

Real-Time Time-Optimal Reorientation of a Rigid Spacecraft

Algorithmic Design and Performance Evaluation

Leonardo Eitner, M.Sc. Candidate

Thesis for the attainment of the academic degree

Master of Science in Aerospace

at the School of Engineering and Design of the Technical University of Munich.

Examiner:

Prof. Dr. Marcello Romano

Supervisor:

M.Sc. Silvia Busi

Submitted:

Munich, 30.11.2025



© Leonardo Eitner, M.Sc. Candidate, 2025

Matriculation Number: 03781345

CoA-2025-MT-AB-1234

I hereby declare that the work presented in this thesis is entirely the result of my own work except where otherwise indicated. To the best of my knowledge the work is original and ideas developed in collaboration with others have been appropriately referenced. Suggestions from the supervisors regarding language and content are excepted.

Abstract

Rapid spacecraft reorientation is critical for emerging applications, including fast low-Earth orbit communication satellites, on-orbit servicing, active debris removal, and defence systems. While time-optimal attitude manoeuvring has been extensively studied, existing solutions typically require significant computation time, limiting their applicability to real-time operations. This paper addresses the challenge of computing time-optimal spacecraft attitude trajectories in real-time (under 0.2 seconds) for generalised initial and final states, including orientation and angular velocities, as well as for spacecraft with asymmetric inertia properties. A comprehensive simulation platform was developed in C++ and CUDA using CasADi to systematically evaluate direct transcription methods for the Optimal Control Problem (OCP). The work examines key algorithmic tradeoffs, including multiple shooting versus direct collocation, implicit versus explicit integration schemes, GPU versus CPU dynamics propagation, and FATROP versus IPOPT solvers. Additionally, the impact of initialisation strategies is investigated, comparing fixed initial guesses with Particle Swarm Optimisation (PSO) approaches. For the latter, both full control trajectory optimisation and Switch Time Optimisation (STO) are compared. Monte Carlo simulations are employed to assess the reliability of each configuration across diverse manoeuvre scenarios, with results corroborated using CGPOPS. The optimal configuration combines FATROP with a fixed deterministic initialisation, multiple shooting transcription, and CPU-based fourth-order Runge-Kutta integration. For rest-to-rest manoeuvres with symmetric spacecraft, this approach yields the optimal solution in over 90% of cases, with computation times under 0.12 seconds. Performance degrades with increasing spacecraft asymmetry and angular velocity magnitudes, though the algorithm maintains practical utility across a wide operational envelope. This work presents a reliable real-time algorithm for time-optimal spacecraft reorientation manoeuvres capable of handling arbitrary initial and final attitude states and asymmetric inertia configurations. The following methodology provides practical guidance for implementation choices in real-time attitude control systems. Future work can extend the framework to incorporate keep-out cone constraints and trajectory path restrictions for collision avoidance and operational safety requirements.

Contents

| | |
|---|-------------|
| Abstract | v |
| List of Symbols | xiii |
| 1 Introduction | 1 |
| 1.1 Motivation | 1 |
| 1.2 Research Question | 2 |
| 1.3 Thesis Structure | 2 |
| 2 Theoretical Foundations | 5 |
| 2.1 Spacecraft Attitude Dynamics | 5 |
| 2.1.1 Euler's Rotational Equations | 5 |
| 2.1.2 Attitude Parameterisation Methods | 6 |
| 2.2 Optimal Control Theory | 9 |
| 2.2.1 Optimal Control Problem Formulation | 9 |
| 2.2.2 Pontryagin's Minimum Principle | 9 |
| 2.2.3 Time-Optimal Control Theory | 10 |
| 2.3 Trajectory Optimisation Methods | 11 |
| 2.3.1 Indirect Methods | 11 |
| 2.3.2 Direct Transcription Methods | 12 |
| 2.4 Optimisation Variables | 17 |
| 2.4.1 Direct Dynamics Formulation | 17 |
| 2.4.2 Inverse Dynamics Formulation | 19 |
| 2.4.3 Selection Criteria and Trade-Offs | 20 |
| 2.5 Time-Optimal Spacecraft Attitude Manoeuvres | 20 |
| 2.5.1 Historical Development | 20 |
| 2.5.2 Problem Formulation | 22 |
| 2.5.3 Optimal Control Characterisation | 23 |
| 2.6 Computational Methods and Implementation | 24 |
| 2.6.1 Nonlinear Programming Solvers | 25 |
| 2.6.2 Optimal Control Software Frameworks | 26 |
| 2.6.3 Derivative-Free Optimisation | 27 |
| 2.7 Efficiency and Reliability | 29 |
| 2.7.1 Initialisation Strategies | 29 |
| 2.7.2 GPU Acceleration Techniques | 30 |
| 2.7.3 Reliability Assessment | 33 |
| 3 Methodology | 35 |
| 3.1 Foundational Design Choices | 35 |
| 3.2 Algorithmic Optimisation | 36 |
| 3.2.1 Transcription Method Selection | 37 |
| 3.2.2 GPU-Accelerated Dynamics Propagation | 37 |
| 3.2.3 NLP Solver Optimisation | 38 |
| 3.3 Algorithm Reliability Assessment | 38 |
| 3.3.1 Test Problem Suite Definition | 38 |

Contents

| | | |
|---------------------|--|-----------|
| 3.3.2 | Monte Carlo Simulation Framework | 39 |
| 3.3.3 | Performance Metrics and Evaluation Criteria | 39 |
| 3.4 | PSO Initialisation Strategy Development and Evaluation | 40 |
| 3.4.1 | Control Parameterisation Approaches | 41 |
| 3.4.2 | Parameter Tuning and Optimisation | 42 |
| 3.4.3 | Performance Evaluation | 43 |
| 3.5 | Implementation Details | 43 |
| 3.5.1 | Computational Platform Specifications | 43 |
| 3.5.2 | Problem-Specific Parameter Values | 45 |
| 3.6 | Chapter Summary | 45 |
| 4 | Results | 51 |
| 4.1 | Gradient-based Strategy Optimisation Results | 51 |
| 4.1.1 | Transcription Method Comparison | 51 |
| 4.1.2 | Integration Scheme Comparison | 56 |
| 4.1.3 | NLP Solver Comparison | 58 |
| 4.2 | Algorithmic Reliability Analysis | 59 |
| 4.2.1 | Success Rate | 59 |
| 4.2.2 | Computation Time | 59 |
| 4.2.3 | Solution Optimality | 60 |
| 4.3 | PSO Development | 61 |
| 4.3.1 | Parameter Tuning Results | 61 |
| 4.3.2 | Trajectory Visualisation | 62 |
| 4.4 | PSO Reliability Analysis | 64 |
| 4.4.1 | Success Rate | 65 |
| 4.4.2 | Computation Time | 65 |
| 4.4.3 | Solution Optimality | 67 |
| 5 | Conclusion | 69 |
| 5.1 | Limitations | 69 |
| 5.1.1 | Modelling Assumptions and Scope | 70 |
| 5.1.2 | Numerical Integration and Asymmetric Spacecraft | 70 |
| 5.1.3 | PSO Parameter Tuning Scope | 70 |
| 5.1.4 | Computational Hardware | 70 |
| 5.2 | Future Work | 70 |
| 5.2.1 | Extended Dynamical Models | 71 |
| 5.2.2 | Runtime Inertia Adaptation | 71 |
| 5.2.3 | Adaptive PSO Parameterisation | 71 |
| 5.2.4 | Path Constraint Integration | 71 |
| 5.2.5 | Hardware-in-the-Loop Validation | 71 |
| 5.3 | Closing Remark | 71 |
| Bibliography | | 73 |

List of Figures

| | | |
|------|--|----|
| 2.1 | CUDA hierarchical thread organisation. | 31 |
| 2.2 | CUDA memory hierarchy from fastest to slowest. | 31 |
| 2.3 | Coalesced memory access vs non-coalesced memory accesses. | 32 |
| 3.1 | Foundational work and baseline algorithm implementation diagram. | 47 |
| 3.2 | Optimised and benchmark algorithm development diagram. | 47 |
| 3.3 | Optimised algorithm reliability analysis diagram. | 48 |
| 3.4 | PSO development diagram. | 49 |
| 3.5 | PSO reliability analysis. | 50 |
| 4.1 | Time-optimal trajectory using multiple shooting transcription for a 90° manoeuvre. | 52 |
| 4.2 | Time-optimal trajectory using Hermite-Simpson collocation transcription for a 90° manoeuvre. | 53 |
| 4.3 | Time-optimal trajectory for a 45° manoeuvre. | 54 |
| 4.4 | Time-optimal trajectory for a 180° manoeuvre. | 55 |
| 4.5 | Success rate of the developed algorithms over the 3 different scenarios. | 60 |
| 4.6 | Computation time of the developed algorithms over the 3 different scenarios. | 60 |
| 4.7 | Optimality gap for non-converged runs of the optimised algorithm. | 61 |
| 4.8 | Output trajectory generated by the PSO with full control trajectory parameterisation. | 63 |
| 4.9 | Output trajectory generated by the PSO with STO parameterisation. | 64 |
| 4.10 | Success rate of the developed algorithm with different initialisation strategies. | 65 |
| 4.11 | Computation time of the optimised algorithm with PSO initialisation. | 66 |
| 4.12 | Discriminated computation time between time spent on PSO and on the gradient-based solver. | 67 |
| 4.13 | Optimality gap for non-converged runs of the optimised algorithm with PSO initialisation. | 68 |

List of Tables

| | | |
|-----|---|----|
| 2.1 | Comparison of attitude parameterisation methods for optimal control applications. | 8 |
| 2.2 | Comparison of pseudospectral collocation methods for trajectory optimisation. | 16 |
| 2.3 | Comparison of NLP solvers for trajectory optimisation. | 26 |
| 3.1 | Dimensionless parameters for spacecraft attitude control optimisation. | 36 |
| 3.2 | Analytical solutions for minimum-time rest-to-rest manoeuvres of symmetric spacecraft. | 37 |
| 3.3 | Monte Carlo simulation parameter ranges for boundary condition sampling. | 40 |
| 3.4 | Performance metric definitions and acceptance criteria for algorithm verification. | 41 |
| 3.5 | PSO parameter ranges for LHS-based tuning. | 43 |
| 3.6 | Computational platform hardware specifications. | 44 |
| 3.7 | Software environment version specifications. | 44 |
| 3.8 | NLP solver configuration parameters. | 45 |
| 3.9 | CGPOPS configuration parameters. | 46 |
| 4.1 | Performance comparison of transcription methods for a 90° manoeuvre. | 52 |
| 4.2 | Performance comparison of transcription methods for a 45° manoeuvre. | 55 |
| 4.3 | Performance comparison of transcription methods for a 180° manoeuvre. | 56 |
| 4.4 | Performance comparison of integration methods for different manoeuvre angles. | 56 |
| 4.5 | Computational performance breakdown of the GPU-accelerated optimisation framework using RK4 for a 180° rotation. | 57 |
| 4.6 | Performance comparison of different RK4 integration implementations. | 57 |
| 4.7 | Computational performance breakdown of the GPU-accelerated optimisation framework using RK4 with structure-exploiting gradient computation for a 180° rotation. | 58 |
| 4.8 | Performance comparison of IPOPT and FATROP NLP solvers for different manoeuvre angles. | 59 |
| 4.9 | PSO optimal parameters. | 62 |

List of Symbols

General Symbols

| | | |
|----------------------|----------------------|--|
| b | [·] | Basis function coefficient vector |
| e | [·] | Unit rotation axis vector |
| f | [·] | System dynamics function |
| f₀ | [·] | Drift dynamics (control-free dynamics) |
| G | [·] | Control influence matrix |
| g | [·] | Global best position (PSO) |
| I₃ | [·] | 3×3 identity matrix |
| J | [kg·m ²] | Inertia tensor (matrix) |
| q | [·] | Unit quaternion vector |
| q_I | [·] | Identity quaternion [1 0 0 0] ^T |
| R | [·] | Rotation matrix |
| S | [·] | Switching function vector |
| t_i | [s] | Switching times vector for axis <i>i</i> |
| u | [·] | Control vector |
| v | [·] | Velocity vector (PSO) |
| x | [·] | State vector |
| z | [·] | Position vector (PSO) |
| B | [·] | Body-fixed reference frame |
| C | [·] | Chebyshev polynomial |
| I | [·] | Inertial reference frame |
| J | [·] | Cost functional |
| K | [·] | PSO iterations |
| L | [·] | Lagrange interpolating polynomial |
| N | [·] | PSO population size |
| P | [·] | Legendre polynomial |

List of Symbols

| | | |
|-----------------|---------------------------------------|---|
| σ | [\cdot] | Sigmoid function |
| τ | [\cdot] | Computation time |
| \mathcal{U} | [\cdot] | Admissible control set |
| c | [\cdot] | Collocation point |
| C_{sw} | [\cdot] | Switch count function |
| D | [\cdot] | Parameter space dimension |
| H | [\cdot] | Hamiltonian function |
| h | [kg·m ² ·s ⁻¹] | Angular momentum |
| H_0 | [\cdot] | Control-independent Hamiltonian portion |
| J | [kg·m ²] | Principal moment of inertia |
| L | [\cdot] | Running cost (Lagrange term) |
| l | [\cdot] | Number of samples |
| M | [\cdot] | Number of basis functions |
| m | [\cdot] | Control vector dimension |
| N | [\cdot] | Number of discretisation points/intervals |
| n | [\cdot] | State vector dimension |
| p | [\cdot] | Polynomial degree |
| q | [\cdot] | Quaternion component |
| r | [\cdot] | Random number |
| S | [\cdot] | Switching function component |
| s | [\cdot] | Initial control direction (bang-bang) |
| t | [s] | Time |
| u | [\cdot] | Control vector component |
| v | [\cdot] | Velocity vector component (PSO) |
| V_{\max} | [\cdot] | Maximum velocity (PSO) |
| w_0 | [\cdot] | Inertia weight (PSO) |
| w_1 | [\cdot] | Cognitive parameter (PSO) |
| w_2 | [\cdot] | Social parameter (PSO) |
| x | [\cdot] | State vector component |
| y | [\cdot] | Number of switches per control axis |
| z | [\cdot] | Position vector component (PSO) |

Greek Symbols

| | | |
|---------------|--------------------------|---|
| α | [\cdot] | Scaling parameter |
| β | [rad] | Rotation angle |
| γ | [\cdot] | Integrated state prediction |
| κ | [\cdot] | Runge-Kutta slope |
| λ | [\cdot] | Costate vector (adjoint variable) |
| ν | [\cdot] | Lagrange multipliers for terminal constraints |
| ω | [N·m] | Angular velocity vector |
| Ω | [rad · s ⁻¹] | Skew-symmetric angular velocity matrix |
| Ψ | [\cdot] | Terminal constraint function |
| ρ | [\cdot] | Personal best position (PSO) |
| σ | [\cdot] | Modified Rodrigues Parameters vector |
| τ | [N·m] | Torque vector |
| ε | [\cdot] | Hermite-Simpson collocation constraint |
| χ | [\cdot] | Basis function |
| Δ | [\cdot] | Change |
| δ | [\cdot] | Kronecker delta |
| ϵ | [\cdot] | Saturation threshold |
| η | [\cdot] | Number of terminal constraints |
| μ | [\cdot] | Eigenvalue (complex) |
| ω | [rad · s ⁻¹] | Angular velocity vector component |
| Φ | [\cdot] | Terminal cost (Mayer term) |
| ϕ | [rad] | Roll Euler angle |
| ψ | [rad] | Yaw Euler angle |
| Σ | [\cdot] | Sum |
| τ | [N·m] | Torque vector component |
| θ | [rad] | Pitch Euler angle |

Subscripts

| | |
|------------------|---------------|
| \square_0 | Initial value |
| \square_{\max} | Maximum value |

List of Symbols

| | |
|-----------------------------|--|
| \llcorner_{\min} | Minimum value |
| \llcorner_ω | Angular velocity component |
| \llcorner_{init} | Relative to initialisation |
| \llcorner_{opt} | Relative to an optimal value |
| \llcorner_{rot} | Relative rotation |
| $\llcorner_{\text{solver}}$ | Relative to the gradient-based solver |
| \llcorner_{sw} | Control switch-related |
| \llcorner_{total} | Relative to a total value |
| \llcorner_x | Skew-symmetric cross-product matrix operator |
| \llcorner_d | Dimension index |
| \llcorner_f | Final value |
| \llcorner_i | Component along axis i |
| \llcorner_j | Particle/point index |
| \llcorner_k | Time step/interval index |
| \llcorner_q | Quaternion component |

Superscripts

| | |
|---------------------|---|
| $\bar{\square}$ | Normalisation by a characteristic scale |
| \llcorner^* | Optimal value |
| \llcorner^{-1} | Inverse |
| \llcorner^- | Quaternion conjugate |
| \llcorner^\dagger | Pseudoinverse |
| \llcorner^k | Iteration index |
| \llcorner^T | Transposed |
| $\ddot{\llcorner}$ | Second time derivative |
| $\dot{\llcorner}$ | First time derivative |

Special Symbols

| | |
|---------------|-------------------------------------|
| $\cos(\cdot)$ | Cosine function |
| $\det(\cdot)$ | Matrix determinant |
| \in | Is within a specified set of values |

| | |
|----------------------|--|
| ∞ | Infinity |
| \mathbb{C} | Set of complex numbers |
| \mathbb{R} | Set of real numbers |
| \mathbf{X} | Multi-dimensional variables |
| \otimes | Quaternion multiplication |
| $\sin(\cdot)$ | Sine function |
| \subset | Is a subset of a specified set of values |
| $\tan(\cdot)$ | Tangent function |
| $\text{diag}(\cdot)$ | Diagonal matrix |
| $\max(\cdot)$ | Returns the maximum value |
| $\min(\cdot)$ | Returns the minimum value |
| $\text{sgn}(\cdot)$ | Sign function |
| \times | Vector cross product |

Abbreviations

| | |
|------|-----------------------------------|
| AD | Automatic Differentiation |
| ADR | Active Debris Removal |
| API | Application Programming Interface |
| BC | Boundary Conditions |
| CGL | Chebyshev-Gauss-Lobatto |
| CPU | Central Processing Unit |
| DRAM | Dynamic Random Access Memory |
| FD | Finite Differences |
| GPU | Graphics Processing Unit |
| IP | Interior Point |
| KKT | Karush-Kuhn-Tucker |
| LEO | Low Earth Orbit |
| LG | Legendre-Gauss |
| LGR | Legendre-Gauss-Radau |
| LHS | Latin Hypercube Sampling |
| MC | Monte Carlo |

List of Symbols

| | |
|-------|---|
| MPC | Model Predictive Control |
| MRP | Modified Rodrigues Parameters |
| NLP | Non-Linear Programming |
| OCP | Optimal Control Problem |
| ODE | Ordinary Differentiable Equation |
| OOS | On-Orbit Servicing |
| PCIe | Peripheral Component Interconnect Express |
| PMP | Pontryagin Maximum Principle |
| PSO | Particle Swarm Optimisation |
| QP | Quadratic Programming |
| RK4 | Runge-Kutta of fourth-order |
| SCP | Sequential Convex Programming |
| SIMT | Single Instruction, Multiple Thread |
| SM | Streaming Multiprocessors |
| SO(3) | Special Orthogonal group in three-dimensional Euclidean space |
| SQP | Sequential Quadratic Programming |
| STO | Switch Time Optimisation |
| TDP | Thermal Design Power |
| TPBVP | Two-Point Boundary Value Problem |

1 Introduction

The precise determination and manipulation of spacecraft orientation, known as spacecraft attitude control, constitutes a fundamental enabling technology for space missions ranging from Earth observation and telecommunications to scientific exploration and defence applications. As satellite systems evolve toward increasingly agile operations, particularly in Low Earth Orbit (LEO) constellations, the demand for rapid and precise reorientation capabilities has intensified. Time-optimal attitude control, which seeks to minimise manoeuvre duration while respecting physical constraints on actuator torques, represents the theoretical performance limit for spacecraft agility. However, classical approaches for calculating the time-optimal trajectory, whether indirect methods based on Pontryagin's Maximum Principle (PMP) or direct methods employing pseudospectral transcription, typically require computation times incompatible with real-time onboard implementation. This thesis addresses the challenge of generating time-optimal spacecraft attitude trajectories with computation times suitable for closed-loop control, enabling autonomous spacecraft to respond dynamically to mission requirements and environmental disturbances. Through systematic investigation of algorithm optimisation methods and intelligent initialisation strategies, this work develops and verifies a real-time algorithm capable of computing time-optimal rest-to-rest and track-to-track manoeuvres for spacecraft with arbitrary inertia properties.

1.1 Motivation

Spacecraft attitude control systems are undergoing a paradigm shift driven by applications that demand unprecedented agility and responsiveness. The proliferation of LEO satellite constellations for global communications and the development of space-based defence systems have created a critical need for rapid spacecraft reorientation capabilities. Unlike geostationary satellites that maintain relatively fixed orientations, LEO satellites require frequent attitude manoeuvres to execute transitions between observation targets, whether for maintaining communication links, tracking ground targets, or executing collision avoidance manoeuvres.

Additionally, the emerging fields of On-Orbit Servicing (OOS) and Active Debris Removal (ADR) missions impose stringent requirements for agile attitude control systems, as the non-cooperative nature of client satellites and debris targets presents significant challenges. Debris objects or satellites in safe mode will be tumbling rather than maintaining stable attitudes [1], necessitating advanced control strategies capable of approaching, capturing, and stabilising rotating targets. Underactuated spacecraft control, either by design or due to onboard failures, also represents a significant driver for attitude control innovation. Being able to compensate for the missing actuation by quickly reorienting the spacecraft can extend operational life and improve mission robustness [2], providing fault tolerance and enabling novel control architectures that reduce system complexity and mass.

The time-optimal control of spacecraft attitude has been extensively studied since the foundational work by Bilimoria and Wie [3], who demonstrated that time-optimal reorientation of asymmetric rigid bodies does not follow the intuitive eigenaxis manoeuvre. Subsequent research by Bai and Junkins [4] and others has refined these results, establishing theoretical frameworks for computing time-optimal trajectories. However, a persistent limitation of these approaches is their computational complexity: traditional methods based on indirect optimal control or pseudospectral transcription can require computation times ranging from several seconds to minutes [5], rendering them unsuitable for real-time onboard implementation.

This computational bottleneck creates a fundamental trade-off in the design of spacecraft control systems. Controllers must either sacrifice optimality by using suboptimal but computationally efficient methods (e.g., eigenaxis manoeuvres or proportional-derivative control) or compute optimal trajectories offline with limited adaptability to changing mission requirements or disturbances. For applications requiring rapid retargeting—such as surveillance satellites tracking multiple ground targets, communication satellites maintaining a line of sight with mobile ground stations, or defensive systems responding to threats—neither approach is satisfactory.

1.2 Research Question

With the motivation established, the research question that this thesis seeks to answer can be stated clearly:

How can one reliably compute time-optimal spacecraft slew manoeuvres in real-time?

Before answering this question, it is necessary to precisely define three key terms:

1. **Real-time** refers to computation times that enable autonomous trajectory replanning within the operational timescales of spacecraft attitude determination and control systems. The specific threshold depends on the spacecraft’s sensor architecture, control loop frequency, inertia properties, and available control authority. This work establishes a threshold of 200 ms based on spacecraft sensor update cycles. Star trackers—which provide absolute attitude measurements—typically operate at update rates below 5 Hz [6]. A 200 ms computation threshold ensures that trajectory generation can be executed in a closed-loop at the sampling rate of a star tracker, enabling the use of updated time-optimal trajectories with the most recent absolute attitude measurement as the initial condition. This threshold represents approximately a one-order-of-magnitude improvement over state-of-the-art methods [5].
2. **Reliability** quantifies the probability that the optimisation algorithm converges to a feasible and locally optimal solution from arbitrary initial conditions within the operational envelope. High reliability is essential for autonomous onboard implementation, as convergence failures necessitate fallback to suboptimal control strategies, negating the benefits of time-optimal control. Reliability must be characterised statistically through simulations across diverse scenarios, encompassing spacecraft with varying inertia asymmetry and manoeuvres involving different angular velocity magnitudes.
3. **Optimality** represents the degree to which computed solutions approximate the global time-optimal trajectory. Solution quality is verified by comparison with CGPOPS, an adaptive pseudospectral collocation framework with established accuracy for time-optimal control problems [7]. This verification ensures that computational efficiency gains do not compromise the optimality of the solution.

Achieving a satisfactory answer to this research question requires a thorough investigation of the algorithmic design space to identify the configuration that optimally balances computational efficiency, solution reliability, and solution quality. This investigation encompasses multiple algorithmic components—transcription methods, integration schemes, Non-Linear Programming (NLP) solvers, initialisation strategies, and computational architectures—each presenting distinct trade-offs that must be rigorously evaluated.

1.3 Thesis Structure

This thesis is organised into five chapters, each addressing a distinct aspect of the real-time time-optimal spacecraft attitude control problem.

Chapter 1: Introduction establishes the motivation for real-time time-optimal attitude control in autonomous spacecraft operations, defines the research objectives, articulates the key performance metrics, and outlines the contributions of this work.

Chapter 2: Theoretical Foundations reviews spacecraft attitude dynamics and optimal control theory, including attitude parameterisation methods, Euler's rotational equations, and the PMP. The chapter surveys the state-of-the-art in trajectory optimisation methods, covering indirect and direct approaches, problem formulation strategies, computational methods, initialisation strategies, and Graphics Processing Unit (GPU) acceleration techniques for parallel computation.

Chapter 3: Methodology describes the research workflow and algorithmic framework developed in this thesis. The chapter presents the specific Optimal Control Problem (OCP) formulation employed and provides a full guide on the decisions and choices made throughout the work. It describes the software architecture and implementation details of the comprehensive simulation platform developed in C++ and CUDA. The chapter covers the integration of CasADi for automatic differentiation and NLP problem formulation, the implementation of CGPOPS for verification and benchmarking, and the GPU acceleration strategies. Computational platform specifications and software design patterns employed to ensure modularity and extensibility are documented.

Chapter 4: Results presents the outcomes of the systematic algorithmic optimisation, as well as the results of the Monte Carlo (MC) simulations employed to evaluate the performance and reliability of different algorithmic configurations. The sensitivity of algorithm performance to spacecraft asymmetry and angular velocity magnitudes is analysed. The chapter identifies the optimal configuration and characterises its operational envelope.

Chapter 5: Conclusion summarises the principal findings of the research, emphasising the key algorithmic choices that enable real-time time-optimal spacecraft attitude slew manoeuvres. Limitations of the current approach are discussed, and future research directions are outlined. It concludes with reflections on the broader implications of this work for autonomous spacecraft systems and the potential for onboard implementation.

2 Theoretical Foundations

Time-optimal spacecraft reorientation requires the integration of rigid body dynamics, optimal control theory, and computational optimisation methods. The complexity of this problem arises from several sources: nonlinear gyroscopic coupling in Euler's rotational equations, the bang-bang control structure that introduces discontinuities challenging for numerical solution, nonconvex optimisation landscapes with multiple local minima, and real-time computational constraints that restrict algorithmic complexity. Developing efficient algorithms necessitates a good understanding of the theoretical foundations and computational methods underlying trajectory optimisation.

This chapter establishes the mathematical framework required for computing real-time time-optimal spacecraft attitude manoeuvres. Section 2.1 presents spacecraft attitude dynamics and parameterisation methods. Section 2.2 develops optimal control theory and specialises to time-optimal problems. Section 2.3 examines indirect and direct trajectory optimisation methodologies. Section 2.4 analyses problem formulation strategies, including control parameterisation and dynamics representation. Section 2.5 applies optimal control theory to spacecraft attitude manoeuvres, deriving the bang-bang control structure and reviewing historical developments. Section 2.6 surveys computational infrastructure, including nonlinear programming solvers, software frameworks, and derivative-free optimisation methods. Section 2.7 addresses initialisation strategies, GPU acceleration, and statistical reliability assessment methods.

2.1 Spacecraft Attitude Dynamics

The mathematical description of spacecraft rotational motion constitutes the foundation upon which attitude control algorithms are constructed. This description comprises two essential components: the dynamic equations governing the evolution of angular velocity under applied torques, and the kinematic equations relating angular velocity to the rate of change of attitude with respect to time. The former is governed by Euler's rotational equations, which express the balance of angular momentum for a rigid body in rotational motion. The latter depends critically on the choice of attitude parameterisation, i.e., the mathematical representation used to describe the spacecraft's orientation in three-dimensional space.

The selection of an appropriate attitude parameterisation has a significant influence on both the theoretical properties and computational efficiency of optimal control algorithms. Various parameterisation schemes have been developed, each exhibiting distinct advantages and limitations [8]. This section presents the fundamental equations governing spacecraft attitude dynamics and examines the principal parameterisation methods employed in trajectory optimisation. Section 2.1.1 derives Euler's rotational equations and establishes the relationship between control torques and angular acceleration. Section 2.1.2 surveys attitude parameterisation methods, analysing their properties in the context of time-optimal control problem formulation.

2.1.1 Euler's Rotational Equations

The rotational motion of a rigid spacecraft is governed by the principle of conservation of angular momentum. For a rigid body with angular momentum vector \mathbf{h} , the time rate of change of angular momentum equals the applied external torque $\boldsymbol{\tau}$:

$$\frac{d\mathbf{h}}{dt} \Big|_{\mathcal{I}} = \boldsymbol{\tau} \quad (2.1)$$

where the derivative is taken with respect to an inertial reference frame \mathcal{I} . For spacecraft attitude control applications, it is advantageous to express the equations of motion in a body-fixed reference frame \mathcal{B} aligned with the spacecraft's principal axes of inertia. According to the vector transport theorem, the transformation of the time derivative from the inertial frame to the body-fixed frame introduces an additional term:

$$\frac{d\mathbf{h}}{dt} \Big|_{\mathcal{I}} = \frac{d\mathbf{h}}{dt} \Big|_{\mathcal{B}} + \boldsymbol{\omega} \times \mathbf{h} \quad (2.2)$$

where $\boldsymbol{\omega} = [\omega_1, \omega_2, \omega_3]^T$ represents the angular velocity vector of the body-fixed frame relative to the inertial frame, expressed in body-fixed coordinates. The angular momentum in the body frame is related to the angular velocity through the inertia tensor \mathbf{J} :

$$\mathbf{h} = \mathbf{J}\boldsymbol{\omega} \quad (2.3)$$

Substituting equations (2.2) and (2.3) into equation (2.1) yields:

$$\mathbf{J}\dot{\boldsymbol{\omega}} + \boldsymbol{\omega} \times \mathbf{J}\boldsymbol{\omega} = \boldsymbol{\tau} \quad (2.4)$$

where $\dot{\boldsymbol{\omega}}$ denotes the time derivative of angular velocity in the body frame. Equation (2.4) represents Euler's rotational equations in vector form.

For a spacecraft with principal axes aligned with the body frame, the inertia tensor is diagonal: $\mathbf{J} = \text{diag}(J_1, J_2, J_3)$, where J_1 , J_2 , and J_3 are the principal moments of inertia. The component form of Euler's equations is then:

$$\begin{aligned} J_1\dot{\omega}_1 + (J_3 - J_2)\omega_2\omega_3 &= \tau_1 \\ J_2\dot{\omega}_2 + (J_1 - J_3)\omega_3\omega_1 &= \tau_2 \\ J_3\dot{\omega}_3 + (J_2 - J_1)\omega_1\omega_2 &= \tau_3 \end{aligned} \quad (2.5)$$

where τ_1 , τ_2 , and τ_3 are the control torques applied about the principal axes. The terms involving products of angular velocity components: $(J_3 - J_2)\omega_2\omega_3$, $(J_1 - J_3)\omega_3\omega_1$, and $(J_2 - J_1)\omega_1\omega_2$, are known as gyroscopic coupling terms. These terms introduce nonlinearity into the dynamics and couple the three rotational degrees of freedom.

The magnitude of gyroscopic coupling depends on the spacecraft's inertial asymmetry. For a spherically symmetric spacecraft with $J_1 = J_2 = J_3$, the gyroscopic terms vanish entirely, and the rotational dynamics decouple into three independent scalar equations. However, most practical spacecraft exhibit asymmetric inertia distributions, resulting in significant gyroscopic coupling that fundamentally affects optimal control solutions [9].

For optimal control applications, Euler's equations are typically written in state-space form. Solving equations (2.5) for the angular accelerations yields:

$$\begin{aligned} \dot{\omega}_1 &= \frac{1}{J_1} [\tau_1 - (J_3 - J_2)\omega_2\omega_3] \\ \dot{\omega}_2 &= \frac{1}{J_2} [\tau_2 - (J_1 - J_3)\omega_3\omega_1] \\ \dot{\omega}_3 &= \frac{1}{J_3} [\tau_3 - (J_2 - J_1)\omega_1\omega_2] \end{aligned} \quad (2.6)$$

These equations establish the relationship between control torques and the resulting angular acceleration. Combined with kinematic equations that relate angular velocity to attitude, equations (2.6) form the complete dynamical system for spacecraft attitude control.

2.1.2 Attitude Parameterisation Methods

The orientation of a rigid body in three-dimensional space possesses three rotational degrees of freedom, yet various mathematical representations exist to describe this orientation. The kinematic

equations relating angular velocity to attitude depend fundamentally on the chosen parameterisation of the attitude. This subsection examines the principal attitude parameterisation schemes employed in optimal control applications, analysing their mathematical properties and computational implications.

Euler Angles

Euler angles parameterise attitude through three successive rotations about specified axes. The most commonly adopted representation follows the 3-2-1 (yaw-pitch-roll) sequence with angles ψ (yaw), θ (pitch), and ϕ (roll). The kinematic equations relating angular velocity $\boldsymbol{\omega} = [\omega_1, \omega_2, \omega_3]^T$ to Euler angle rates are:

$$\begin{bmatrix} \dot{\phi} \\ \dot{\theta} \\ \dot{\psi} \end{bmatrix} = \begin{bmatrix} 1 & \sin \phi \tan \theta & \cos \phi \tan \theta \\ 0 & \cos \phi & -\sin \phi \\ 0 & \sin \phi / \cos \theta & \cos \phi / \cos \theta \end{bmatrix} \begin{bmatrix} \omega_1 \\ \omega_2 \\ \omega_3 \end{bmatrix} \quad (2.7)$$

While intuitive and requiring only three parameters (matching the physical degrees of freedom), this representation suffers from singularities at certain orientations where the mapping between angular velocity and the time derivative of Euler angles becomes undefined [8]. The kinematic equations (2.7) contain trigonometric functions in the denominator that approach zero when the pitch angle approaches $\pm 90^\circ$, a configuration known as gimbal lock. At these singular orientations, the transformation matrix becomes rank-deficient, and infinitely many combinations of $\dot{\phi}$ and $\dot{\psi}$ can produce the same angular velocity. These singularities restrict the applicability of Euler angles to problems where the spacecraft orientation remains within a limited range, making them unsuitable for large-angle reorientation manoeuvres [8].

Unit Quaternions

Unit quaternions provide a globally non-singular four-parameter representation of attitude. A unit quaternion $\mathbf{q} = [q_0, q_1, q_2, q_3]^T$ (where q_0 is the scalar part and $[q_1, q_2, q_3]^T$ the vector part) satisfies the unit norm constraint $\|\mathbf{q}\| = \sqrt{q_0^2 + q_1^2 + q_2^2 + q_3^2} = 1$. The kinematic equation relating angular velocity to the time derivative of the quaternion is:

$$\dot{\mathbf{q}} = \frac{1}{2} \boldsymbol{\Omega}(\boldsymbol{\omega}) \mathbf{q} \quad (2.8)$$

where $\boldsymbol{\Omega}(\boldsymbol{\omega})$ is the skew-symmetric matrix:

$$\boldsymbol{\Omega}(\boldsymbol{\omega}) = \begin{bmatrix} 0 & -\omega_1 & -\omega_2 & -\omega_3 \\ \omega_1 & 0 & \omega_3 & -\omega_2 \\ \omega_2 & -\omega_3 & 0 & \omega_1 \\ \omega_3 & \omega_2 & -\omega_1 & 0 \end{bmatrix} \quad (2.9)$$

The quaternion kinematic equation (2.8) is linear in both \mathbf{q} and $\boldsymbol{\omega}$ and remains well-defined for all orientations. However, the unit norm constraint introduces an algebraic constraint into the optimisation problem. This constraint can be handled through explicit normalisation at each time step, penalty methods, or direct enforcement within the NLP formulation [10]. The unit quaternion representation constitutes a double cover of the attitude space $\text{SO}(3)$, meaning that antipodal quaternions \mathbf{q} and $-\mathbf{q}$ represent the same physical orientation. Despite the redundant parameterisation, quaternions have become the dominant choice for spacecraft attitude control due to their singularity-free representation and computational efficiency [8].

Modified Rodrigues Parameters

MRPs constitute a three-parameter minimal representation that avoids the redundancy of quaternions. For a rotation through angle β about axis \mathbf{e} , the MRP vector is defined as:

$$\boldsymbol{\sigma} = \mathbf{e} \tan\left(\frac{\beta}{4}\right) \quad (2.10)$$

The kinematic equation for MRPs is:

$$\dot{\boldsymbol{\sigma}} = \frac{1}{4} [(1 - \|\boldsymbol{\sigma}\|^2)\mathbf{I}_3 + 2[\boldsymbol{\sigma}]_{\times} + 2\boldsymbol{\sigma}\boldsymbol{\sigma}^T] \boldsymbol{\omega} \quad (2.11)$$

where $[\boldsymbol{\sigma}]_{\times}$ denotes the skew-symmetric cross-product matrix, and \mathbf{I}_3 the 3-by-3 identity matrix. MRPs offer computational advantages for small to moderate rotations, as the kinematic equation (2.11) involves only algebraic operations without transcendental functions. However, MRPs exhibit a singularity at $\beta = \pm 360^\circ$ (corresponding to $\|\boldsymbol{\sigma}\| \rightarrow \infty$), limiting their applicability to large-angle manoeuvres [8]. Shadow sets of MRPs can be employed to extend the valid range by switching to an alternative representation when $\|\boldsymbol{\sigma}\|$ exceeds a threshold, but this introduces discontinuities that complicate gradient-based optimisation.

Rotation Matrices and SO(3)

Rotation matrices provide a coordinate-free representation of attitude on the Special Orthogonal group SO(3). A rotation matrix $\mathbf{R} \in \mathbb{R}^{3 \times 3}$ satisfies the orthonormality constraints $\mathbf{R}^T \mathbf{R} = \mathbf{I}_3$ and $\det(\mathbf{R}) = 1$. The kinematic equation on SO(3) is:

$$\dot{\mathbf{R}} = \mathbf{R}[\boldsymbol{\omega}]_{\times} \quad (2.12)$$

Direct SO(3) parameterisation avoids singularities entirely and provides a natural framework for geometric control design [11, 12]. The manifold structure of SO(3) can be preserved through Lie group integrators that maintain orthonormality without explicit constraint enforcement. However, even then, when compared to the three physical rotational degrees of freedom, the nine matrix elements still introduce six redundant terms. If orthonormality constraints are explicitly enforced within the optimisation problem, its computational complexity increases beyond the other attitude parameterisation strategies. Recent developments in geometric optimisation and structure-preserving discretisation have made SO(3) representations increasingly competitive for trajectory optimisation, particularly when combined with variational integrators [12].

Selection Criteria for Optimal Control

The choice of attitude parameterisation for time-optimal control involves trade-offs between singularity avoidance, computational efficiency, and constraint complexity. Table 2.1 summarises the key characteristics of each parameterisation method.

Table 2.1 Comparison of attitude parameterisation methods for optimal control applications.

| Method | Parameters | Singularities | Constraints |
|--------------|------------|---------------|--------------------|
| Euler Angles | 3 | Yes | None |
| Quaternions | 4 | No | Unit norm |
| MRP | 3 | Yes | None |
| SO(3) | 9 | No | Orthonormality (6) |

For time-optimal spacecraft reorientation problems involving arbitrarily large-angle manoeuvres, quaternion parameterisation offers the most favourable balance of performance. The global validity

without singularities enables reliable optimisation across the entire attitude space, while the unit norm constraint can be efficiently managed through normalisation or penalty methods. The linear kinematic equation (2.8) facilitates efficient gradient computation required by gradient-based NLP solvers. Consequently, quaternion-based formulations have become standard in modern time-optimal attitude control implementations [3, 10, 13].

2.2 Optimal Control Theory

Optimal control theory provides the mathematical framework for determining control inputs that minimise a specified performance criterion while satisfying system dynamics and constraints. For time-optimal spacecraft attitude control, the objective is to reduce the manoeuvre duration subject to actuator torque limitations and prescribed boundary conditions on attitude and angular velocity. The theoretical foundations trace to the calculus of variations, with Pontryagin's seminal contribution extending these principles to control-constrained problems through the introduction of costate variables (also termed adjoint variables or Lagrange multipliers) and the formulation of necessary conditions for optimality [14]. A fundamental result of PMP for time-optimal problems with bounded control is the bang-bang control structure, wherein optimal control inputs assume their extreme values and switch between these extremes a finite number of times [14]. For spacecraft attitude control with torque-limited actuators, this bang-bang structure has been extensively characterised [3, 10], and its exploitation forms the basis for efficient solution algorithms. This section presents the fundamental theory of optimal control, specialises it to the time-optimal control, and establishes the theoretical properties that inform computational solution methods.

2.2.1 Optimal Control Problem Formulation

The general OCP in Bolza form aims to determine a control trajectory $\mathbf{u}(t)$ that minimises a cost functional while satisfying the system dynamics and constraints. Ordinary differential equations describe the system dynamics:

$$\dot{\mathbf{x}}(t) = \mathbf{f}(\mathbf{x}(t), \mathbf{u}(t), t) \quad (2.13)$$

where $\mathbf{x}(t) \in \mathbb{R}^n$ represents the n -dimensional state vector and $\mathbf{u}(t) \in \mathcal{U} \subset \mathbb{R}^m$ denotes the m -dimensional control vector. The admissible control set \mathcal{U} encodes constraints on control values. The time interval of interest is $t \in [t_0, t_f]$, with initial state specified as $\mathbf{x}(t_0) = \mathbf{x}_0$.

Terminal state conditions may assume three forms: $\mathbf{x}(t_f) = \mathbf{x}_f$ for fixed terminal states, For constrained terminal states, the condition $\Psi(\mathbf{x}(t_f), t_f) = \mathbf{0}$ must be satisfied, where $\Psi : \mathbb{R}^n \times \mathbb{R} \rightarrow \mathbb{R}^\eta$ defines η terminal constraints. For free terminal states, $\mathbf{x}(t_f)$ remains unconstrained.

The cost functional in Bolza form combines terminal and running costs:

$$\mathcal{J} = \Phi(\mathbf{x}(t_f), t_f) + \int_{t_0}^{t_f} L(\mathbf{x}(t), \mathbf{u}(t), t) dt \quad (2.14)$$

where $\Phi : \mathbb{R}^n \times \mathbb{R} \rightarrow \mathbb{R}$ represents the terminal cost, also called Mayer term, and $L : \mathbb{R}^n \times \mathbb{R}^m \times \mathbb{R} \rightarrow \mathbb{R}$ denotes the running cost or Lagrange term.

The optimal control $\mathbf{u}^*(t)$ minimises the cost functional \mathcal{J} subject to the dynamics (2.13), control constraints $\mathbf{u}(t) \in \mathcal{U}$, and boundary conditions. The corresponding optimal trajectory $\mathbf{x}^*(t)$ satisfies all constraints and achieves the minimum cost among all admissible solutions [15].

2.2.2 Pontryagin's Minimum Principle

With the OCP formulated, it is now necessary to determine the optimal control $\mathbf{u}^*(t)$ that minimises the cost functional \mathcal{J} . Classical calculus of variations extends naturally to problems with unconstrained controls through the Euler-Lagrange equations, but fails when control authority is bounded. The PMP, established in 1962, extends the calculus of variations to control-constrained

optimisation problems and provides necessary conditions for optimality [14]. The principle introduces the costate vector $\boldsymbol{\lambda}(t) \in \mathbb{R}^n$, which represents the sensitivity of the optimal cost-to-go with respect to state perturbations [15]. The Hamiltonian function is defined as:

$$H(\mathbf{x}, \mathbf{u}, \boldsymbol{\lambda}, t) = L(\mathbf{x}, \mathbf{u}, t) + \boldsymbol{\lambda}^T \mathbf{f}(\mathbf{x}, \mathbf{u}, t) \quad (2.15)$$

The Hamiltonian quantifies the instantaneous trade-off between minimising the running cost and progressing along the state trajectory toward the terminal target.

For an optimal solution $(\mathbf{x}^*(t), \mathbf{u}^*(t), \boldsymbol{\lambda}^*(t))$, PMP requires satisfaction of the following necessary conditions:

(i) State equations:

$$\dot{\mathbf{x}}^*(t) = \frac{\partial H}{\partial \boldsymbol{\lambda}} = \mathbf{f}(\mathbf{x}^*(t), \mathbf{u}^*(t), t) \quad (2.16)$$

(ii) Costate equations:

$$\dot{\boldsymbol{\lambda}}^*(t) = -\frac{\partial H}{\partial \mathbf{x}} = -\frac{\partial L}{\partial \mathbf{x}} - \left(\frac{\partial \mathbf{f}}{\partial \mathbf{x}} \right)^T \boldsymbol{\lambda}^*(t) \quad (2.17)$$

(iii) Optimality condition (minimum principle):

$$H(\mathbf{x}^*(t), \mathbf{u}^*(t), \boldsymbol{\lambda}^*(t), t) = \min_{\mathbf{u} \in \mathcal{U}} H(\mathbf{x}^*(t), \mathbf{u}, \boldsymbol{\lambda}^*(t), t) \quad (2.18)$$

(iv) Transversality conditions: For terminal constraints $\boldsymbol{\Psi}(\mathbf{x}(t_f), t_f) = \mathbf{0}$ with associated Lagrange multipliers $\boldsymbol{\nu} \in \mathbb{R}^q$, the terminal costate satisfies:

$$\boldsymbol{\lambda}^*(t_f) = \frac{\partial \Phi}{\partial \mathbf{x}} \Big|_{t_f} + \boldsymbol{\nu}^T \frac{\partial \boldsymbol{\Psi}}{\partial \mathbf{x}} \Big|_{t_f} \quad (2.19)$$

Additionally, for free terminal time, the Hamiltonian must satisfy the condition:

$$H(\mathbf{x}^*(t_f), \mathbf{u}^*(t_f), \boldsymbol{\lambda}^*(t_f), t_f) = -\frac{\partial \Phi}{\partial t} \Big|_{t_f} - \boldsymbol{\nu}^T \frac{\partial \boldsymbol{\Psi}}{\partial t} \Big|_{t_f} \quad (2.20)$$

These conditions define a two-point boundary value problem (TPBVP): the state equations integrate forward from initial conditions $\mathbf{x}(t_0) = \mathbf{x}_0$, while the costate equations integrate backwards from terminal conditions determined by the transversality conditions. The optimal control at each instant is determined pointwise from the minimisation condition (2.18). The computational challenge of solving the resulting TPBVP motivates the development of direct transcription methods, as discussed in section 2.3.

2.2.3 Time-Optimal Control Theory

For time-optimal control problems where the objective is to minimise manoeuvre duration, the cost functional specialises to $\mathcal{J} = t_f - t_0$ with terminal cost $\Phi = 0$ and running cost $L = 1$. The Hamiltonian (2.15) simplifies to:

$$H = 1 + \boldsymbol{\lambda}^T \mathbf{f}(\mathbf{x}, \mathbf{u}, t) \quad (2.21)$$

Correspondingly, the costate (2.17) reduces to:

$$\dot{\boldsymbol{\lambda}}^*(t) = -\left(\frac{\partial \mathbf{f}}{\partial \mathbf{x}} \right)^T \boldsymbol{\lambda}^*(t) \quad (2.22)$$

For autonomous systems where the dynamics \mathbf{f} do not depend explicitly on time, and with constant running cost $L = 1$, the Hamiltonian exhibits temporal independence: $\partial H / \partial t = 0$. Along the optimal trajectory, the total time derivative of the Hamiltonian is:

$$\frac{dH}{dt} = \frac{\partial H}{\partial \mathbf{u}} \cdot \dot{\mathbf{u}} \quad (2.23)$$

If the control appears linearly in the Hamiltonian (as is the case for spacecraft dynamics, shown in section 2.5), $\partial H/\partial \mathbf{u}$ is independent of \mathbf{u} , and thus the Hamiltonian remains constant along continuous segments of the optimal trajectory. At switching times where the control is discontinuous, the Hamiltonian remains continuous [14]. Consequently:

$$H(\mathbf{x}^*(t), \mathbf{u}^*(t), \boldsymbol{\lambda}^*(t), t) = H_0 = \text{constant} \quad (2.24)$$

The transversality condition (2.20) for free terminal time with $\Phi = 0$ and terminal constraints that do not depend explicitly on time ($\partial \Psi / \partial t = 0$) requires $H(\mathbf{x}^*(t_f), \mathbf{u}^*(t_f), \boldsymbol{\lambda}^*(t_f), t_f) = 0$. Therefore, $H = 0$ along the entire optimal trajectory:

$$1 + \boldsymbol{\lambda}^T \mathbf{f}(\mathbf{x}^*, \mathbf{u}^*, t) = 0 \quad (2.25)$$

The bang-bang structure of time-optimal control emerges from the linear appearance of control in the Hamiltonian. For spacecraft attitude dynamics, the dynamics \mathbf{f} can be partitioned such that the Hamiltonian assumes the form:

$$H = H_0(\mathbf{x}, \boldsymbol{\lambda}, t) + \sum_{i=1}^m S_i(t) u_i \quad (2.26)$$

where $S_i(t)$ are switching functions extracted from the costate-dynamics coupling, u_i denotes the i -th control component, and H_0 denotes the control-independent portion of the Hamiltonian. The minimisation condition (2.18) requires minimising $\sum_{i=1}^m S_i(t) u_i$ subject to $|u_i| \leq u_{i,\max}$. This is achieved by:

$$u_i^*(t) = \begin{cases} u_{i,\max} & \text{if } S_i(t) < 0 \\ u_{i,\min} & \text{if } S_i(t) > 0 \\ \text{undefined} & \text{if } S_i(t) = 0 \end{cases} \quad (2.27)$$

For symmetric control bounds ($u_{i,\min} = -u_{i,\max}$), this reduces to $u_i^*(t) = -u_{i,\max} \operatorname{sgn}(S_i(t))$, confirming the bang-bang structure wherein each control component saturates at its extreme values.

When $S_i(t) = 0$ at an isolated instant, a switch occurs. If $S_i(t) = 0$ over a finite time interval, a singular arc exists. Singular arcs require higher-order analysis through successive time derivatives of the switching function ($S_i = \dot{S}_i = \ddot{S}_i = \dots = 0$) and satisfaction of the generalised Legendre-Clebsch condition for optimality [15]. However, for spacecraft attitude control with torque-limited actuators, singular arcs do not occur due to the linear appearance of control in the dynamics, sufficient controllability of the system, and the time-minimisation objective that drives controls to their extremes [3].

2.3 Trajectory Optimisation Methods

Two primary methodological frameworks exist for solving OCPs: indirect methods that apply PMP to obtain necessary conditions for optimality, and direct methods that discretise the continuous-time problem into a finite-dimensional NLP. While indirect methods offer theoretical insight into the optimal solution structure through the explicit computation of costate trajectories, they suffer from severe initialisation sensitivity and narrow convergence basins. Direct transcription proves more robust to initialisation at the cost of solution accuracy. This section examines the relevance of both approaches to real-time time-optimal control.

2.3.1 Indirect Methods

Indirect methods derive from the necessary conditions established by PMP in section 2.2.2. The approach transforms the optimal control problem into a TPBVP by introducing costate variables and applying the optimality conditions (2.16)–(2.20). The resulting TPBVP comprises forward

integration of the state equations (2.16) from initial conditions $\mathbf{x}(t_0) = \mathbf{x}_0$, backward integration of the costate equations (2.17) from terminal conditions specified by the transversality conditions (2.19), and pointwise determination of optimal control through the minimisation condition (2.18).

Several computational techniques exist for solving the TPBVP. Single shooting methods guess initial costate values $\boldsymbol{\lambda}(t_0)$, integrate the coupled state-costate system forward in time, and iteratively adjust $\boldsymbol{\lambda}(t_0)$ until terminal conditions are satisfied. Multiple shooting partitions the time horizon into segments, integrating each segment independently and enforcing continuity constraints at segment boundaries. Collocation methods approximate state and costate trajectories using polynomial basis functions and minimise residuals of the differential equations at collocation points. Continuation methods gradually transition from a simpler, more easily solved problem to the target problem by varying a homotopy parameter [15].

Indirect methods offer several theoretical and computational advantages. Upon convergence, they satisfy the necessary conditions for optimality exactly, achieving high solution accuracy. The formulation provides direct insight into optimal solution structure through the costate trajectories and switching functions. For problems where the bang-bang control structure is known *a priori*, the switching function framework naturally handles control discontinuities. When analytical expressions for costate derivatives are available, evaluation of the costate equation (2.17) can be computationally efficient. Furthermore, single shooting methods optimise only the initial costate values, resulting in lower-dimensional search spaces compared to discretising entire state and control trajectories.

However, indirect methods suffer from severe practical limitations that have restricted their adoption for real-time optimal control. The TPBVP exhibits extreme sensitivity to initial guesses for the costate variables, with convergence requiring values within a typically small basin of attraction [15]. The costate variables lack direct physical interpretation, making intelligent initialisation difficult. Incorporating path constraints or inequality constraints substantially complicates the necessary conditions, requiring complementarity conditions and active-set determination. Extending multiple-phase problems with discontinuous state or control profiles increases the formulation complexity. The limited robustness to problem variations necessitates re-tuning for each new configuration.

Despite their theoretical elegance and potential for high-accuracy solutions, these computational challenges and initialisation sensitivities have limited the adoption of indirect methods for practical real-time systems. Indirect methods remain most appropriate for problems where the solution structure is well-understood, good initialisation is available through physical insight or continuation from related problems, high accuracy is paramount, and computation time is not a critical factor.

2.3.2 Direct Transcription Methods

Direct transcription methods discretise the continuous-time optimal control problem into a finite-dimensional NLP problem. This approach relaxes the strict necessary conditions of optimality required by indirect methods, instead seeking an approximate solution to the discretised problem that can be improved through mesh refinement. The fundamental advantage of direct methods lies in their ability to leverage mature NLP solver infrastructure developed for general-purpose constrained optimisation [15]. Direct transcription has become the dominant approach for real-time optimal control applications due to larger convergence basins, easier initialisation, and natural accommodation of path constraints.

Direct Shooting

Direct shooting discretises only the control trajectory, obtaining state trajectories through forward integration of the dynamics. The time interval $[t_0, t_f]$ is partitioned into a grid of N points, $\{t_0, t_1, \dots, t_N = t_f\}$, and control values \mathbf{u}_k at grid points k become optimisation variables. Between grid points, the control is parameterised as piecewise constant, piecewise linear, or using higher-order polynomial basis functions. For each candidate control trajectory, the dynamics (2.13)

are integrated forward from the initial condition $\mathbf{x}(t_0) = \mathbf{x}_0$ to obtain the state trajectory. The objective function and constraints are then evaluated based on the resulting states.

Direct shooting offers the advantage of requiring a low number of decision variables, as only control values are optimised while states are implicitly determined through integration. The method is straightforward to implement using standard ODE integrators. However, the approach generates dense constraint Jacobians, as each control variable influences all subsequent states through the integration process. Direct shooting provides no direct control over intermediate state values, which can potentially lead to large constraint violations during optimisation iterations. These limitations have led to a preference for alternative direct transcription methods that discretise both states and controls.

Direct Multiple Shooting

Direct multiple shooting partitions the time horizon into N segments $[t_k, t_{k+1}]$ for $k = 0, 1, \dots, N-1$. Both state and control variables at segment boundaries become optimisation variables. Within each segment, the dynamics are integrated forward from the initial state \mathbf{x}_k using control \mathbf{u}_k to obtain a predicted terminal state. Denoting the state obtained by integrating the dynamics from \mathbf{x}_k with control \mathbf{u}_k over interval $[t_k, t_{k+1}]$ as $\gamma_k(\mathbf{x}_k, \mathbf{u}_k)$, continuity constraints enforce consistency between segments:

$$\mathbf{x}_{k+1} - \gamma_k(\mathbf{x}_k, \mathbf{u}_k) = \mathbf{0}, \quad k = 0, 1, \dots, N-1 \quad (2.28)$$

Multiple shooting generates sparse NLP structures characterised by block-diagonal Jacobian matrices and banded Hessian matrices. Each continuity constraint (2.28) couples only adjacent segments, resulting in a block-tridiagonal structure. This sparsity can be exploited by specialised linear solvers within the NLP algorithm, substantially reducing computational cost for large-scale problems [15]. The method exhibits favourable convergence properties, as intermediate state variables can be initialised to physically reasonable values independently of the control trajectory. Multiple shooting naturally enables parallelisation: segment integrations can be performed concurrently on multi-core processors or distributed computing systems. The computational efficiency for long time horizons and natural decomposition makes multiple shooting well-suited for real-time applications.

Numerical Integration Schemes

The choice of integration method for propagating dynamics within shooting intervals has a significant impact on accuracy, stability, and computational cost. Integration schemes are broadly classified as explicit or implicit methods, each exhibiting distinct computational characteristics and stability properties relevant to spacecraft attitude dynamics.

Explicit integration methods compute the state at the next time step using only information from the current and previous time steps. The forward Euler method represents the simplest explicit scheme. For the dynamical system $\dot{\mathbf{x}} = \mathbf{f}(\mathbf{x}, \mathbf{u}, t)$ from equation (2.13), forward Euler advances the state from time t_k to $t_{k+1} = t_k + \Delta t$ using:

$$\mathbf{x}_{k+1} = \mathbf{x}_k + \Delta t \mathbf{f}(\mathbf{x}_k, \mathbf{u}_k, t_k) \quad (2.29)$$

where Δt denotes the time step. The method possesses first-order accuracy, with a local truncation error of $O(\Delta t^2)$ and a global error of $O(\Delta t)$ [16]. Forward Euler exhibits a bounded stability region: for the scalar test equation $\dot{x} = \mu x$ with $\mu \in \mathbb{C}$, the method is absolutely stable for $|1 + \Delta t \mu| \leq 1$. This restriction limits the maximum stable step size, particularly for stiff systems characterised by widely separated timescales where eigenvalues with large negative real parts impose severe stability constraints despite the solution evolving primarily on slower timescales governed by eigenvalues closer to zero [16].

The classical fourth-order Runge-Kutta method (RK4) substantially improves accuracy through multiple function evaluations per step. The method computes four intermediate slopes and combines them to achieve fourth-order accuracy:

$$\begin{aligned}\kappa_1 &= \mathbf{f}(\mathbf{x}_k, \mathbf{u}_k, t_k) \\ \kappa_2 &= \mathbf{f}\left(\mathbf{x}_k + \frac{\Delta t}{2} \kappa_1, \mathbf{u}_k, t_k + \frac{\Delta t}{2}\right) \\ \kappa_3 &= \mathbf{f}\left(\mathbf{x}_k + \frac{\Delta t}{2} \kappa_2, \mathbf{u}_k, t_k + \frac{\Delta t}{2}\right) \\ \kappa_4 &= \mathbf{f}(\mathbf{x}_k + \Delta t \kappa_3, \mathbf{u}_k, t_k + \Delta t) \\ \mathbf{x}_{k+1} &= \mathbf{x}_k + \frac{\Delta t}{6} (\kappa_1 + 2\kappa_2 + 2\kappa_3 + \kappa_4)\end{aligned}\tag{2.30}$$

RK4 achieves local truncation error $O(\Delta t^5)$ and global error $O(\Delta t^4)$ [16], enabling accurate integration with substantially larger step sizes than forward Euler for smooth problems. The stability region of RK4 is larger than forward Euler but remains bounded, restricting step size for stiff systems.

Explicit methods offer straightforward implementation requiring only function evaluations of $\mathbf{f}(\mathbf{x}, \mathbf{u}, t)$ without solving nonlinear equations. Parallelisation across multiple shooting segments is trivial, as each segment integration proceeds independently. However, explicit methods impose step size restrictions determined by stability considerations rather than accuracy.

Implicit integration methods evaluate the dynamics function at the next time step, requiring solution of a system of algebraic equations at each integration step. The backward Euler method represents the simplest implicit scheme:

$$\mathbf{x}_{k+1} = \mathbf{x}_k + \Delta t \mathbf{f}(\mathbf{x}_{k+1}, \mathbf{u}_{k+1}, t_{k+1})\tag{2.31}$$

The dependence of the right-hand side on the unknown state \mathbf{x}_{k+1} necessitates solving the implicit equation:

$$\mathbf{x}_{k+1} - \mathbf{x}_k - \Delta t \mathbf{f}(\mathbf{x}_{k+1}, \mathbf{u}_{k+1}, t_{k+1}) = \mathbf{0}\tag{2.32}$$

This nonlinear system is typically solved iteratively using Newton's method or simplified Newton iterations. Despite sharing first-order accuracy with forward Euler ($O(\Delta t)$ global error), backwards Euler possesses fundamentally different stability properties. The method is A-stable: for the scalar test equation $\dot{x} = \mu x$, backward Euler is absolutely stable for all $\Delta t > 0$ when $\text{Re}(\mu) < 0$ [16]. This unconditional stability enables substantially larger time steps for stiff problems without numerical instability.

The computational cost per step for implicit methods exceeds that of explicit methods due to the iterative solution of equation (2.32). Each Newton iteration requires evaluation of the Jacobian matrix $\partial \mathbf{f} / \partial \mathbf{x}$ and solution of a linear system. However, the ability to use much larger step sizes can offset the per-step cost, particularly for problems where accuracy requirements permit coarse temporal resolution but stability constraints would restrict explicit methods to prohibitively small steps.

Adaptive step-size methods automatically adjust step sizes based on local error estimates, balancing accuracy and computational cost. This gain comes at the cost of higher complexity. Nevertheless, there exist options that try to reduce this issue, such as the CVODES solver from the SUNDIALS library. It implements variable-order, variable-step Adams-Moulton and backward differentiation methods with automatic stiffness detection [17, 18]. CVODES provides error-controlled integration that maintains user-specified accuracy tolerances through adaptive step-size and order selection. The solver includes a built-in capability for forward and adjoint sensitivity analysis [19], as well as GPU exploiting features [20], enabling the efficient computation of gradients required for NLP solutions without finite-difference approximations.

Direct Collocation

Direct collocation methods discretise both state and control trajectories at collocation points and approximate trajectories using polynomial representations. The dynamics are enforced at collocation points through defect constraints that penalise deviations from the differential equation. Collocation methods differ primarily in their choice of polynomial basis functions and collocation point locations, which determine approximation accuracy, computational efficiency, and suitability for different boundary condition types.

Hermite-Simpson collocation represents a widely-used local collocation method that partitions the time interval $[t_0, t_f]$ into N subintervals $[t_k, t_{k+1}]$ for $k = 0, 1, \dots, N - 1$. Within each interval, the state trajectory is approximated by a cubic Hermite polynomial constructed from endpoint values and derivatives. The midpoint $t_{k+1/2} = (t_k + t_{k+1})/2$ serves as the collocation point where dynamics are enforced. Let $\Delta t_k = t_{k+1} - t_k$ denote the interval length. The state approximation satisfies endpoint interpolation conditions:

$$\begin{aligned}\mathbf{x}(t_k) &= \mathbf{x}_k \\ \mathbf{x}(t_{k+1}) &= \mathbf{x}_{k+1}\end{aligned}\tag{2.33}$$

and derivative conditions:

$$\begin{aligned}\dot{\mathbf{x}}(t_k) &= \mathbf{f}(\mathbf{x}_k, \mathbf{u}_k, t_k) \\ \dot{\mathbf{x}}(t_{k+1}) &= \mathbf{f}(\mathbf{x}_{k+1}, \mathbf{u}_{k+1}, t_{k+1})\end{aligned}\tag{2.34}$$

The cubic Hermite interpolant yields the midpoint state approximation:

$$\mathbf{x}_{k+1/2} = \frac{1}{2}(\mathbf{x}_k + \mathbf{x}_{k+1}) + \frac{\Delta t_k}{8} [\mathbf{f}(\mathbf{x}_k, \mathbf{u}_k, t_k) - \mathbf{f}(\mathbf{x}_{k+1}, \mathbf{u}_{k+1}, t_{k+1})]\tag{2.35}$$

The collocation constraint enforces the dynamics at the midpoint:

$$\varsigma_k = \mathbf{f}(\mathbf{x}_{k+1/2}, \mathbf{u}_{k+1/2}, t_{k+1/2}) - \frac{\mathbf{x}_{k+1} - \mathbf{x}_k}{\Delta t_k} = \mathbf{0}\tag{2.36}$$

This defect constraint (2.36) can equivalently be written using Simpson's quadrature rule for the integral of the dynamics:

$$\mathbf{x}_{k+1} = \mathbf{x}_k + \frac{\Delta t_k}{6} [\mathbf{f}(\mathbf{x}_k, \mathbf{u}_k, t_k) + 4\mathbf{f}(\mathbf{x}_{k+1/2}, \mathbf{u}_{k+1/2}, t_{k+1/2}) + \mathbf{f}(\mathbf{x}_{k+1}, \mathbf{u}_{k+1}, t_{k+1})]\tag{2.37}$$

Hermite-Simpson collocation achieves fourth-order local accuracy: the local truncation error is $O(\Delta t_k^5)$ and the global error is $O(\Delta t^4)$ where $\Delta t = \max_k \Delta t_k$ [15]. The method generates sparse constraint structures, as each defect constraint (2.36) couples only three consecutive state variables $\{\mathbf{x}_k, \mathbf{x}_{k+1/2}, \mathbf{x}_{k+1}\}$. This sparsity enables efficient computation for large-scale problems. The local nature of the approximation facilitates adaptive mesh refinement: intervals can be subdivided independently based on local error estimates without affecting the approximation quality in other regions. Hermite-Simpson collocation balances accuracy, computational efficiency, and implementation simplicity, establishing it as a popular choice for aerospace trajectory optimisation [15].

Pseudospectral methods employ global polynomial approximations over the entire time interval, in contrast to the piecewise local polynomials of Hermite-Simpson collocation. The state trajectory is approximated as:

$$\mathbf{x}(t) \approx \sum_{i=0}^N \mathbf{x}_i \mathcal{L}_i(t)\tag{2.38}$$

where $\mathcal{L}_i(t)$ are Lagrange interpolating polynomials satisfying $\mathcal{L}_i(t_j) = \delta_{ij}$ (Kronecker delta), and $\{t_0, t_1, \dots, t_N\}$ are collocation points. The choice of collocation points fundamentally determines the method's convergence properties and computational characteristics.

Pseudospectral methods achieve spectral convergence: for sufficiently smooth solutions, the approximation error decreases faster than any polynomial in the number of collocation points. Specifically, if the solution possesses a continuous derivatives, the error decreases as $O(p^{-a})$ where p is the polynomial degree [15]. This rapid convergence enables high accuracy with relatively few discretisation points compared to low-order local methods.

- **Legendre-Gauss (LG):** Collocation points $\{w_1, \dots, c_p\}$ comprise the p roots of the Legendre polynomial $\mathcal{P}_p(c)$, lying strictly interior to $[-1, 1]$. Endpoints are excluded, requiring direct specification of initial conditions and extrapolation for terminal constraints. Quadrature weights enable exact integration of polynomials up to degree $2p - 1$. Best suited for problems with free terminal states where boundary extrapolation is acceptable [15].
- **Chebyshev-Gauss-Lobatto (CGL):** Collocation points $c_k = \cos(\pi k/p)$ for $k = 0, \dots, p$ comprise the $p + 1$ extrema of the Chebyshev polynomial $\mathcal{C}_p(c)$, including both endpoints $c_0 = 1$ and $c_p = -1$. Quadrature accuracy matches LG at degree $2p - 1$. Direct enforcement of both initial and terminal boundary conditions without extrapolation makes CGL particularly suitable for problems with constrained initial and final states [15].
- **Legendre-Gauss-Radau (LGR):** Collocation points consist of $c_0 = -1$ (initial time) plus p roots of $(\mathcal{P}_p(c) + \mathcal{P}_{p+1}(c))/(1+c)$, yielding $p + 1$ points with initial endpoint included but final endpoint excluded. Direct initial condition enforcement with terminal state extrapolation. Quadrature weights provide exact integration up to degree $2p$, one degree higher than LG or CGL with equivalent interior point count. The asymmetric structure and superior quadrature accuracy make LGR advantageous for initial value problems, and it is employed by GPOPS-II [21], and CGPOPS [7].

Table 2.2 summarises the key differences.

Table 2.2 Comparison of pseudospectral collocation methods for trajectory optimisation.

| Property | LG | CGL | LGR |
|-------------------------|---------------|----------|---------------|
| Number of points | p | $p + 1$ | $p + 1$ |
| Initial point included | No | Yes | Yes |
| Final point included | No | Yes | No |
| Quadrature accuracy | $2p - 1$ | $2p - 1$ | $2p$ |
| Initial BC enforcement | Direct | Direct | Direct |
| Terminal BC enforcement | Extrapolation | Direct | Extrapolation |

Pseudospectral methods generate dense NLP structures due to high connectivity between variables through the polynomial basis functions. This density increases computational cost for sparse linear algebra operations within NLP solvers, but can be compensated by the lower amount of discretisation points required to achieve convergence, especially for smooth, continuously differentiable optimal trajectories. However, collocation methods may struggle to accurately represent bang-bang controls, as the polynomial approximation poorly captures discontinuous switching behaviour. Increasing the polynomial order or refining the mesh near switching points can mitigate this limitation, but it also increases problem dimensionality.

Optimisation Method Selection

Direct transcription methods offer several critical advantages over indirect methods for practical trajectory optimisation. The convergence basins are substantially larger, enabling successful solution from cruder initial guesses. Initialisation is more intuitive, as state and control variables possess direct physical meaning—unlike costate variables in indirect methods. Linear interpolation between

boundary conditions, physically motivated trajectories, or zero controls often suffices as initial guesses for moderately nonlinear problems.

Path constraints and inequality constraints are naturally incorporated as additional constraints in the NLP formulation. Multiple-phase problems with discontinuous states or controls are handled seamlessly by introducing separate variables and constraints for each phase. Direct methods exhibit robustness to problem variations: modifying spacecraft parameters, constraint bounds, or boundary conditions requires no fundamental reformulation. The availability of mature, well-tested NLP solvers such as IPOPT [22] and SNOPT [23] enables reliable solution of large-scale problems. These advantages have established direct transcription as the dominant choice for real-time optimal control implementations.

2.4 Optimisation Variables

Beyond the choice of the transcription method and attitude parameterisation, another strategic decision in problem formulation significantly affects computational performance and solution quality. This choice concerns which specific parameters are used as the optimisation variables. In the previous sections, it was established that in an OCP, it is solved for the optimal control vector $\mathbf{u}_*(t)$ which minimises a certain cost functional \mathcal{J} . Intuitively, said vector is normally defined as the available actuation in a system. This approach is referred to as direct dynamics formulation and is the most commonly used in the available literature. Alternatively, one can resort to inverse dynamics formulation, where the system's state $\mathbf{x}(t)$ becomes the optimisation variable, and the inverse dynamics equations are solved to obtain the required actuation for following the obtained state trajectory. The choice between these formulations affects how constraints are enforced, the structure of the optimisation problem, and the computational efficiency of gradient evaluations. This section describes these two approaches and provides the means for an informed problem-specific selection.

2.4.1 Direct Dynamics Formulation

Direct dynamics follows the conventional formulation, where control inputs are specified, and system states are determined through the forward integration of the governing equations. The control trajectory $\mathbf{u}(t)$ serves as the decision variable vector in the optimisation problem. State trajectories are obtained by integrating the dynamics constraint $\dot{\mathbf{x}} = \mathbf{f}(\mathbf{x}, \mathbf{u})$ from equation (2.13) subject to initial conditions $\mathbf{x}(t_0) = \mathbf{x}_0$. Control bounds $u_{i,\min} \leq u_i \leq u_{i,\max}$ are naturally enforced as box constraints in the NLP formulation.

However, boundary conditions on states must be explicitly enforced through equality or inequality constraints in the optimisation problem. For problems with fixed terminal states $\mathbf{x}(t_f) = \mathbf{x}_f$, these constraints couple the entire trajectory through the dynamics integration. Path constraints on states, when present, similarly require explicit formulation of constraints. The direct dynamics approach represents the standard formulation employed in most trajectory optimisation implementations and integrates naturally with direct transcription frameworks discussed in section 2.3.2.

Within direct dynamics formulations, two fundamentally different approaches exist for parameterising control trajectories: the more common full control trajectory optimisation, where the whole control vector is used as the decision variable, allowing for full solution structure freedom, and bang-bang parameterisation, known as Switch Time optimisation (STO), which exploits problems where it is known *a priori* that the optimal control trajectory has a bang-bang structure.

Full Trajectory Optimisation

Full trajectory optimisation treats control values at each discretisation point as independent decision variables. No *a priori* structure is imposed on the control profile, granting the optimiser complete freedom to determine the control history. For a problem discretised at N points with m control

inputs, the decision variable count is $O(N \times m)$. This general approach accommodates arbitrary optimal control structures, including singular arcs, continuously varying controls, and complex switching patterns.

However, full trajectory optimisation requires the NLP solver to discover the bang-bang structure inherent in time-optimal problems: a discovery that may require many iterations and careful initialisation. The high dimensionality increases computational expense, particularly for fine discretisations needed to resolve control discontinuities accurately. The optimiser must determine both switching times and control magnitudes, despite the knowledge from section 2.2.3 that optimal controls saturate at bounds. Grid resolution must be sufficiently fine to capture rapid switching, potentially requiring hundreds of discretisation points for problems with multiple switches per axis.

Bang-bang Parameterisation

The STO approach exploits the theoretical result from equation (2.27) that time-optimal control with bounded authority exhibits bang-bang structure in the absence of singular arcs. Rather than optimising control magnitudes at each time point, this approach parameterises the control trajectory by switching times $\mathbf{t}_i = [t_i^{(1)}, t_i^{(2)}, \dots, t_i^{(y)}]$ and initial control directions $s_i \in \{-1, +1\}$ for each control channel i . Between switching times, each control component remains at its extreme value with sign reversals at each subsequent switching time. For problems with y switches per control axis, STO represents a dramatic dimensionality reduction compared to full trajectory optimisation: $O(y \times m)$ versus $O(N \times m)$ where typically $y \ll N$. This reduction substantially decreases computational cost and can improve convergence reliability by eliminating the need for the solver to discover the bang-bang structure.

However, STO introduces implementation complexities beyond this dimensionality advantage. The discrete control direction variables $s_i \in \{-1, +1\}$ present incompatibility with gradient-based NLP solvers, which operate on continuous decision variables. For m independent control axes, 2^m possible initial direction combinations exist. Different approaches address this discrete optimisation component:

- **Exhaustive enumeration** solves the continuous switching time problem for all 2^m sign combinations and selects the globally optimal solution, guaranteeing global optimality at multiplicative computational cost.
- **Relaxation** to continuous variables $s_i \in [-1, +1]$ followed by post-processing conversion to ± 1 enables gradient-based optimisation but provides no optimality guarantees for the converted solution and can lead to solver instabilities for values close to the midpoint due to constant switching.
- **Heuristic determination** based on initial and final state analysis. May fail to identify globally optimal sign configurations [3, 24].

The switching time variables must satisfy temporal ordering constraints $t_0 < t_i^{(1)} < t_i^{(2)} < \dots < t_i^{(y)} < t_f$ to maintain physical consistency. These $O(y)$ inequality constraints can become active during optimisation, potentially complicating convergence. Constraint violations during intermediate iterations result in non-physical control histories, which degrade solver performance.

Reconstruction of the continuous-time control trajectory from discrete switching times involves non-smooth operations incompatible with gradient-based optimisation. The control law for each axis i is:

$$u_i(t, \mathbf{t}_i, s_i) = s_i \cdot (-1)^{C_{\text{sw}}(t, \mathbf{t}_i)} \cdot u_{i,\max} \quad (2.39)$$

where $C_{\text{sw}}(t, \mathbf{t}_i) = |\{t_i^{(j)} : t_i^{(j)} < t\}|$ counts switches occurring before time t . This operation introduces discontinuities at each switching instant, making the controls non-differentiable and violating smoothness requirements of gradient-based NLP solvers [15].

To address this non-differentiability, practical implementations often employ smoothing techniques to approximate the discontinuous switching behaviour through differentiable functions, such as sigmoid or hyperbolic tangent functions. This regularisation represents a fundamental compromise between fidelity to theoretical bang-bang structure and computational tractability [25].

The requirement for *a priori* specification of switch count remains a fundamental limitation. An insufficient switch count yields suboptimal solutions that are unable to reach the true optimum; an excessive switch count may cause convergence failure or generate spurious switches. Iterative approaches with incrementally increasing switch counts enable empirical determination of optimal v at multiplicative computational expense.

2.4.2 Inverse Dynamics Formulation

Inverse dynamics reverses the problem structure by treating the state trajectory $\mathbf{x}(t)$ as the primary decision variable and computing the required control inputs through the inversion of the system dynamics. The state trajectory is parameterised using M basis function expansions such as B-splines, polynomial series, or Fourier series. Common parameterisations include:

$$\mathbf{x}(t) = \sum_{j=0}^M \mathbf{b}_j \chi_j(t) \quad (2.40)$$

where $\chi_j(t)$ are basis functions and \mathbf{b}_j are coefficient vectors serving as optimisation variables.

The time derivative of the parameterised state trajectory is computed analytically:

$$\dot{\mathbf{x}}(t) = \sum_{j=0}^M \mathbf{b}_j \dot{\chi}_j(t) \quad (2.41)$$

For systems where the dynamics can be written in the affine control form:

$$\dot{\mathbf{x}} = \mathbf{f}_0(\mathbf{x}) + \mathbf{G}(\mathbf{x})\mathbf{u} \quad (2.42)$$

where $\mathbf{f}_0(\mathbf{x})$ represents drift dynamics and $\mathbf{G}(\mathbf{x}) \in \mathbb{R}^{n \times m}$ is the control influence matrix, the required control can be computed through algebraic inversion:

$$\mathbf{u}(t) = \mathbf{G}(\mathbf{x}(t))^{-1} [\dot{\mathbf{x}}(t) - \mathbf{f}_0(\mathbf{x}(t))] \quad (2.43)$$

provided that $\mathbf{G}(\mathbf{x})$ is full rank. For underactuated systems where $m < n$, the pseudoinverse \mathbf{G}^\dagger replaces the standard inverse, though this introduces additional complexity in ensuring trajectory feasibility.

The inverse dynamics formulation offers significant advantages for satisfying boundary conditions. State boundary conditions at initial and terminal times can be enforced directly through the basis function coefficients in equation (2.40). For polynomial or spline representations, linear equality constraints on coefficients suffice to ensure $\mathbf{x}(t_0) = \mathbf{x}_0$ and $\mathbf{x}(t_f) = \mathbf{x}_f$ regardless of optimisation progress [26]. This automatic satisfaction of state boundary conditions eliminates a class of potentially difficult nonlinear constraints from the NLP formulation.

Analytical differentiation of smooth basis functions yields exact expressions for state derivatives, eliminating numerical differentiation errors. Higher-order derivatives required for acceleration-dependent dynamics can be computed symbolically from the basis functions. Gradient computation for the optimisation algorithm benefits from the explicit relationship between decision variables (basis coefficients) and the objective function, enabling efficient symbolic or automatic differentiation of the entire problem. Nevertheless, solution quality depends on how well the selected basis function approximates the actual system dynamics. Additionally, inverse dynamics introduces the fundamental challenge of ensuring control feasibility. The computed controls from equation (2.43) may

violate actuator constraints for arbitrary choices of trajectory parameterisation. Aggressive trajectories or poorly conditioned basis function selections can result in required control magnitudes exceeding physical actuator capabilities.

For spacecraft reorientation problems, Euler's rotational equations (2.6) provide the affine control structure with control torques entering linearly and equation (2.4) defines the inverse dynamics. However, the bang-bang nature of the time-optimal solution drives the required torques to the actuator limits, necessitating careful selection of basis functions and iterative refinement to maintain control feasibility throughout the full trajectory.

2.4.3 Selection Criteria and Trade-Offs

The choice between formulation strategies depends on problem characteristics and computational requirements. For problems where the optimal switching structure is known from prior analysis or analytical results, bang-bang parameterisation offers substantial computational advantages. When the switching structure is unknown or problem-dependent, full trajectory optimisation provides greater generality at a higher computational cost. The selection between direct and inverse dynamics formulations involves trade-offs between constraint handling complexity, problem dimensionality, and computational efficiency. Direct dynamics naturally handles control constraints but requires explicit enforcement of state boundary conditions through potentially nonlinear constraints. Inverse dynamics automatically satisfy state boundary conditions but introduce complexity in enforcing control feasibility. For problems where state boundary conditions are numerous or complex, inverse dynamics can reduce the overall difficulty of the problem, despite the challenge of control feasibility. Conversely, when control bounds are tight and state boundary conditions are simple, direct dynamics often prove more efficient [26, 24].

Additional factors include available computational resources (offline optimisation permits more expensive methods), required solution accuracy (high-fidelity solutions may justify increased computational cost), tolerance for implementation complexity (inverse dynamics requires careful parameterisation design), and real-time performance requirements (necessitating efficient formulations and potentially structure-exploiting methods). The formulation strategy should align with the specific application requirements and available computational infrastructure, striking a balance between optimality, reliability, and computational efficiency.

2.5 Time-Optimal Spacecraft Attitude Manoeuvres

The application of optimal control theory to spacecraft reorientation problems combines the rigid body dynamics established in section 2.1 with the theoretical framework presented in sections 2.2 to 2.4. Time-optimal spacecraft attitude control has evolved from early analytical studies on simplified configurations to sophisticated numerical methods capable of handling arbitrary manoeuvres in real time. The problem exhibits significant complexity arising from nonlinear gyroscopic coupling, nonconvex optimisation landscapes, and the bang-bang control structure predicted by PMP. Historical developments have established analytical characterisations for specific cases while revealing fundamental limitations that necessitate numerical solution approaches. This section traces the historical evolution of time-optimal spacecraft reorientation research, presents the complete mathematical problem formulation, derives the optimal control characterisation through application of PMP, and analyses the factors contributing to problem complexity and computational difficulty.

2.5.1 Historical Development

The theoretical foundations for time-optimal spacecraft attitude control trace back to the establishment of PMP in 1962 [14], which provided the first rigorous framework for characterising optimal control trajectories subject to bounded control authority. The principle demonstrates that for systems where control appears linearly and no singular arcs exist, optimal trajectories exhibit a

bang-bang structure, i.e., switching between extreme control values a finite number of times. These early theoretical developments focused on simplified spacecraft configurations to enable analytical tractability.

Initial spacecraft attitude studies in the 1960s and 1970s concentrated on idealised cases: symmetric spacecraft with three equal principal moments of inertia ($J_1 = J_2 = J_3$), rest-to-rest manoeuvres with zero initial and final angular velocities ($\omega_0 = \omega_f = \mathbf{0}$), and systems with zero net angular momentum. These simplifications enabled analytical or semi-analytical solution techniques but provided limited insight into general spacecraft configurations. A common assumption during this period was that time-optimal manoeuvres would follow eigenaxis rotations, which are single-axis rotations aligned with a principal axis of inertia. This assumption appeared physically intuitive, as eigenaxis rotations avoid gyroscopic coupling and enable independent control of angular velocity about a single axis.

The 1990s witnessed key breakthroughs that fundamentally altered the understanding of time-optimal spacecraft control. Bilimoria and Wie's seminal 1993 contribution [3] demonstrated that eigenaxis manoeuvres are not time-optimal for spacecraft with independent three-axis control authority, $|\tau_i| \leq \tau_{i,\max}$, also known as cubically constrained control. By allowing simultaneous torque application about multiple axes, the spacecraft can utilise gyroscopic coupling to achieve faster reorientations than those achieved through single-axis rotations. Their analysis of symmetric spacecraft revealed that optimal switching structures depend critically on the magnitude of the manoeuvre angle. For rotations exceeding 72° , they identified a specific five-switch structure as the optimal solution. For rotations below 72° , they initially proposed a seven-switch structure, though this was later refined by Bai and Junkins [4]. This work represented a mindset shift: rather than avoiding gyroscopic effects, optimal control actively exploits coupling dynamics to minimise manoeuvre time. When the total torque magnitude is constrained instead of each individual element, $\|\boldsymbol{\tau}\| \leq \tau_{\max}$, known as spherically constrained control, eigenaxis rotation remains the time-optimal manoeuvre.

Byers extended Bilimoria and Wie's results to fully asymmetric spacecraft in 1996 [9], analysing asymmetric spacecraft configurations where all three principal moments of inertia are distinct ($J_1 \neq J_2 \neq J_3$). Gyroscopic coupling terms in Euler's equations (2.5) introduce additional complexity, as each axis influences the dynamics of the others through products of angular velocity components. Byers characterised how inertia ratios affect both switching times and bang-bang control profiles, demonstrating that spacecraft asymmetry influences not only the optimal control structure but also the convergence properties of numerical solution methods. Highly asymmetric configurations with large disparities in principal moments exhibit more complex switching patterns and present greater challenges for gradient-based optimisation algorithms.

Recent advances from the 2000s through 2010s have refined the understanding of small-angle manoeuvres and enabled the solution of increasingly general problems. Bai and Junkins discovered in 2009 [4] that rotations below 72° admit an improved six-switch structure, contradicting the earlier seven-switch proposal and demonstrating that even well-studied problems can yield new optimal solutions through careful analysis. Concurrently, developments in direct transcription methods and nonlinear programming solvers have enabled numerical solution of time-optimal problems for arbitrary spacecraft configurations, including track-to-track manoeuvres with non-zero initial and final angular velocities. Modern research emphasises efficient algorithms suitable for onboard real-time implementation, including structure-exploiting optimisation methods and intelligent initialisation strategies that improve convergence reliability.

The evolution from analytical characterisation of simplified cases to fully numerical approaches for general configurations reflects both increasing computational capabilities and recognition of fundamental analytical intractability for arbitrary manoeuvres. The contemporary focus has shifted from theoretical analysis to practical deployment, developing algorithms that balance near-optimality with computational efficiency sufficient for real-time trajectory generation aboard resource-constrained spacecraft processors.

2.5.2 Problem Formulation

The complete optimal control problem statement for time-optimal spacecraft reorientation integrates the attitude dynamics from section 2.1 with the theoretical framework from section 2.2. When quaternions are used for attitude parametrisation, the state vector looks like:

$$\mathbf{x} = \begin{bmatrix} \mathbf{q} \\ \boldsymbol{\omega} \end{bmatrix} \in \mathbb{R}^7 \quad (2.44)$$

The control vector consists of torques applied about the principal axes:

$$\mathbf{u} = \boldsymbol{\tau} \quad (2.45)$$

The system dynamics combine the quaternion kinematics from equation (2.8) with Euler's rotational equations from equation (2.6):

$$\dot{\mathbf{x}} = \mathbf{f}(\mathbf{q}, \boldsymbol{\omega}, \boldsymbol{\tau}) = \begin{bmatrix} \frac{1}{2}\boldsymbol{\Omega}(\boldsymbol{\omega})\mathbf{q} \\ \mathbf{J}^{-1}[\boldsymbol{\tau} - \boldsymbol{\omega} \times \mathbf{J}\boldsymbol{\omega}] \end{bmatrix} \quad (2.46)$$

Actuator limitations define the admissible control set:

$$\mathcal{U} = \{\boldsymbol{\tau} \in \mathbb{R}^3 : |\tau_i| \leq \tau_{i,\max}, i = 1, 2, 3\} \quad (2.47)$$

where $\tau_{i,\max}$ represents the maximum torque magnitude available about the i -th principal axis. The constraints may be uniform ($\tau_{1,\max} = \tau_{2,\max} = \tau_{3,\max}$) or axis-dependent, reflecting different actuator capabilities for different axes.

Boundary conditions specify the initial and terminal spacecraft states. The initial condition prescribes both attitude and angular velocity:

$$\mathbf{x}(t_0) = \begin{bmatrix} \mathbf{q}_0 \\ \boldsymbol{\omega}_0 \end{bmatrix} \quad (2.48)$$

Similarly, the terminal condition specifies the desired final state:

$$\mathbf{x}(t_f) = \begin{bmatrix} \mathbf{q}_f \\ \boldsymbol{\omega}_f \end{bmatrix} \quad (2.49)$$

Due to the double cover property of the quaternion representation, both \mathbf{q}_f and $-\mathbf{q}_f$ correspond to the same physical terminal orientation. However, these two mathematically equivalent representations yield fundamentally different optimal trajectories. If the solver does not account for this ambiguity, the optimisation may converge to an undesirable equilibrium that requires rotation through angles exceeding 180° , a phenomenon known as quaternion unwinding. To ensure convergence to the time-optimal solution, the terminal quaternion must be selected such that:

$$\mathbf{q}_0^T \mathbf{q}_f \geq 0 \quad (2.50)$$

This condition guarantees that the rotation angle is less than 180° , corresponding to the shortest rotational path on $\text{SO}(3)$. This constraint can be enforced during problem initialisation by evaluating $\mathbf{q}_0^T \mathbf{q}_f$ and replacing $\mathbf{q}_f = -\mathbf{q}_f$ if the inner product is negative. This preprocessing step is computationally trivial yet essential for obtaining globally optimal time-minimal trajectories [10].

Alternatively, one can compute the relative rotation required with equation (2.51), where \mathbf{q}_0^- is the quaternion conjugate of \mathbf{q}_0 and \otimes denotes quaternion multiplication.

$$\mathbf{q}_{\text{rot}} = \mathbf{q}_f \otimes \mathbf{q}_0^- \quad (2.51)$$

This transformation approach exploits the group structure of unit quaternions. By formulating the problem in terms of the relative rotation \mathbf{q}_{rot} , the optimisation always starts from the identity quaternion $\mathbf{q}_I = [1 \ 0 \ 0]^T$, which can simplify initialisation and improve numerical conditioning. The trajectory is then mapped back to the physical frame via quaternion composition:

$$\mathbf{q}(t) = \mathbf{q}^*(t) \otimes \mathbf{q}_0 \quad (2.52)$$

where $\mathbf{q}^*(t)$ is the optimal quaternion trajectory in the optimisation frame.

2.5.3 Optimal Control Characterisation

The objective functional for time-optimal control minimises the manoeuvre duration:

$$\mathcal{J} = t_f - t_0 \quad (2.53)$$

subject to dynamics constraint (2.46), control bounds (2.47), and boundary conditions (2.48)–(2.49).

The quaternion unit norm constraint requires special consideration within the optimisation framework. Three primary approaches exist for enforcing $\|\mathbf{q}(t)\| = 1$: explicit normalisation projects the quaternion onto the unit sphere after each integration step; penalty methods augment the objective function with terms penalizing norm deviations; direct enforcement incorporates $\|\mathbf{q}\| = 1$ as an algebraic constraint within the NLP formulation [10]. The choice of constraint handling method influences both computational efficiency and numerical conditioning of the optimisation problem.

The problem constitutes a nonlinear, nonconvex, control-constrained optimal control problem. Nonlinearity arises from the gyroscopic coupling terms in Euler's equations and the bilinear structure of quaternion kinematics. Nonconvexity arises from the rotational manifold structure and the bang-bang control switching, resulting in multiple local minima in the optimisation landscape.

Application of PMP to the spacecraft attitude control problem yields the necessary conditions for time-optimal trajectories. The Hamiltonian for spacecraft attitude dynamics, following equation (2.21), takes the form:

$$H = 1 + \boldsymbol{\lambda}^T \mathbf{f}(\mathbf{q}, \boldsymbol{\omega}, \boldsymbol{\tau}) \quad (2.54)$$

where $\boldsymbol{\lambda} \in \mathbb{R}^7$ represents the costate vector partitioned into components corresponding to attitude and angular velocity:

$$\boldsymbol{\lambda} = \begin{bmatrix} \boldsymbol{\lambda}_q \\ \boldsymbol{\lambda}_\omega \end{bmatrix} \quad (2.55)$$

Expanding the Hamiltonian using the spacecraft dynamics (2.46) yields:

$$H = 1 + \frac{1}{2} \boldsymbol{\lambda}_q^T \boldsymbol{\Omega}(\boldsymbol{\omega}) \mathbf{q} + \boldsymbol{\lambda}_\omega^T \mathbf{J}^{-1} [\boldsymbol{\tau} - \boldsymbol{\omega} \times \mathbf{J} \boldsymbol{\omega}] \quad (2.56)$$

The costate differential equations follow from equation (2.17). For time-optimal problems with $L = 1$, the costate equations reduce to:

$$\dot{\boldsymbol{\lambda}} = - \left(\frac{\partial \mathbf{f}}{\partial \mathbf{x}} \right)^T \boldsymbol{\lambda} \quad (2.57)$$

The Jacobian $\partial \mathbf{f} / \partial \mathbf{x}$ couples the kinematic and dynamic equations, requiring evaluation of derivatives of both quaternion kinematics and Euler's rotational equations with respect to attitude and angular velocity.

The switching function emerges from the linear appearance of control torques in the Hamiltonian. Extracting terms involving $\boldsymbol{\tau}$ from equation (2.56):

$$H = H_0(\mathbf{q}, \boldsymbol{\omega}, \boldsymbol{\lambda}_q, \boldsymbol{\lambda}_\omega) + \boldsymbol{\lambda}_\omega^T \mathbf{J}^{-1} \boldsymbol{\tau} \quad (2.58)$$

where H_0 encompasses all terms independent of control. Defining the switching function:

$$\mathbf{S}(t) = \mathbf{J}^{-1} \boldsymbol{\lambda}_\omega(t) \quad (2.59)$$

enables rewriting the Hamiltonian as:

$$H = H_0 + \mathbf{S}^T \boldsymbol{\tau} = H_0 + \sum_{i=1}^3 S_i(t) \tau_i \quad (2.60)$$

The minimisation condition (2.18) requires minimising $\sum_{i=1}^3 S_i(t) \tau_i$ subject to control bounds $|\tau_i| \leq \tau_{i,\max}$. Since the sum is linear in each control component, the minimum occurs at the boundary of the admissible set. For each axis independently:

$$\tau_i^*(t) = \begin{cases} -\tau_{i,\max} & \text{if } S_i(t) > 0 \\ +\tau_{i,\max} & \text{if } S_i(t) < 0, \quad i = 1, 2, 3 \\ \text{undefined} & \text{if } S_i(t) = 0 \end{cases} \quad (2.61)$$

which can be written compactly as:

$$\tau_i^*(t) = -\tau_{i,\max} \cdot \text{sgn}(S_i(t)), \quad i = 1, 2, 3 \quad (2.62)$$

This result confirms the bang-bang structure anticipated by PMP: each torque component saturates at its extreme value ($\pm\tau_{i,\max}$) with the sign determined by the corresponding switching function component.

The switching function admits physical interpretation. From equation (2.59), $\mathbf{S}(t) = \mathbf{J}^{-1} \boldsymbol{\lambda}_\omega(t)$ represents the inertia-weighted costate on angular velocity dynamics. The sign of each component $S_i(t)$ determines the optimal torque direction about the i -th principal axis: positive switching function values drive the torque to its negative extreme, while negative values drive the torque in the positive direction. Zero-crossings of the switching function, where $S_i(t)$ changes sign, determine switching instants at which the optimal control transitions between extreme values.

The switching function evolution is governed by the costate trajectory, which depends on the state trajectory through the costate equations (2.57). The state trajectory, in turn, depends on the applied control through the dynamics (2.46). This circular dependency, where the costate affects the switching function, the switching function determines the control, the control drives the state, and the state influences the costate, necessitates the simultaneous solution of the forward state equations and the backward costate equations. The resulting TPBVP couples conditions at the initial time (state specified) and the final time (costate determined by transversality conditions), presenting the fundamental computational challenge of indirect optimal control methods.

2.6 Computational Methods and Implementation

The practical implementation of direct transcription methods for spacecraft attitude control requires sophisticated computational infrastructure, encompassing numerical optimisation algorithms, software frameworks, and initialisation strategies. Many different solvers exist to solve OCP's, each adapted for specific transcription methods, problem structures, and applications. This section examines the computational methods that enable efficient trajectory optimisation. Section 2.6.1 analyses gradient-based nonlinear programming solvers, distinguishing general-purpose algorithms from structure-exploiting approaches and convexification-based methods. Section 2.6.2 surveys software frameworks providing problem formulation interfaces and automatic differentiation. Section 2.6.3 examines metaheuristic algorithms for initialisation and global search.

2.6.1 Nonlinear Programming Solvers

Direct transcription converts continuous-time optimal control problems into finite-dimensional NLPs characterised by large-scale sparse structure. For multiple shooting with N shooting intervals and n states, the NLP comprises $N(n + m)$ decision variables, where m denotes the control dimension. The constraint Jacobian exhibits block-sparse structure: dynamics constraints couple only adjacent intervals, creating block-tridiagonal patterns in the Karush-Kuhn-Tucker (KKT) system [27]. Direct collocation generates denser constraint structures due to polynomial approximations coupling multiple collocation points within intervals [15]. Exploitation of this temporal structure differentiates general-purpose sparse NLP solvers from specialised algorithms designed for optimal control. This section examines computational methods for trajectory optimisation, distinguishing between general-purpose algorithms and structure-exploiting approaches.

General-Purpose NLP Solvers

General-purpose solvers treat trajectory optimisation as standard sparse NLP without exploiting temporal structure. Two algorithmic paradigms dominate: interior-point methods and sequential quadratic programming (SQP). These methods apply to arbitrary transcription schemes but achieve computational complexity scaling as $O((Nn)^3)$ due to full KKT matrix factorisation [28].

- **Interior Point Methods:** IPOPT (Interior Point OPTimiser) implements a primal-dual interior-point (IP) method algorithm with filter line search [22]. The filter mechanism maintains non-dominated pairs of constraint violation and objective function values, accepting iterates that improve either metric. This approach demonstrates robust convergence across diverse problem formulations and has been extensively validated in aerospace trajectory optimisation [15]. However, IPOPT factors the full KKT system as a general sparse matrix without recognising the block structure arising from temporal dynamics. For large-horizon problems, factorisation becomes computationally expensive, limiting applicability to offline optimisation and algorithm development.
- **Sequential Quadratic Programming:** SNOPT (Sparse Nonlinear OPTimiser) employs SQP with quasi-Newton Hessian approximation updates [23]. Each iteration solves a quadratic program (QP) approximating the Lagrangian, using gradient information to update the Hessian approximation. The quasi-Newton approach eliminates the need for exact second-derivative computation, thereby reducing costs when automatic differentiation is unavailable. SNOPT maintains superlinear convergence, though slower than Newton methods with exact Hessians. The solver is suitable for preliminary design phases where the cost of derivative computation exceeds the cost of additional iterations [23].

Structure-Exploiting Solvers

Structure-exploiting solvers leverage the block-sparse temporal structure inherent to optimal control problems, achieving computational complexity of $O(Nn^3)$, which is linear in the horizon length [27, 29]. These methods prove particularly effective for multiple shooting formulations, where dynamics constraints couple only adjacent shooting intervals, creating block-tridiagonal KKT systems. The computational advantage increases with horizon length: for $N = 50$ stages with $n = 7$ states (quaternion attitude representation), structure exploitation reduces complexity from $O((350)^3) \approx 43$ million to $O(50 \cdot 343) \approx 17$ thousand operations.

- **Riccati-Based IP:** FATROP (Fast Trajectory optimisation) implements structure-exploiting interior-point optimisation using generalised Riccati recursion [27]. The method recognises block-tridiagonal KKT structure and employs forward-backwards Riccati sweeps rather than general sparse factorisation. The forward pass computes Riccati matrices encoding primal-dual relationships between adjacent stages; the backward pass recursively solves for optimal

state and control trajectories. FATROP handles inequality constraints through an active-set interior-point approach without introducing slack variables, maintaining problem compactness. The solver incorporates exact Hessian information via automatic differentiation, enabling quadratic convergence. Benchmarks demonstrate approximately $10\times$ speedup versus IPOPT for trajectory optimisation problems, suitable for real-time applications [27].

- **Riccati-Based SQP:** The ACADOS framework paired with the HPIPM (High-Performance Interior Point Method) QP solver exploits block-tridiagonal structure via Riccati recursion [30]. The ACADOS-HPIPM combination achieves computational performance comparable to FATROP for multiple shooting problems while providing greater flexibility in transcription method selection [29]. The framework supports automatic differentiation via CasADi [31], enabling the efficient generation of derivatives for arbitrary dynamics formulations.

Sequential Convex Programming

Sequential convex programming (SCP) provides an alternative approach to nonconvex trajectory optimisation through iterative solution of convex approximations [32]. Each SCP iteration linearises nonlinear dynamics, imposes trust region constraints to maintain approximation validity, solves the resulting convex program via second-order cone programming or QP methods, and updates the reference trajectory. SCP has seen limited application to attitude control due to quaternion constraint complexities [32].

Solver Selection Criteria

Solver selection depends on computational requirements, problem characteristics, and the availability of infrastructure. Table 2.3 summarises key characteristics. IPOPT provides maximum reliability for offline trajectory design and algorithm prototyping, with robust convergence across formulations but limited real-time applicability. SNOPT suits scenarios where exact Hessian computation is expensive or during preliminary design phases. Structure-exploiting solvers enable real-time implementation but require specific sparse OCP formulations. FATROP offers simpler integration, while ACADOS provides greater algorithmic flexibility.

Table 2.3 Comparison of NLP solvers for trajectory optimisation.

| Solver | Method | Complexity | Convergence |
|--------------|-------------|-------------|-------------|
| IPOPT | IP | $O((Nn)^3)$ | Quadratic |
| SNOPT | SQP | $O((Nn)^3)$ | Superlinear |
| FATROP | Riccati IP | $O(Nn^3)$ | Quadratic |
| ACADOS-HPIPM | Riccati SQP | $O(Nn^3)$ | Superlinear |

2.6.2 Optimal Control Software Frameworks

Software frameworks bridge domain-specific trajectory optimisation concepts and low-level nonlinear programming abstractions. Key capabilities include intuitive problem specification interfaces, automatic differentiation for gradient computation, integration with multiple solvers, recognition of sparse structures, and efficient function evaluation. Framework selection involves trade-offs between generality, computational efficiency, and implementation complexity.

CasADi: Symbolic Framework

CasADi (Computer Algebra System with Automatic Differentiation) provides foundational infrastructure for modern optimal control [31]. The symbolic framework constructs computational graphs

that represent problem functions, applies algebraic simplifications, determines sparsity patterns, and generates efficient, standalone C code. CasADi supports forward and reverse mode automatic differentiation, producing exact derivatives without finite-difference errors. The framework interfaces with IPOPT, SNOPT, FATROP, and other commercial solvers through unified application programming interfaces (APIs). The Opti stack offers high-level syntax for OCP formulation [33]. CasADi's open-source availability, extensive documentation, and widespread adoption within the aerospace community establish it as a de facto standard infrastructure.

ACADOS: Real-Time Framework

ACADOS (Automatic Control and Dynamic optimisation Suite) targets fast embedded optimal control with emphasis on Model Predictive Control (MPC) [29]. The framework generates templated C code for embedded targets with a fixed memory footprint and minimal runtime overhead. ACADOS implements real-time iteration schemes, structure-exploiting QP solvers (HPIPM, qpOASES), and custom linear algebra kernels optimised for cache performance and vectorisation. Performance targets include millisecond-range computation, suitable for high-rate control loops that exceed 100 Hz. Integration with CasADi enables symbolic differentiation while specialised optimisations address real-time execution requirements. Open-source availability facilitates research and commercial deployment.

GPOPS: Pseudospectral Methods

GPOPS-II (General Purpose OPtimal Control Software) implements hp-adaptive Gaussian quadrature collocation in MATLAB [21]. The framework employs LGR collocation with automatic mesh refinement, adapting interval sizes (h-method) and polynomial orders (p-method) to achieve specified accuracy tolerances. Adaptive capabilities prove valuable for bang-bang problems where mesh concentration near switching times improves efficiency. GPOPS-II interfaces with IPOPT and SNOPT, supporting sparse finite differences, automatic differentiation, or user-supplied derivatives. Wide aerospace adoption has established benchmark solutions for diverse optimal control problems.

CGPOPS provides a C++ implementation of similar algorithms, achieving 2-6 \times speedup over MATLAB through compiled language efficiency [7]. Multiple derivative methods include central finite differences, bicomplex-step differentiation, which eliminates subtraction error, hyper-dual differentiation for exact second derivatives, and automatic differentiation integration. Specialised mesh refinement strategies for bang-bang control include switching detection algorithms and grid concentration near discontinuities. Exact sparsity pattern identification via hyper-dual methods improves computational efficiency. Cross-platform portability and compiled performance make CGPOPS suitable for production deployment.

2.6.3 Derivative-Free Optimisation

Derivative-free methods are applicable in scenarios where gradients are unavailable, unreliable, or computationally expensive to obtain. Metaheuristic algorithms employ stochastic population-based search, while direct search methods use deterministic pattern exploration. Computational cost typically exceeds that of gradient-based approaches by orders of magnitude, offset by the potential for parallelisation and robustness to local minima. One of the most widely used methods is the Particle Swarm Optimisation (PSO), which has gained popularity due to its simple yet effective implementation.

Particle Swarm Optimisation

PSO models collective intelligence through social learning. A population of \mathcal{N} particles maintains positions \mathbf{z}_j and velocities \mathbf{v}_j for every particle j , evolving via:

$$\begin{aligned}\mathbf{v}_j^{k+1} &= w_0 \mathbf{v}_j^k + w_1 r_1 (\boldsymbol{\rho}_j - \mathbf{z}_j^k) + w_2 r_2 (\mathbf{g} - \mathbf{z}_j^k) \\ \mathbf{z}_j^{k+1} &= \mathbf{z}_j^k + \mathbf{v}_j^{k+1}\end{aligned}\quad (2.63)$$

where $\boldsymbol{\rho}_j$ is personal best, \mathbf{g} is global best, w_0 is inertia weight, $w_1, w_2 \geq 0$ are cognitive and social parameters, and $r_1, r_2 \in [0, 1]$ are random numbers. Parameter tuning balances exploration and exploitation: increasing inertia increases solution space exploration, while reducing it allows for refinement of local optima. Cognitive and social parameters weigh individual versus collective learning. Some variations of the traditional PSO use dynamic weights, allowing for better solution space exploration initially, but transitioning to a more precise search for the last iterations to refine the global best solution.

Applications in optimal control mostly include costate initialisation for indirect methods [34] and warm-start generation for gradient-based refinement [35].

For discrete optimisation problems, binary PSO extends the continuous framework to binary decision variables [36]. The velocity update in equation (2.63) remains unchanged, but positions are mapped to binary values through a sigmoid transfer function:

$$\begin{aligned}\mathcal{S}(v_{j,d}^{k+1}) &= \frac{1}{1 + e^{-\alpha v_{j,d}^{k+1}}} \\ z_{j,d}^{k+1} &= \begin{cases} 1 & \text{if } r_d < \mathcal{S}(v_{j,d}^{k+1}) \\ 0 & \text{otherwise} \end{cases}\end{aligned}\quad (2.64)$$

where $\alpha > 0$ is a scaling parameter controlling the sigmoid slope and $r_d \in [0, 1]$ is a random number for each dimension d . The parameter α determines the degree of stochasticity in position updates: larger values produce steeper sigmoid transitions, leading to more deterministic decisions, while smaller values maintain gradual transitions that preserve stochastic behaviour [36].

To prevent complete loss of randomness when velocity values are big, the velocity is clamped $|v_{j,d}| \leq V_{\max}$, where V_{\max} is computed to maintain the sigmoid output within bounds $[1 - \epsilon, \epsilon]$ for a saturation threshold $\epsilon \in [0.5, 1.0]$:

$$V_{\max} = -\frac{1}{\alpha} \ln \left(\frac{1}{\epsilon} - 1 \right) \quad (2.65)$$

Without velocity saturation, unbounded velocities can drive $\mathcal{S}(v_{j,d}) \rightarrow 0$ or $\mathcal{S}(v_{j,d}) \rightarrow 1$, eliminating the probabilistic position update and degrading search performance. For $\epsilon = 1$, the effect of bounding the velocity is nullified, and the decisions are allowed to become deterministic for large velocity values. When $\epsilon = 0.5$, the velocity term loses its influence on the decision for the next position, and the process becomes completely random. Binary PSO finds application in bang-bang control sign selection [24], feature selection, and scheduling problems.

Application Strategy

Although derivative-free methods comprise thousands of function evaluations, suffer from complex parameter tuning, and offer no convergence guarantees, they have found their utility in many different applications due to their global search capability and simple implementation. Additionally, GPU acceleration has enabled order-of-magnitude speedups for parallel function evaluation [37, 38], making them attractive for real-time applications.

Their use in optimal control focuses primarily on initialisation generation [34, 35]. A two-stage approach combines metaheuristic global search to identify promising regions with gradient-based refinement to achieve high accuracy. This hybrid strategy leverages complementary strengths: derivative-free robustness for initialisation and gradient-based efficiency for convergence.

2.7 Efficiency and Reliability

The practical deployment of trajectory optimisation algorithms for spacecraft attitude control requires consideration of both computational efficiency and solution reliability. Reliability, defined as the probability of converging to a feasible and optimal solution from arbitrary initial conditions, critically depends on the quality of initialisation for nonconvex problems. Computational efficiency determines whether algorithms can execute within real-time constraints imposed by on-board processors and operational timelines. The definition of "real-time" varies across spacecraft applications: agile imaging missions may demand sub-second computation, while station-keeping operations permit longer solution horizons. Statistical validation through MC analysis provides essential characterisation of algorithm performance across the operational envelope. This section examines strategies for improving both reliability and efficiency. Section 2.7.1 analyses initialisation strategies ranging from deterministic heuristics to stochastic global search methods. Section 2.7.2 examines GPU acceleration techniques for parallel function evaluation. Section 2.7.3 presents statistical methods for quantifying algorithm reliability across problem parameter spaces.

2.7.1 Initialisation Strategies

Gradient-based NLP solvers converge to local optima from initial guesses within their basins of attraction. Nonconvex trajectory optimisation problems exhibit multiple local minima, with basin sizes and locations depending on problem parameters. Poor initialisation leads to different failure modes, such as convergence failure when iteration limits are exceeded, the generation of infeasible solutions that violate dynamics or boundary conditions, and entrapment in suboptimal local minima distant from the global optimum. Initialisation strategies can be divided into two categories: deterministic approaches that utilise problem-specific knowledge, and stochastic methods that employ global search algorithms.

Deterministic Initialisation

Deterministic strategies construct initial guesses using available information without stochastic sampling. Some examples consist of:

- **Warm-starting from previous solutions** — exploits similarity between sequential optimisation problems by initialising from previously converged trajectories. For parametric studies that vary problem properties incrementally, the optimal solution changes continuously with the parameters. Warm-starting from the solution at nearby parameter values typically ensures convergence with minimal iterations. The approach requires maintaining a solution library or database indexed by problem parameters. Applicability is limited to problems with a similar structure and boundary conditions, as novel manoeuvres or significant parameter changes render previous solutions uninformative.
- **Linear interpolation between boundary conditions** — constructs state trajectories by linearly interpolating between initial and terminal states. This initialisation satisfies boundary conditions by construction but ignores system dynamics, typically producing infeasible trajectories requiring significant correction during optimisation. Linear interpolation may suffice for nearly linear systems or small manoeuvres where dynamics approximate straight-line motion in state space, but proves inadequate for highly nonlinear trajectories.
- **Zero control initialisation** — sets all control values to zero for all discretisation points. This simple approach proves inadequate for control-driven systems where zero control produces trivial or infeasible trajectories. Zero control initialisation may fail entirely for unstable dynamics requiring active control to maintain bounded trajectories.

- **Heuristic trajectory generation** — employs physics-based approximations tailored to problem structure. For spacecraft attitude control, eigenaxis rotation provides a physically motivated initialisation. This strategy is famous for trapping solvers in non-optimal solution basins, as these trajectories comply with both system dynamics and constraints and, therefore, often lie in a local minimum.

Deterministic initialisation offers computational economy, deterministic reproducibility, and simple implementation. However, reliability degrades for problems with significant nonlinearity, large manoeuvre magnitudes, or complex constraint activity [35]. Deterministic methods prove most appropriate for well-behaved problems and small perturbations from known solutions.

Stochastic Initialisation

Stochastic strategies combine derivative-free global search with gradient-based refinement, exploring multiple candidate solutions to identify promising initialisation points. Metaheuristic algorithms such as PSO have demonstrated effectiveness for trajectory optimisation initialisation [35, 34, 24].

The two-stage approach performs global search using metaheuristics (see section 2.6.3) to generate candidate solutions, evaluates a population of trajectories across the decision variable space, selects the best candidate based on objective value and constraint satisfaction, and refines the selected solution using gradient-based NLP optimisation. Stochastic initialisation provides several advantages over deterministic approaches. Exploring multiple solution candidates reduces sensitivity to the quality of the initial guess. Global search capability enables escape from poor local minima that trap deterministic methods. Discovery of solution structure, such as switching patterns in bang-bang control, provides physically meaningful initialisation for refinement. The parallel nature of population-based algorithms enables efficient implementation on multi-core processors or GPUs [37, 38]. However, stochastic methods impose computational expense, typically requiring thousands of function evaluations before gradient-based refinement. The stochastic nature introduces solution variability between runs with different random seeds. Metaheuristic performance depends on parameter tuning, requiring problem-specific calibration. Unlike gradient-based methods, metaheuristics provide no theoretical convergence guarantees or optimality conditions.

Selection Criteria

initialisation strategy selection depends on problem characteristics and computational constraints. Problem complexity assessment guides the choice: well-behaved dynamics with smooth objective functions permit deterministic methods, while multimodal landscapes with multiple local minima require stochastic global search. An unknown solution structure, particularly switching patterns in bang-bang control, favours hybrid approaches that combine stochastic structure discovery with gradient-based refinement.

Computational budget availability influences strategy selection. Tight time constraints in online optimisation necessitate simple deterministic initialisation, accepting reduced reliability for computational speed. Offline trajectory generation enables sophisticated stochastic methods, which invest computation to achieve high reliability. The availability of prior solutions enables warm-starting when problem parameters vary continuously, eliminating the need for expensive global search.

The required reliability level determines method sophistication. Applications that demand high success rates justify the use of stochastic or hybrid methods, despite the associated computational expense. Systems that tolerate occasional failures may employ simpler deterministic methods and attempt alternative initialisations upon convergence failure.

2.7.2 GPU Acceleration Techniques

GPUs have evolved from specialised graphics hardware to general-purpose parallel computing platforms. The CUDA (Compute Unified Device Architecture) programming model developed by

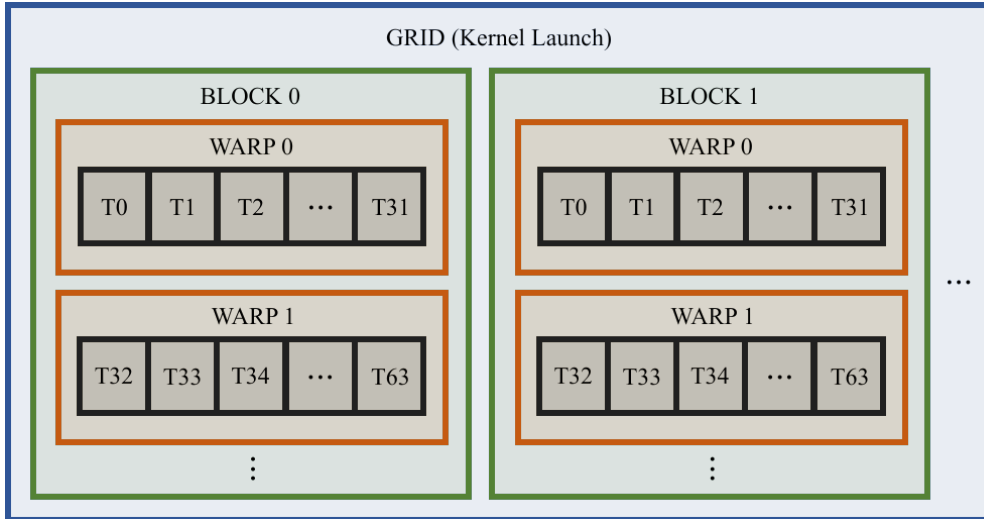


Figure 2.1 CUDA hierarchical thread organisation.

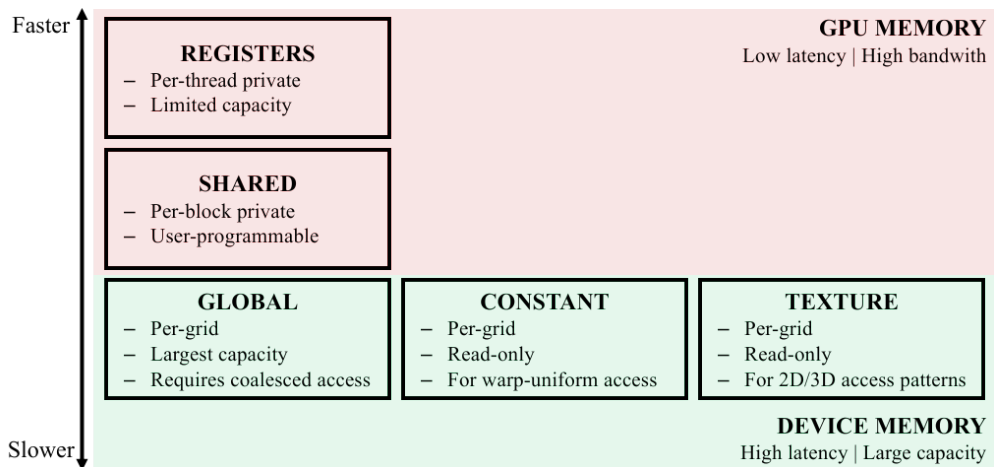


Figure 2.2 CUDA memory hierarchy from fastest to slowest.

NVIDIA provides C/C++ language extensions enabling exploitation of GPU parallelism for scientific computing [39]. Trajectory optimisation exhibits a parallelisable structure amenable to GPU acceleration, though sequential components within NLP solvers limit overall speedup.

CUDA Architecture and Programming Model

CUDA exposes a hierarchical thread organisation comprising: threads (finest granularity execution units), blocks (thread groups executing on streaming multiprocessors (SM)), and grids (block collections comprising a kernel launch). Figure 2.1 illustrates this hierarchy, where each block contains multiple groups of 32 threads that execute instructions in lockstep (single instruction, multiple thread (SIMT) execution model) known as warps. This organisational structure enables massive parallelism while maintaining simplicity in the programming model.

The memory hierarchy, depicted in figure 2.2, comprises multiple levels with distinct latency and capacity characteristics. Registers provide the fastest per-thread private storage with limited capacity. Shared memory offers fast per-block storage under explicit programmer control, functioning as a software-managed cache. Global memory, residing in device dynamic random access memory (DRAM), provides the largest capacity with the highest latency and requires coalesced access patterns for efficient bandwidth utilisation. Constant and texture memory represent specialised cached device memory, optimised for warp-uniform reads and spatial locality, respectively [40].

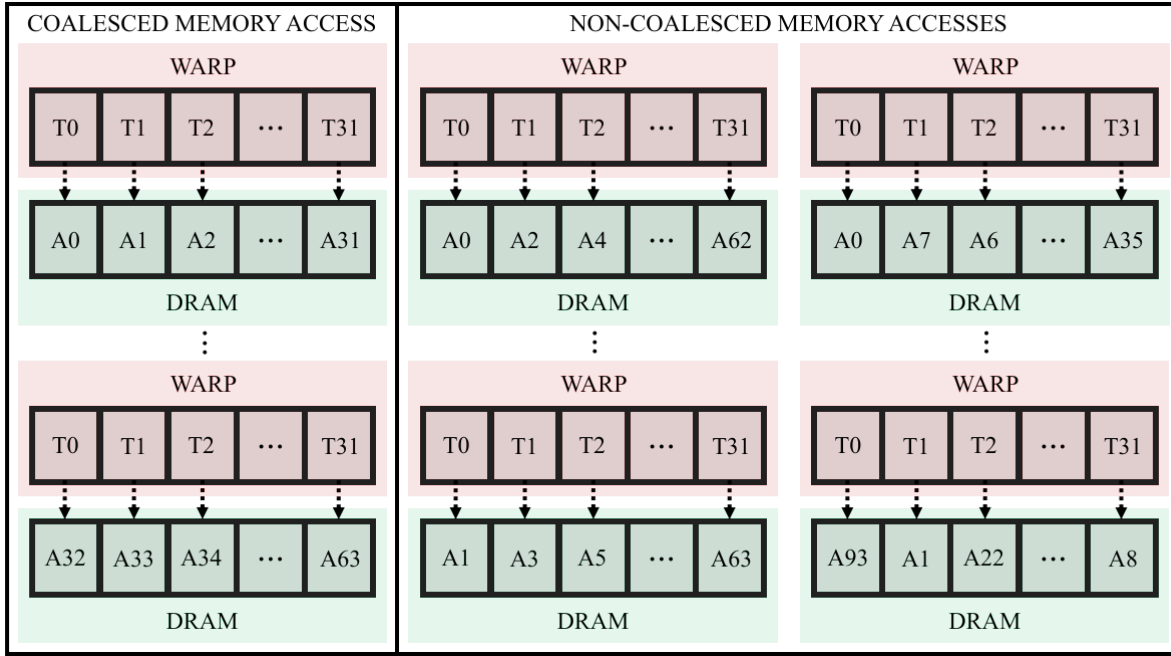


Figure 2.3 Coalesced memory access vs non-coalesced memory accesses.

Performance optimisation requires the exploitation of architectural characteristics. Memory coalescing through aligned, contiguous access patterns maximises global memory bandwidth utilisation. Figure 2.3 shows what this looks like. Shared memory exploitation reduces device memory traffic by enabling data reuse within thread blocks, thereby improving overall system performance. Occupancy maximisation hides memory latency through computation-memory access overlap. Thread divergence minimisation maintains uniform control flow within warps, preventing serialisation of divergent execution paths [40].

Well-designed computational kernels demonstrate 10–100 \times speedup versus sequential CPU execution [39]. However, achievable performance gains depend critically on algorithmic parallelisability, memory access patterns, and computational intensity characteristics of the specific problem domain.

GPU Acceleration in Trajectory Optimisation

Direct transcription generates a parallel structure suitable for GPU implementation. Multiple shooting with N segments enables concurrent dynamics propagation: each segment integration proceeds independently, requiring only segment-local data. Collocation methods parallelise constraint evaluation at hundreds of discretisation points. Sensitivity computation for gradients and Hessians via automatic differentiation benefits from parallel evaluation of partial derivatives.

Implementation examples demonstrate the potential and limitations of GPU acceleration. CuSADI provides CUDA-based symbolic automatic differentiation, generating GPU kernels for function and gradient evaluation [41]. CVODES-CUDA implements GPU-accelerated ODE integration with sensitivity analysis [20]. GPU-based interior-point methods for linear problems accelerate function evaluation but face challenges in sparse linear algebra [42].

Although function evaluation speedup has been demonstrated for dynamics propagation and constraint evaluation, overall optimisation speedup remains limited by sequential components.

Limitations and Challenges

NLP solvers contain inherently sequential components resistant to parallelisation. Line search algorithms backtrack sequentially, evaluating merit functions until sufficient decrease conditions are satisfied. Convergence checks require global synchronisation to assess optimality conditions across

all variables. KKT matrix factorisation for computing Newton steps exhibits limited parallelism, as sparse direct solvers perform elimination with irregular dependency patterns that are poorly suited to GPU architectures.

Solving linear systems presents particular challenges on GPUs. Sparse factorisation involves irregular memory access patterns (indirect addressing through pointer-based data structures) and low arithmetic intensity (computation per memory access), characteristics that mismatch the GPU memory hierarchy, which is optimised for regular, compute-intensive operations. Memory bandwidth requirements can exceed available Peripheral Component Interconnect Express (PCIe) bandwidth for high-speed data transfers between CPU and GPU, with transfer latency negating computational gains for small to moderate problem sizes.

Programming complexity increases substantially for GPU implementation. Code must explicitly manage memory allocation, data transfer, kernel launch parameters, and synchronisation. Debugging parallel code proves significantly more challenging than sequential programs, as race conditions and memory access violations manifest non-deterministically.

Hybrid CPU-GPU Architectures

Viable solutions employ hybrid architectures that exploit the complementary strengths of CPU and GPU hardware. The CPU manages the optimisation loop, performs sequential operations (line search, convergence checks), handles control-flow-intensive tasks, and executes sparse linear algebra when appropriate. The GPU performs expensive parallel function evaluations, evaluates constraints across the discretisation grid, computes gradients via parallel automatic differentiation, and performs batched dynamics integration.

This division of labour can achieve superior single-thread performance and control flow handling on the CPU, while leveraging massive GPU throughput for arithmetic operations. Asynchronous computation enables overlap: while the GPU evaluates functions, the CPU can prepare the next iteration or process results from previous evaluations.

Well-designed hybrid systems achieve $2\text{-}10\times$ speedup over CPU-only implementations [42]. The modest speedup relative to theoretical GPU peak performance reflects Amdahl's law, which states that sequential components limit overall acceleration, regardless of the speedup achieved in parallel sections.

2.7.3 Reliability Assessment

Algorithm reliability is the probability of successful convergence to feasible, globally optimal solutions, and requires statistical characterisation across problem parameter spaces. Nonconvex optimisation landscapes with multiple local minima exhibit initialisation-dependent convergence behaviour that defeats deterministic analysis. Gradient-based solvers demonstrate varying success rates depending on problem formulation, manoeuvre type, and initialisation strategy [35]. Statistical validation through repeated trials with parameter variation quantifies operational envelope boundaries and identifies problem regions requiring enhanced initialisation or alternative solution methods.

Practical sample size selection balances theoretical requirements with computational constraints. For a D -dimensional parameter space with l samples, the informal rule $l \approx 10D$ has been empirically validated and theoretically justified by Loeppky et al. [43] as a good starting point, though convergence studies remain advisable to verify sufficiency for specific applications.

Monte Carlo Simulation

MC simulation utilises stochastic sampling to assess algorithm performance across various parameter distributions. The methodology defines problem parameter space, specifies probability distributions for each parameter (uniform, normal, or problem-specific distributions), and performs independent

random draws for each trial. Each trial solves the trajectory optimisation problem from specified initialisation, recording convergence success, final objective value, and computation time. Aggregating results across l trials estimates convergence probability, characterises solution quality distribution, and identifies parameter regions with poor reliability.

MC simulation provides conceptual simplicity, general applicability across diverse problems, and well-established statistical theory for confidence interval estimation. However, the convergence rate scales as $O(l^{-1/2})$: halving the confidence interval width requires quadrupling the sample size. Achieving tight confidence bounds on rare events (failure probabilities below 1%) necessitates tens of thousands of trials.

Latin Hypercube Sampling

Latin Hypercube Sampling (LHS) provides stratified sampling with improved space-filling properties compared to pure random sampling [44]. The method offers better parameter space coverage with fewer samples, reducing computational burden for expensive trajectory optimisation evaluations.

For a D -dimensional parameter space with l samples, LHS proceeds as follows. First, divide each parameter range into l equal-probability intervals. Second, sample once from each interval for every parameter dimension independently. Third, randomly permute samples across dimensions to create D -dimensional combinations. This ensures each interval is represented exactly once per dimension, avoiding clustering that afflicts pure random sampling.

Stein [45] established the theoretical foundation for LHS variance reduction, proving that the estimator variance converges as $O(l^{-1})$ when $l \gg D$, compared to $O(l^{-1/2})$ for MC simulations. The degree of variance reduction depends fundamentally on the additivity of the objective function: LHS effectively filters out additive components, with remaining variance proportional to the non-additive residual. This theoretical result demonstrates that LHS achieves asymptotically lower variance than simple random sampling for any square-integrable function, with maximum benefit for nearly-additive response surfaces.

LHS achieves reduced clustering and more uniform exploration of parameter extremes compared to traditional MC simulations, with reduced sample count for equivalent statistical confidence. Implementation complexity exceeds that of simple random sampling, and variance reduction effectiveness depends on response surface smoothness and additivity—assumptions that are potentially violated by discontinuous failure boundaries in some optimisation problems.

Reliability Metrics and Analysis

Reliability assessment quantifies algorithm performance through multiple metrics beyond binary success/failure classification. The convergence rate measures the fraction of trials that achieve feasible solutions satisfying optimality tolerances. Solution quality distribution characterises objective value variation across successful trials, identifying cases where poor initialisation yields suboptimal local minima. Computation time distributions inform real-time feasibility assessment. Parameter sensitivity analysis identifies configurations that exhibit degraded reliability, guiding the development of specialised initialisation strategies for challenging regions.

Statistical analysis of reliability data enables the characterisation of operational envelopes. Confidence intervals on convergence probability provide probabilistic guarantees for deployment. Identification of parameter boundaries where reliability degrades rapidly guides operational constraints, such as restricting manoeuvre angles, limiting initial angular velocities, or constraining spacecraft asymmetry ratios to regions with high success rates. Reliability assessment validates algorithm improvements: comparing convergence rates before and after initialisation enhancement quantifies the benefit with statistical rigour.

3 Methodology

This chapter outlines the methodology for developing and verifying real-time spacecraft attitude control algorithms, with a goal of achieving computation times of less than 200 milliseconds. Building upon the theoretical foundations of chapter 2, the approach follows a hierarchical framework: foundational design choices establish the problem structure; sequential algorithmic optimisation identifies optimal configurations through comparative evaluation; and MC simulation quantifies reliability across the operational envelope.

Section 3.1 documents the selection of quaternion parameterisation, direct dynamics formulation, and the CasADi-based computational framework. Section 3.2 compares transcription methods, integration schemes, and NLP solvers through benchmark problems. Section 3.3 defines test problem suites, performance metrics, and statistical verification protocols. Section 3.4 develops PSO-based initialisation strategies to enhance convergence reliability. Section 3.5 specifies the computational platform characteristics and numerical parameters that enable reproducibility. Each decision is justified through a quantitative performance evaluation, ensuring that the final algorithm strikes a balance between computational efficiency, solution quality, and convergence reliability.

3.1 Foundational Design Choices

This section establishes fundamental design decisions that define the problem structure prior to algorithmic optimisation. These choices constrain subsequent algorithmic decisions and directly influence solution feasibility, computational efficiency, and implementation complexity.

1. **Attitude Parameterisation** – Quaternion parameterisation is selected based on three advantages established in section 2.1.2 and table 2.1: global validity without singularities, minimal redundancy (single constraint versus six for $\text{SO}(3)$), and linear kinematic equations (2.8) which facilitate efficient gradient computation.
2. **Dynamics Formulation** – Direct dynamics formulation is selected because it provides natural handling of control constraints (2.47) as box constraints in the NLP, and simplified boundary condition enforcement. The inverse dynamics alternative offers automatic boundary condition satisfaction but introduces control feasibility challenges for time-optimal control where the bang-bang structure (2.62) drives controls to saturation, and additional complexity in enforcing the unit quaternion norm constraint and finding adequate basis functions.
3. **Control Parameterisation** – Full trajectory optimisation is selected based on the following criteria: switching structures for track-to-track manoeuvres and asymmetric spacecraft remain problem-dependent despite analytical results for symmetric rest-to-rest cases; and the formulation accommodates arbitrary configurations within a unified framework. Although the decision variable count exceeds that for bang-bang parameterisation, the enhanced convergence robustness due to the absence of discontinuities normally offsets this cost.
4. **Optimisation Methodology** – Direct transcription is selected over indirect methods (section 2.3.1) due to its larger convergence basins enabling cruder initial guesses, intuitive initialisation using physical variables rather than abstract costates, natural constraint handling, robustness to parameter variations, mature solver infrastructure, and optimal computational efficiency.

5. **Computational Framework** – CasADi provides exact derivatives via automatic differentiation, eliminating finite-difference errors, automatic sparsity exploitation for block-tridiagonal structures (2.28), unified APIs for multiple NLP solvers enabling their comparison, high-level Opti syntax, and extensive aerospace validation.
6. **NLP Solver** – IPOPT is selected for initial algorithm development due to its general-purpose applicability across all transcription methods, enabling their comparison and robust filter line search convergence across parameter space. However, section 3.2.3 evaluates structure-exploiting alternatives.
7. **Verification and Benchmarking** – CGPOPS provides reference solutions via hp-adaptive LGR collocation achieving spectral convergence. Established aerospace benchmarking enables verification through literature comparison. Computation times (ranging from seconds to minutes) preclude real-time use. Therefore, CGPOPS serves exclusively for verification. Results in chapter 4 are verified against CGPOPS to ensure speed optimisations preserve solution quality.

3.2 Algorithmic Optimisation

This section documents the systematic selection of algorithmic components through comparative evaluation on benchmark problems. The methodology employs sequential decision-making to identify the configuration achieving an optimal balance between computational efficiency and solution quality. Benchmark scenarios consist of symmetric spacecraft executing rest-to-rest manoeuvres through 45° , 90° , and 180° rotations, for which analytical switching structures and optimal manoeuvre durations have been established [3, 4]. Table 3.2 presents the dimensionless optimal durations for these canonical cases, which serve as reference solutions for verifying implementation correctness and measuring solution quality through the computation of optimality gaps. The bounds are chosen to be large enough not to interfere with the optimal solution, but as tight as possible to restrict the solution search space and accelerate convergence.

Table 3.1 Dimensionless parameters for spacecraft attitude control optimisation.

| Category | Parameter | Symbol | Value |
|--|---------------------|-----------------------|-------|
| Manoeuvre Duration | Minimum bound | T_{\min} | 0.0 |
| | Maximum bound | T_{\max} | 6.0 |
| Symmetric Spacecraft Principal Moments of Inertia | i -axis component | \bar{J}_i | 1.0 |
| Angular Velocity Bounds | Maximum magnitude | ω_{\max} | 5.0 |
| | Minimum magnitude | ω_{\min} | -5.0 |
| Control Torque Bounds | Maximum magnitude | $\bar{\tau}_{i,\max}$ | 1.0 |
| | Minimum magnitude | $\bar{\tau}_{i,\min}$ | -1.0 |

Note: All parameters are dimensionless. The overbar notation denotes normalisation by the characteristic scales J_0 (reference inertia) and τ_{\max} (maximum control authority). Quaternion components are inherently bounded by ± 1 due to the unit norm constraint. Dimensionless time may be converted to dimensional time in seconds by multiplying by the scaling factor $\sqrt{J_0/\tau_{\max}}$. Dimensionless angular velocity must be divided by the same scaling factor to convert it into its dimensional counterpart in rad/s.

The selection process follows an iterative refinement strategy wherein earlier decisions constrain and inform subsequent choices. Transcription method selection (section 3.2.1) establishes the fundamental discretisation framework, determining whether dynamics are enforced through shooting integration or collocation constraints. The integration scheme evaluation (section 3.2.2) then optimises the dynamics propagation method within the selected transcription framework, comparing

fixed-step explicit methods with adaptive implicit schemes and evaluating the potential for GPU acceleration. Finally, NLP solver optimisation (section 3.2.3) identifies the most efficient solver for the established problem structure, comparing general-purpose interior-point methods against structure-exploiting Riccati-based algorithms.

Each comparison employs consistent evaluation metrics: total computation time and solution quality quantified by the optimality gap relative to the analytical solutions in table 3.2.

Table 3.2 Analytical solutions for minimum-time rest-to-rest manoeuvres of symmetric spacecraft.

| Rotation Angle | Dimensionless Duration | Number of Switches |
|----------------|------------------------|--------------------|
| 45° | 1.7471 (1.7499) | 6 (7) |
| 90° | 2.4211 | 5 |
| 180° | 3.2431 | 5 |

3.2.1 Transcription Method Selection

The first step is comparing direct multiple shooting (section 2.3.2) with Hermite-Simpson collocation (section 2.3.2). They represent alternative frameworks for enforcing dynamics constraints in direct transcription. Multiple shooting generates block-tridiagonal constraint structures exploitable by specialised solvers and enables parallel integration across shooting intervals. Hermite-Simpson collocation requires fewer function evaluations through an implicit midpoint formulation. Both achieve fourth-order accuracy $O(\Delta t^4)$: Hermite-Simpson through cubic polynomial approximation, multiple shooting when paired with RK4 integration (section 2.3.2). While Hermite-Simpson's implicit properties benefit stiff systems, spacecraft attitude dynamics with moderate inertia asymmetry exhibit negligible stiffness. The minimum number of discretisation intervals required for reliable convergence for both methods is $N = 50$, and this value is maintained throughout the remainder of the optimisation.

The comparison determines that multiple shooting gives better results, leading to its adoption for all future development. These results are analysed in section 4.1.1.

3.2.2 GPU-Accelerated Dynamics Propagation

Within the multiple shooting framework, the choice of integration scheme for propagating dynamics across shooting intervals is analysed. This evaluation compares explicit fixed-step integration using classical RK4 against adaptive implicit methods implemented in CVODES, the variable-step ordinary differential equation solver from the SUNDIALS library. GPU acceleration is used to exploit the parallel structure of multiple shooting.

- **RK4** provides deterministic computational cost with four function evaluations per integration step (2.30), enabling straightforward performance prediction and memory allocation. The explicit nature requires no iterative solution of implicit equations, simplifying implementation and facilitating GPU parallelisation. However, fixed step sizes may prove inefficient for trajectories with varying solution smoothness, potentially requiring very small steps across the entire interval to maintain accuracy near switching discontinuities.
- **CVODES** employs variable-order, variable-step Adams-Moulton and Backward Differentiation Formula methods with automatic stiffness detection. The adaptive step size feature provides computational efficiency for smooth trajectory segments while concentrating steps near rapid state variations. CVODES includes built-in GPU-enabled integration and sensitivity analysis capabilities that accelerate computation, potentially offsetting the overhead of adaptive step size and implicit integration.

3 Methodology

The evaluation compares computational platforms and integration methods simultaneously. It examines the potential for GPU acceleration in explicit RK4 integration and a GPU CVODES implementation by comparing their performance with that of a CPU-run explicit RK4 integration scheme. The analysis considers total computation time, including CPU-to-GPU memory transfers and kernel launch latency, as these overheads can dominate for small problems where integration time itself is negligible.

To enable initial GPU kernel implementation without requiring manual construction of exact analytical derivatives, the NLP solver employs finite-difference approximations for Jacobian evaluation and limited-memory approximations for Hessian construction. These approximations, specified through solver options, reduce implementation complexity at the expense of computational efficiency and solution accuracy when compared to exact derivative formulations. These settings are also used in the CPU implementation for fair comparison.

The analysis of the comparison results revealed that propagating the dynamics on the CPU using explicit RK4 entails the best performance/complexity ratio and is therefore selected as the numerical integration method for the final algorithm configuration. Section 4.1.2 contains the details of this analysis.

3.2.3 NLP Solver Optimisation

The NLP solver selection fundamentally determines whether real-time computation times can be achieved. Here, IPOPT is compared to FATROP, which directly exploits the block-tridiagonal structure of OCPs transcribed using multiple shooting, reducing computational complexity from cubic to linear in horizon length.

The comparison employs multiple shooting with CPU-based RK4 integration. Both solvers receive identical problem formulations generated through CasADI's symbolic framework, ensuring consistency in derivative computations and constraint structures. The results presented in section 4.1.3 show that FATROP consistently outperforms IPOPT, leading to its adoption in the optimal algorithm configuration.

3.3 Algorithm Reliability Assessment

The reliability evaluation of trajectory optimisation algorithms requires comprehensive testing across representative problem scenarios and a statistical assessment of performance characteristics. This section establishes the verification framework employed to characterise implementation performance across the operational envelope. The methodology integrates stratified sampling techniques for efficient exploration of the parameter space with MC analysis for statistical reliability assessment.

3.3.1 Test Problem Suite Definition

The benchmark problem suite spans the operational envelope through variation of spacecraft configuration and manoeuvre characteristics. The problem difficulty increases with every configuration, enabling the assessment of algorithm robustness across configurations ranging from analytically tractable cases to computationally challenging scenarios.

Problem Configurations and Manoeuvre Types

Three evaluation scenarios are considered, progressing from a simpler case to increasingly complex operational conditions:

1. **Scenario A: Rest-to-rest with symmetric spacecraft** – Inertia tensor $J_1 = J_2 = J_3 = 1.0$ (dimensionless) with zero initial and final angular velocities ($\omega_0 = \omega_f = \mathbf{0}$). This configuration decouples Euler's rotational equations (2.5), eliminating gyroscopic coupling terms.

2. **Scenario B: Track-to-track with symmetric spacecraft** – Inertia tensor $J_1 = J_2 = J_3 = 1.0$ (dimensionless) with non-zero initial and/or final angular velocities ($\omega_0, \omega_f \in [\omega_{\min}, \omega_{\max}]$). This scenario evaluates algorithm performance under more complex boundary conditions while maintaining decoupled dynamics.
3. **Scenario C: Track-to-track with asymmetric spacecraft** – Inertia ratio $J_1 : J_2 : J_3 = 1 : 2 : 3$, representative of small satellite configurations with distinct principal axes, with non-zero boundary velocities. This configuration combines gyroscopic coupling with complex boundary conditions, representing the most challenging operational scenario.

Initialisation Approach

A deterministic baseline employs warm-starting from a previously converged optimal trajectory for a rest-to-rest 90° rotation manoeuvre about the second principal axis (y-axis). This reference trajectory comprises complete state and control histories, as well as the time-step size, and serves as the initial guess for all manoeuvre scenarios regardless of boundary condition similarity. This trajectory provides the solver with clues about the bang-bang behaviour of the control parameters and a reasonable guess for manoeuvre duration. Additionally, since it is a real trajectory, all its points lie within the feasible parameter space, thereby avoiding infeasibility problems that can stem from poor initial guesses.

More accurate initialisation techniques are implemented, namely PSO (subsection 2.6.3). Nevertheless, its use comes with an added complexity and computation time. This last aspect can be offset with improved gradient-based solver convergence, but its implementation is delayed until proven necessary.

3.3.2 Monte Carlo Simulation Framework

Statistical verification employs MC simulation with LHS (section 2.7.3) to characterise algorithm performance across the parameter space. This framework strikes a balance between statistical rigour and computational feasibility. Boundary condition parameters are sampled from uniform distributions representing diverse operational scenarios. The sampling ranges are explained below and summarised in table 3.3.

- **Attitude quaternions:** Terminal attitudes are generated through uniform sampling of Euler angles from the interval $[-180^\circ, 180^\circ]$ for each of the three axes. These are subsequently converted into quaternions, ensuring their placement on the unit sphere. While this approach does not produce perfectly uniform coverage of the rotation group $\text{SO}(3)$, as some configurations are redundant, it still provides adequate diversity for MC analysis across the operational envelope. The initial attitude is fixed to $\{0^\circ, 0^\circ, 0^\circ\}$ since any pair of initial and final attitudes can be rotated to this coordinate frame for solving, and then the solution can be adjusted back to the boundary conditions interval (equations (2.51) and (2.52)).
- **Angular velocities:** Initial and terminal angular velocity components are sampled uniformly from $[-3^\circ/\text{s}, 3^\circ/\text{s}]$ per axis, and are normalised afterward so that $\|\omega\| \leq 3^\circ/\text{s}$. This range encompasses typical spacecraft slew rates while remaining within the typical capabilities of star-sensor measurements [46].

3.3.3 Performance Metrics and Evaluation Criteria

Algorithm assessment employs quantitative metrics aligned with the research objectives established in chapter 1. Metrics span computational efficiency, solution quality, and convergence reliability dimensions.

Table 3.3 Monte Carlo simulation parameter ranges for boundary condition sampling.

| Category | Parameter | Range |
|---------------------------|------------------------------|---|
| Initial Attitude | Euler angles (3 components) | $\mathbf{0}^\circ$ (fixed) |
| | Converted to quaternion | Identity quaternion {1, 0, 0, 0} |
| Terminal Attitude | Euler angles (3 components) | $[-180^\circ, 180^\circ]$ each |
| | Converted to quaternion | Unit sphere |
| Initial Angular Velocity | Rest-to-rest | $\mathbf{0}^\circ/\text{s}$ (fixed) |
| | Per-axis components (3 axes) | $[-3^\circ/\text{s}, 3^\circ/\text{s}]$ each* |
| Terminal Angular Velocity | Rest-to-rest | $\mathbf{0}^\circ/\text{s}$ (fixed) |
| | Track-to-track (3 axes) | $[-3^\circ/\text{s}, 3^\circ/\text{s}]$ each* |

*Values are normalised afterward so that $\|\omega\| \leq 3^\circ/\text{s}$.

Computational Efficiency Metrics

Total computation time $\mathcal{T}_{\text{total}}$ decomposes into initialisation and solver contributions:

$$\mathcal{T}_{\text{total}} = \mathcal{T}_{\text{init}} + \mathcal{T}_{\text{solver}} \quad (3.1)$$

where $\mathcal{T}_{\text{init}} = 0$ for the fixed deterministic initialisation. The real-time threshold established in chapter 1 requires $\mathcal{T}_{\text{total}} < 200\text{ ms}$ for onboard trajectory generation.

Solution Quality Metrics

Optimality gap quantifies solution quality relative to reference trajectories:

$$\Delta_{\text{opt}} = \frac{|T_{\text{computed}} - T_{\text{ref}}|}{T_{\text{ref}}} \times 100\% \quad (3.2)$$

where T_{computed} denotes the manoeuvre duration obtained by the evaluated algorithm and T_{ref} represents the reference optimal duration from either analytical solutions (table 3.2) or CGPOPS. Acceptable solution quality requires $\Delta_{\text{opt}} < 0.1\%$, striking a balance between near-optimality and computational efficiency.

Convergence Reliability Metrics

Convergence rate $\mathcal{R}_{\text{conv}}$ measures the fraction of trials achieving feasible, optimal solutions:

$$\mathcal{R}_{\text{conv}} = \frac{N_{\text{success}}}{N_{\text{total}}} \times 100\% \quad (3.3)$$

where N_{success} denotes trials satisfying convergence criteria and N_{total} represents total trial count. Convergence criteria require: satisfaction of NLP optimality and constraint violations tolerances, and optimality gap $\Delta_{\text{opt}} < 0.1\%$ when reference solutions are available. High-reliability operation demands $\mathcal{R}_{\text{conv}} > 99\%$.

Table 3.4 summarises acceptance criteria for algorithm verification.

3.4 PSO Initialisation Strategy Development and Evaluation

Nonconvex trajectory optimisation exhibits convergence behaviour that is critically dependent on the quality of initialisation, with poor initial guesses yielding convergence failure, constraint violations, or entrapment in suboptimal local minima (section 2.7.1). This section develops initialisation strategies following the two-stage paradigm established in section 2.6.3: derivative-free global search

Table 3.4 Performance metric definitions and acceptance criteria for algorithm verification.

| Category | Metric | Symbol | Acceptance Criterion |
|--------------------------|------------------------|-----------------------------|----------------------|
| Computational Efficiency | Total computation time | T_{total} | < 200 ms |
| Solution Quality | Optimality gap | Δ_{opt} | < 0.1% |
| Convergence Reliability | Convergence rate | $\mathcal{R}_{\text{conv}}$ | > 99% |

via PSO followed by gradient-based refinement using FATROP with multiple shooting and CPU-based RK4 integration. The evaluation compares two control parameterisation approaches: full trajectory optimisation versus STO, and benchmarks stochastic initialisation against the previously characterised deterministic initialisation method.

3.4.1 Control Parameterisation Approaches

Two fundamentally different parameterisation strategies are evaluated for PSO-based initialisation, each representing distinct trade-offs between search space dimensionality and structural assumptions about optimal control form. All PSO implementations leverage GPU parallelisation for concurrent particle evaluation, exploiting the embarrassingly parallel structure of population-based metaheuristics (section 2.7.2).

Full Control Trajectory Parameterisation

Full control trajectory parameterisation treats control values at all 50 discretisation points as independent PSO decision variables, imposing no *a priori* structural constraints. It then uses the generated control trajectory to propagate the dynamics from the initial state, and enforces the final state constraint through a penalty on the objective function. The decision variable vector comprises the control torques $\tau_{i,k}$ for each of the 50 discretisation intervals k and for each of the 3 control axes i , and the time-step Δt , yielding dimensionality $O(50 \times 3 + 1) = O(151)$. This high-dimensional search space provides complete flexibility for discovering arbitrary control structures, but it also increases the computational burden and may impede convergence for metaheuristic algorithms.

Dynamic weight strategies are applied to all three weights in equation (2.63) to balance exploration in early iterations with exploitation during convergence, by linearly decreasing the parameters from their initial to minimum values over the optimisation horizon. Therefore, the PSO parameters subject to tuning comprise: inertia weight w_0 , cognitive parameter w_1 , social parameter w_2 , population size \mathcal{N} , iteration count \mathcal{K} , and dynamic weight bounds $w_{0,\min}, w_{1,\min}, w_{2,\min}$ for time-varying parameters. The methodology used to select them is described in section 3.4.2.

STO Parameterisation

STO exploits the bang-bang control structure established in section 2.2.3 and equations (2.27) and (2.62) by parameterising trajectories through switching times y_i and initial control directions s_i for each of the 3 axis i . From the available analytical solutions, the maximum number of control switches per axis $y_{i,\max}$ is 3 [3]. However, the total maximum number of control switches y_{\max} for all 3 axes in an optimal trajectory is 6 (table 3.2). The dimensionality of the problem is then reduced to $O(3 + 6 + 1) = O(10)$, substantially decreasing search space volume when compared to the $O(151)$ dimensionality of the previous method and improving metaheuristic convergence characteristics discussed in section 2.4.

Binary PSO addresses the discrete control direction variables through sigmoid transfer functions (equation (2.64)), introducing additional tuning parameters beyond those in full parameterisation: sigmoid scaling parameter α controlling transition steepness and velocity saturation threshold $\epsilon \in [0.5, 1.0]$ maintaining stochastic behaviour (equation (2.65)). The continuous switching time vari-

3 Methodology

ables employ standard PSO updates with temporal ordering constraints $t_0 < t_i^{(1)} < \dots < t_i^{(y)} < t_f$ enforced by reordering the values at each iteration.

3.4.2 Parameter Tuning and Optimisation

PSO performance depends critically on parameter selection (section 2.6.3). Systematic tuning via LHS identifies configurations balancing convergence reliability with computational efficiency. The tuning methodology evaluates PSO performance when coupled with gradient-based refinement, reflecting the two-stage approach established in section 3.4.

Tuning Methodology

Parameter tuning employs nested optimisation: an outer LHS loop samples PSO parameter combinations while an inner evaluation assesses performance on a representative combination of rest-to-rest manoeuvres. The methodology proceeds as follows:

1. Generate 1000 PSO parameter combinations via LHS across specified parameter ranges (table 3.5).
2. For each parameter combination, execute 1000 independent trials with LHS-sampled initial and final boundary conditions.
3. Record convergence rate $\mathcal{R}_{\text{conv}}$ and mean computation time $\mathcal{T}_{\text{total}}$ for each parameter combination.
4. Identify configurations that minimise computation time and maximise convergence rate.

Parameter Space

For full trajectory parameterisation (section 3.4.1), the parameter space comprises:

- **Population size and iteration count** (\mathcal{N}, \mathcal{K}): These two parameters together determine the problem size, as they control how long the PSO needs to run. For each control parameterisation approach, pairs of \mathcal{N} and \mathcal{K} are tested until a computation time of 100 ms or more is achieved. This limit is selected to allocate sufficient computational budget for subsequent gradient-based refinement within the 200-ms real-time constraint. For \mathcal{N} , only multiples of 640 (the number of cores available in GPU) are used in order to maximise GPU utilisation. The resulting sampling ranges are: $\mathcal{N} \in \{640, 1280, 1920, 2560, 3200, 3840, 4480, 5120\}$ and $\mathcal{K} \in [10, 750]$.
- **Exploration parameters** (w_0, w_1, w_2): Initial values for inertia weight, cognitive parameter, and social parameter are sampled from $[0.1, 10.0]$. While typical PSO implementations employ values in the range $[0.5, 3.0]$, the extended upper bound enables exploration of aggressive parameter settings potentially beneficial for high-dimensional trajectory optimisation problems: $w_0, w_1, w_2 \in [0.1, 10.0]$.
- **Minimum exploration parameters** ($w_{0,\min}, w_{1,\min}, w_{2,\min}$): Terminal values for dynamic weight scheduling are sampled as fractions of their corresponding initial values to ensure monotonic decrease throughout optimisation. Sampling $\zeta_0, \zeta_1, \zeta_2 \in [0.0, 1.0]$ yields minimum parameters $w_{0,\min} = \zeta_0 \cdot w_0$, $w_{1,\min} = \zeta_1 \cdot w_1$, $w_{2,\min} = \zeta_2 \cdot w_2$, satisfying the constraint $w_{0,\min} \leq w_0$, $w_{1,\min} \leq w_1$, $w_{2,\min} \leq w_2$ by construction.

For STO parameterisation employing binary PSO (section 3.4.1), additional parameters include:

- **Sigmoid scaling (α):** The scaling parameter controlling sigmoid function steepness in the binary position update (equation (2.64)) is sampled from the same extended range as continuous parameters to enable exploration of both gradual and sharp probabilistic transitions: $\alpha \in [0.1, 10.0]$.
- **Sigmoid saturation threshold (ϵ):** The saturation threshold determining maximum sigmoid output bounds (equation (2.65)) is sampled from $[0.5, 1.0]$, where $\epsilon = 0.5$ enforces complete randomisation and $\epsilon = 1.0$ permits deterministic position updates for large velocity magnitudes, as established in section 2.6.3.

Table 3.5 summarises parameter ranges.

Table 3.5 PSO parameter ranges for LHS-based tuning.

| Category | Parameter | Range |
|-----------------------|--------------------|------------------|
| Swarm Configuration | Population size | $[640, 5120]^*$ |
| | Iteration count | $[10, 750]$ |
| Inertia Weight | Initial weight | $[0.1, 10.0]$ |
| | Minimum weight | $[0.0\%, 1.0\%]$ |
| Cognitive Parameter | Initial weight | $[0.1, 10.0]$ |
| | Minimum weight | $[0.0\%, 1.0\%]$ |
| Social Parameter | Initial weight | $[0.1, 10.0]$ |
| | Minimum weight | $[0.0\%, 1.0\%]$ |
| Binary PSO (STO only) | Sigmoid scaling | $[0.1, 10.0]$ |
| | Sigmoid saturation | $[0.5, 1.0]$ |

*Values are sampled in multiples of 640 (number of available GPU cores).
Actual allowed values: {640, 1280, 1920, 2560, 3200, 3840, 4480, 5120}

3.4.3 Performance Evaluation

Once both PSO approaches are correctly tuned, their performance is compared to that of the same gradient-based algorithm using a previously converged optimal trajectory as the initial guess. The methodology described in section 3.4 is followed again, and the same metrics are used to evaluate the performance of the new algorithms. The computational efficiency metric (equation (3.1)) now has a non-zero initialisation component T_{init} corresponding to the time spent on the PSO.

The results of this analysis determine the most reliable algorithm configuration developed throughout this work and are presented in section 4.4.

3.5 Implementation Details

This section documents the computational platform, software architecture, and parameter values employed in the present study. A complete specification of the implementation environment enables the reproducibility of results and facilitates a comparative evaluation against alternative approaches. The computational infrastructure comprises consumer-grade hardware, demonstrating the feasibility of real-time trajectory optimisation without requiring specialised aerospace computing resources.

3.5.1 Computational Platform Specifications

All computational experiments were executed on a machine equipped with an Intel Core i7-8750H processor and NVIDIA GeForce GTX 1050 Mobile graphics accelerator. This hardware configuration represents a mid-range computational platform from 2018.

Hardware Configuration

The computational platform comprises two primary processing units whose specifications are detailed in table 3.6.

Table 3.6 Computational platform hardware specifications.

| Component | Specification | Value |
|-----------|--------------------|--------------------------------|
| CPU | Model | Intel Core i7-8750H |
| | Architecture | Coffee Lake (14 nm) |
| | Physical cores | 6 |
| | Logical threads | 12 |
| | Base frequency | 2.20 GHz |
| | Maximum frequency | 4.10 GHz |
| | L3 cache | 9 MB |
| | TDP | 45 W |
| GPU | Model | NVIDIA GeForce GTX 1050 Mobile |
| | Architecture | Pascal (GP107M) |
| | CUDA cores | 640 |
| | SM count | 5 |
| | Base clock | 1354 MHz |
| | Boost clock | 1493 MHz |
| | Memory capacity | 4 GB GDDR5 |
| | Memory bandwidth | 112 GB/s |
| | Compute capability | 6.1 |
| | TDP | 75 W |

Software Environment

The software stack comprises open-source tools and libraries that are selected for their numerical robustness, community support, and cross-platform portability. Table 3.7 enumerates version-specific identifiers enabling exact reproduction of the computational environment.

Table 3.7 Software environment version specifications.

| Category | Component | Version |
|------------------|--------------|-----------|
| Operating System | Ubuntu Linux | 24.04 LTS |
| Compiler | GCC/g++ | 13.3.0 |
| | C++ Standard | C++17 |
| GPU Computing | CUDA Toolkit | 12.8.93 |
| Libraries | CasADi | 3.7.0+ |
| | SUNDIALS | 6.7.0 |
| | IPOPT | 3.14.18 |
| | FATROP | 1.0.0 |
| | CGPOPS | 1.0 |
| Build System | CMake | 3.28.3 |

3.5.2 Problem-Specific Parameter Values

This subsection documents numerical parameter values employed throughout the study, organised by functional category. Unless otherwise stated, parameters remained constant across all computational experiments to ensure consistency in comparative evaluations.

Numerical Precision

Floating-point precision is selected according to computational requirements and hardware characteristics. All CPU-based optimisation computations employ double-precision (64-bit) arithmetic to maintain numerical accuracy throughout the NLP solution process. The PSO initialisation algorithms are implemented using single-precision (32-bit) arithmetic on the GPU, yielding computational performance improvements of approximately $1.5\times$ relative to double-precision implementations. Single-precision arithmetic is not evaluated for GPU dynamics propagation since the resulting numerical accuracy proves insufficient when compared with the accuracy required by the NLP solvers.

NLP Solver Configuration

IPOPT and FATROP are used in their default configuration with CasADi, with the exception of the parameters summarised in table 3.8.

Table 3.8 NLP solver configuration parameters.

| Solver | Parameter | Value | Description |
|--------|-----------------------|-----------|-----------------------------------|
| IPOPT | tol | 10^{-7} | Convergence tolerance |
| | max_iter | 1000 | Maximum iterations |
| | linear_solver | MUMPS | Sparse direct linear solver |
| | mu_strategy | adaptive | Barrier parameter update strategy |
| | warm_start_init_point | yes | Enable warm-start initialisation |
| FATROP | tol | 10^{-7} | Convergence tolerance |
| | max_iter | 1000 | Maximum iterations |
| | linear_solver | BLASFEO | Linear algebra backend |

CGPOPS Verification Parameters

Reference solution generation through CGPOPS employs the mesh refinement and accuracy parameters listed in table 3.9. These settings ensure that the reference solution accuracy exceeds the test algorithm precision, enabling reliable verification. CGPOPS uses the LGR pseudospectral collocation method (section 2.3.2) to transcribe the OCP.

3.6 Chapter Summary

This section summarises the methodology adopted for this thesis, illustrated with diagrams. Diagram 3.1 depicts the foundational work described in section 3.1 that leads to the development of the baseline algorithm. This is then sequentially optimised as shown in diagram 3.2 and described in section 3.2. The optimised algorithm's resilience to changing boundary conditions is tested through an MC simulation (diagram 3.3). This scheme is followed once for rest-to-rest manoeuvres and a second time for track-to-track manoeuvres, both using symmetric spacecraft inertial parameters. The scheme is followed a third and last time for track-to-track manoeuvres, this time using an asymmetric spacecraft. The exact parameters used and boundary conditions bounds can be found

Table 3.9 CGPOPS configuration parameters.

| Parameter | Value | Description |
|---|-----------|---|
| <i>Derivative Computation and Scaling</i> | | |
| derivativeSupplier | 1 | Bicomplex-step differentiation |
| scaled | 1 | Automatic variable scaling |
| <i>Initial Mesh Configuration</i> | | |
| numintervals | 50 | Initial mesh intervals per phase |
| initcolpts | 5 | Initial collocation points per interval |
| <i>Adaptive Mesh Refinement</i> | | |
| meshRefineType | 1 | hp-Patterson-Rao refinement |
| meshTol | 10^{-7} | Mesh convergence tolerance |
| maxMeshIter | 5 | Maximum refinement iterations |
| minColPts | 4 | Minimum collocation points per interval |
| maxColPts | 10 | Maximum collocation points per interval |
| <i>NLP Solver Configuration</i> | | |
| runIPOPTFlag | 1 | Enable IPOPT solver |
| NLPtol | 10^{-7} | NLP convergence tolerance |
| NLPmaxiter | 1000 | Maximum NLP iterations |
| linear_solver | MUMPS | IPOPT linear solver backend |
| <i>Control Structure Detection</i> | | |
| useLTIHDD | 1 | Bang-bang control detection |

in section 3.3. Diagram 3.4 represents the methodology used to develop and tune the PSO initialisation strategies, and section 3.4 provides a more in-depth description. Finally, diagram 3.5 shows how the final combinations of PSO and optimised solver are evaluated for their performance in the same three scenarios described previously.

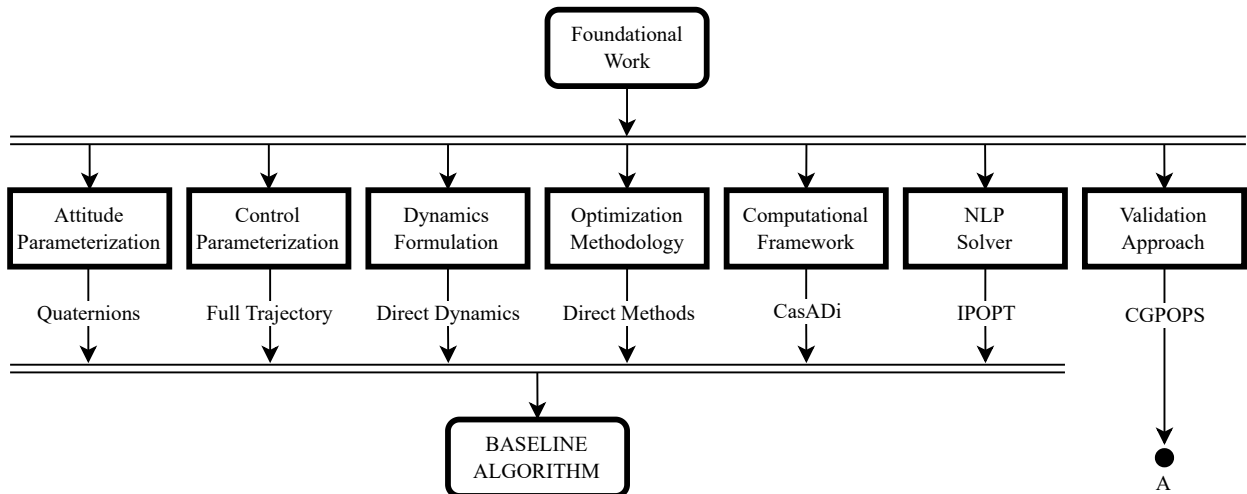


Figure 3.1 Foundational work and baseline algorithm implementation diagram.

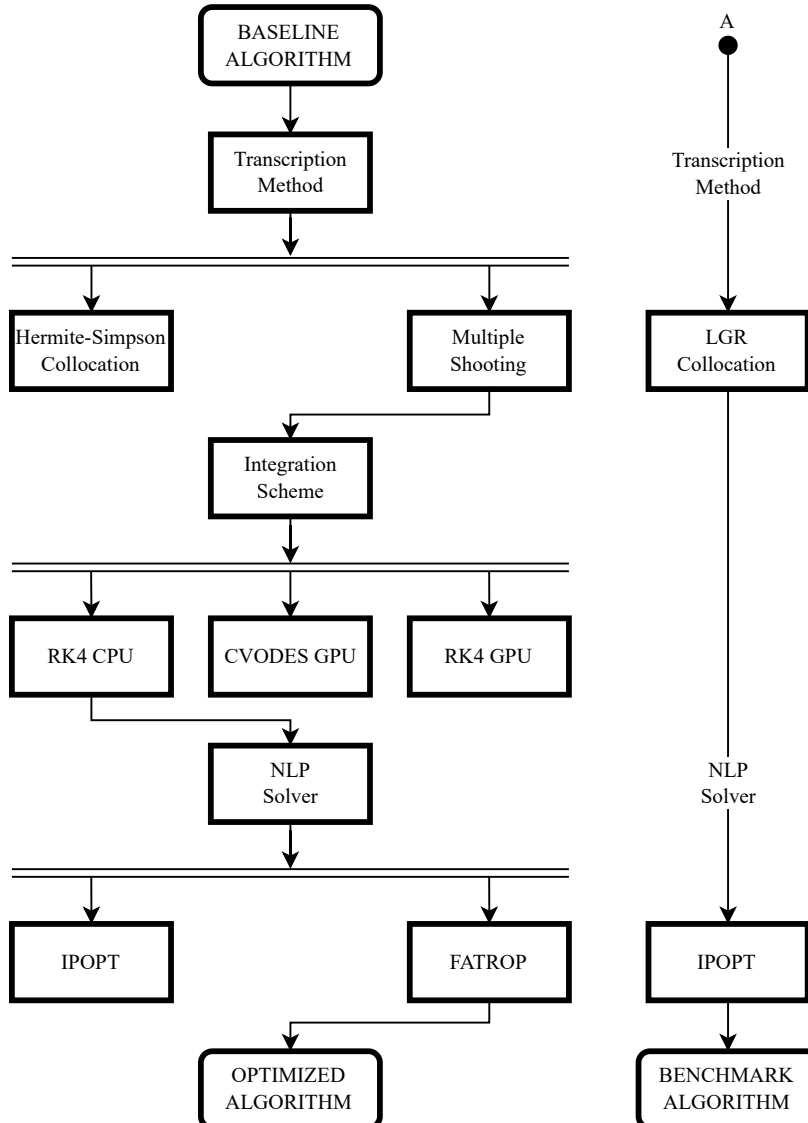


Figure 3.2 Optimised and benchmark algorithm development diagram.

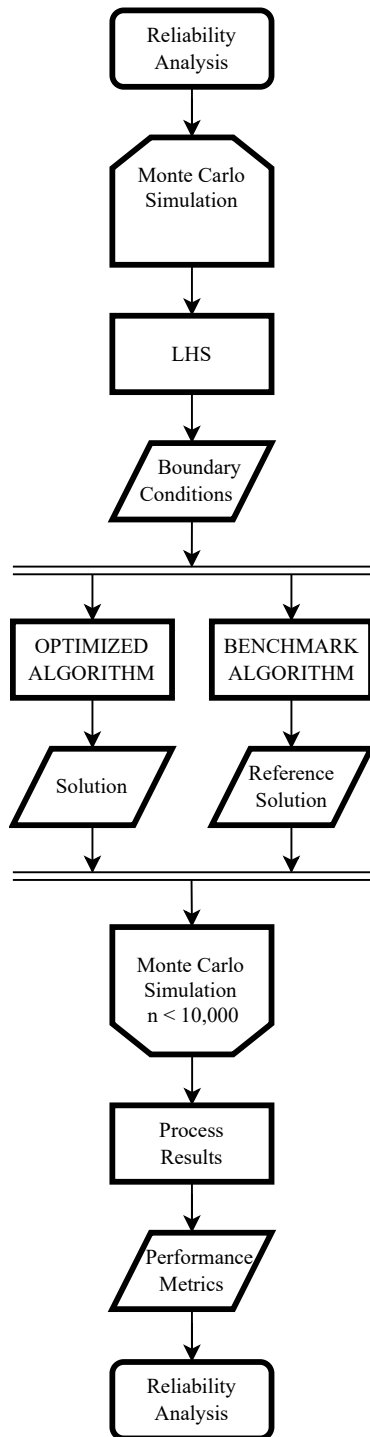
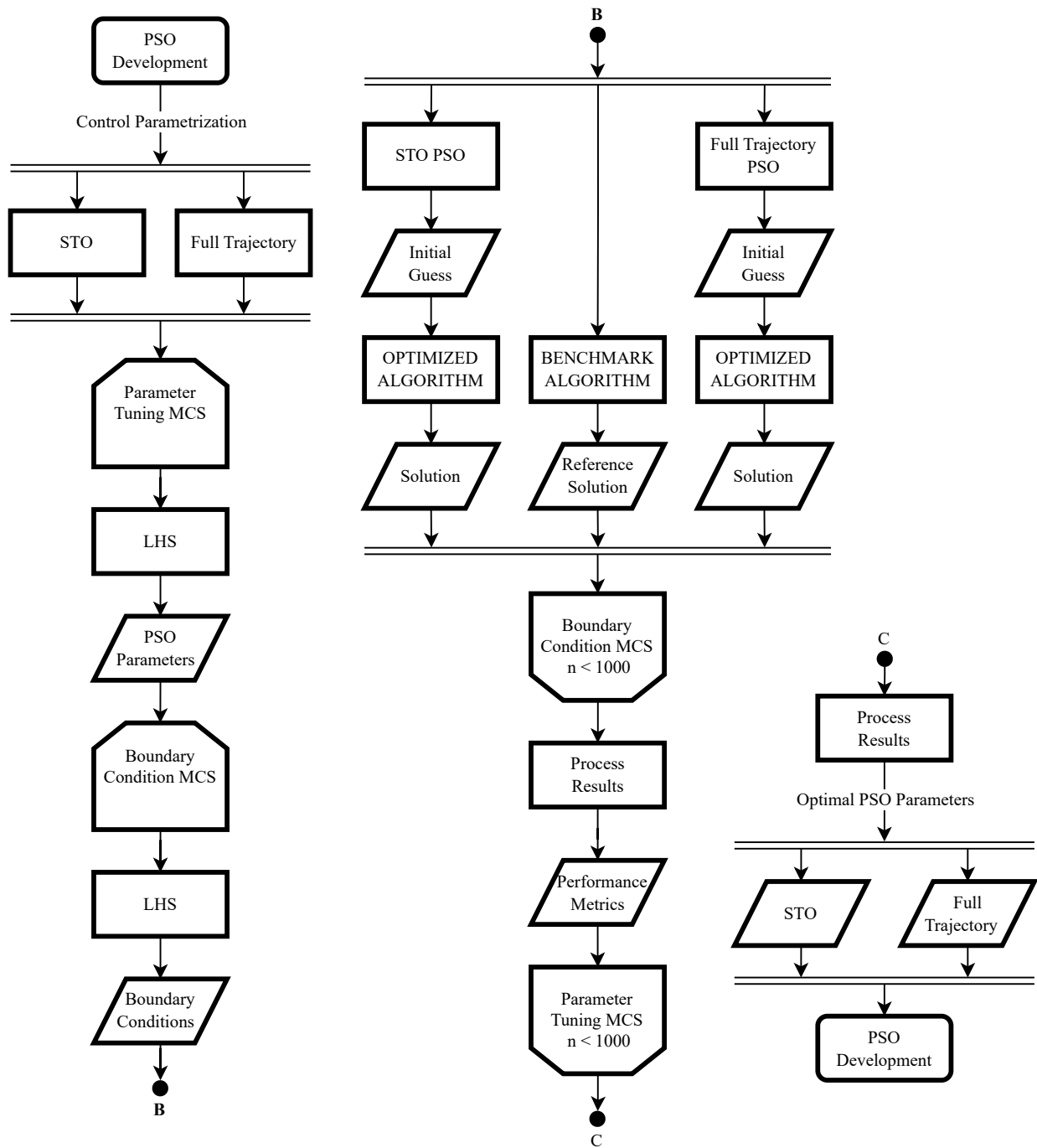


Figure 3.3 Optimised algorithm reliability analysis diagram.

**Figure 3.4** PSO development diagram.

3 Methodology

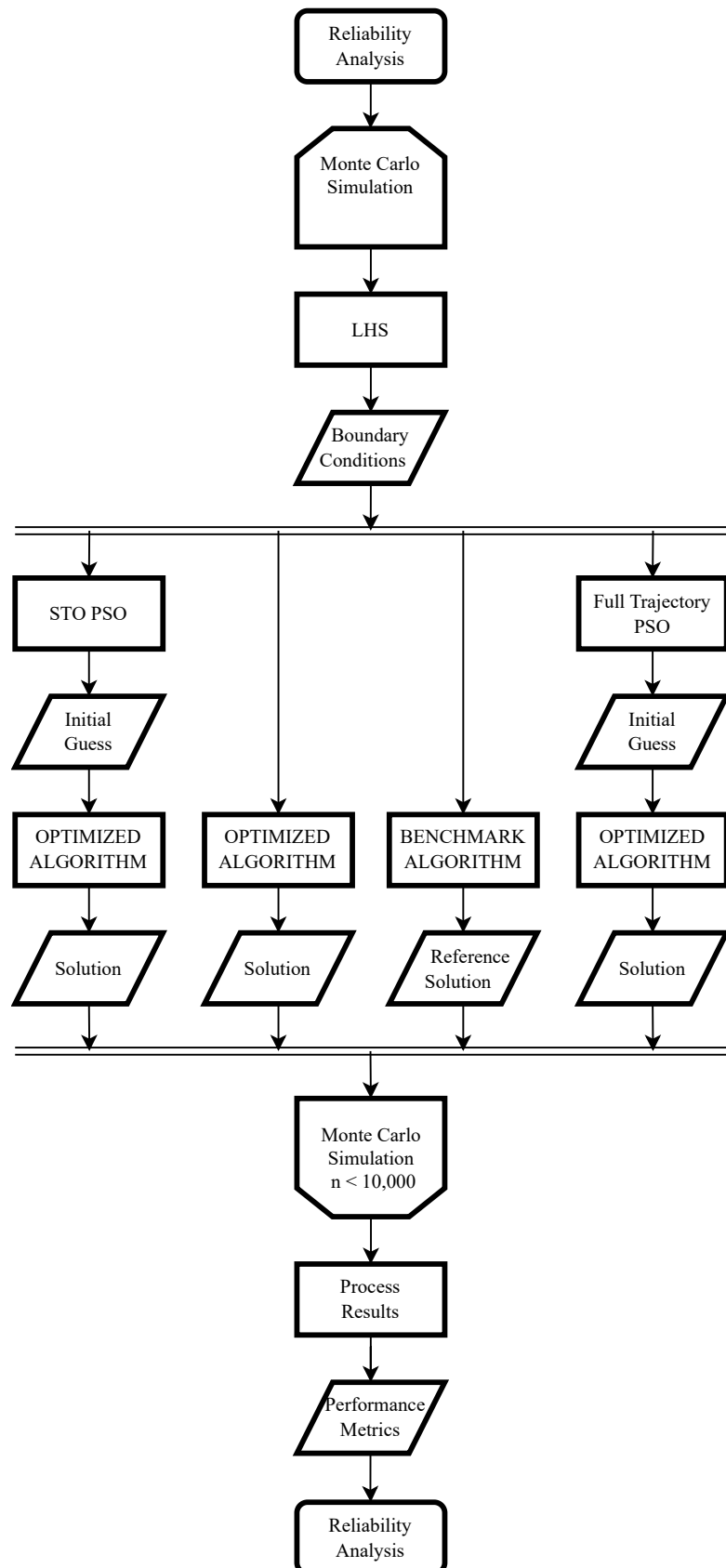


Figure 3.5 PSO reliability analysis.

4 Results

This chapter presents the numerical results obtained from the gradient-based optimisation framework developed in chapter 3. The performance of different transcription methods is evaluated through benchmark manoeuvres, and the computational characteristics of the implemented algorithms are analysed.

4.1 Gradient-based Strategy Optimisation Results

The numerical experiments are conducted using a symmetric spacecraft configuration with characteristic scales $J_0 = 1 \text{ kg}\cdot\text{m}^2$ and $\tau_{\max} = 1 \text{ N}\cdot\text{m}$ for simplicity. The spacecraft dynamics and optimal control problem formulation follow the definitions established in section 3.2. All manoeuvres consist of rest-to-rest reorientations about the first principal axis (roll axis), with initial condition $\mathbf{q}_0 = [1, 0, 0, 0]^T$.

4.1.1 Transcription Method Comparison

This section compares the computational performance and solution quality of multiple shooting paired with RK4 and Hermite-Simpson collocation transcription methods. A detailed framework and reasoning for method selection are found in section 3.2.1.

90° Manoeuvre

The time-optimal trajectories for the 90° rest-to-rest manoeuvre obtained via multiple shooting and Hermite-Simpson collocation are presented in figures 4.1 and 4.2, respectively. Both transcription methods successfully converged to optimal solutions satisfying the necessary conditions for optimality. However, despite utilising identical initial guess trajectories, the two methods converged to distinct local optima, as evidenced by the different control switching structures visible in figures 4.1d and 4.2d. This behaviour confirms the nonconvex nature of the time-optimal spacecraft reorientation problem discussed in section 2.5.2, wherein multiple locally optimal solutions exist in the optimisation landscape.

The Euler angle trajectories (figures 4.1a and 4.2a) demonstrate smooth monotonic rotation about the first principal axis, while the quaternion components (figures 4.1b and 4.2b) exhibit the characteristic evolution along the unit hypersphere. Angular velocity profiles (figures 4.1c and 4.2c) display the expected symmetry for rest-to-rest manoeuvres, with peak angular rates occurring near the trajectory midpoint. The control torque histories (figures 4.1d and 4.2d) exhibit bang-bang structure with 5 switches, consistent with PMP for time-optimal control of this problem class.

Quantitative performance metrics are summarised in table 4.1. The optimal manoeuvre duration serves as the baseline for error assessment. Multiple shooting achieved a manoeuvre duration of 2.4214 s with 0.012% error, while Hermite-Simpson collocation yielded 2.4220 s with 0.038% error. Multiple shooting demonstrated superior computational efficiency, requiring 0.961 s compared to 3.974 s for collocation (4× speedup and a 3× increase in accuracy). The increased computational efficiency and enhanced solution accuracy of multiple shooting demonstrate that problem sparsity is an advantage when solvers are capable of exploiting it, as is the case with IPOPT (section 2.6.1).

4 Results

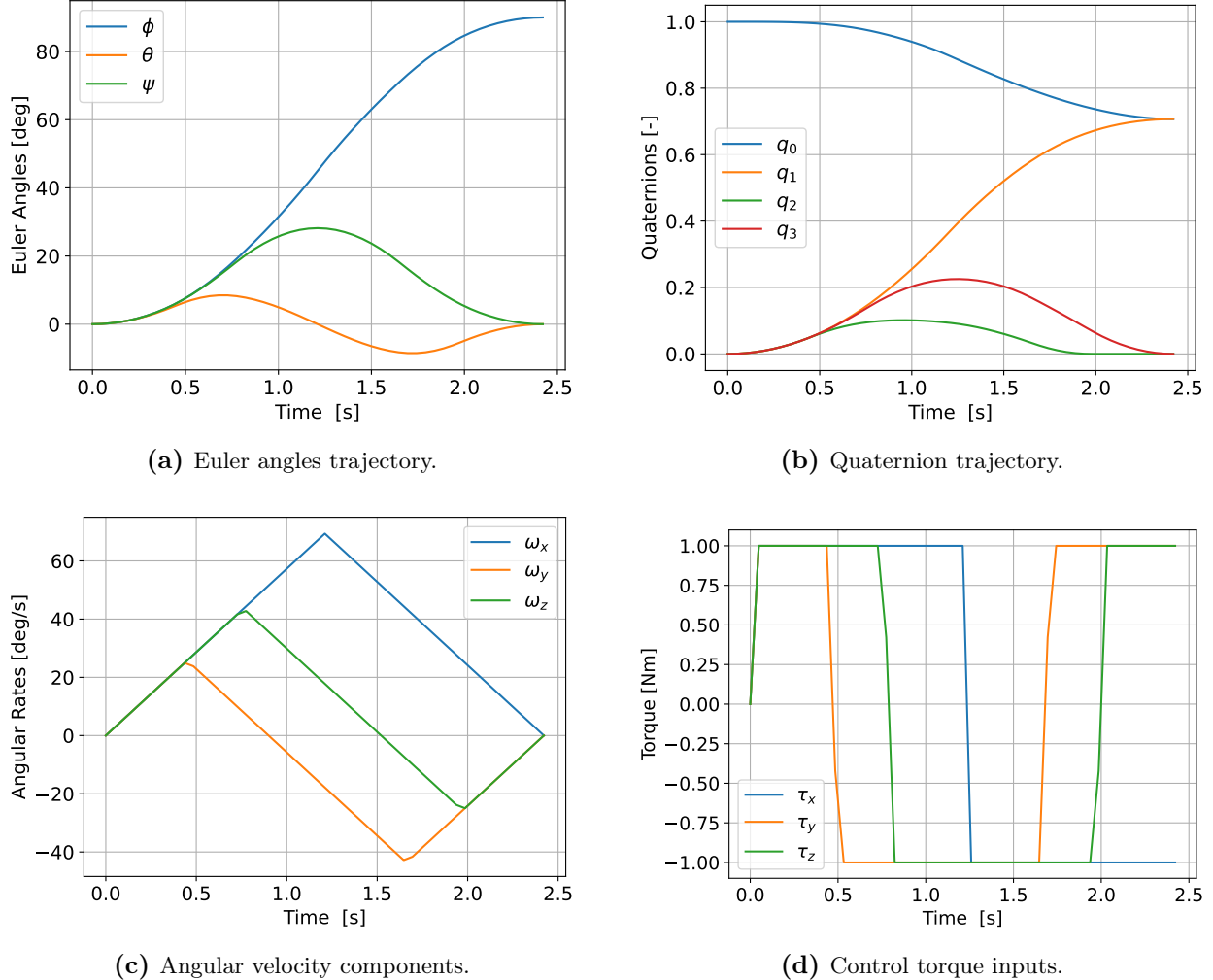


Figure 4.1 Time-optimal trajectory using multiple shooting transcription for a 90° manoeuvre.

Table 4.1 Performance comparison of transcription methods for a 90° manoeuvre.

| Metric | Optimal | Multiple Shooting | HS Collocation |
|--|---------|-------------------|----------------|
| Computation time [s] | — | 0.961 | 3.974 |
| Control switches [-] | 5 | 5 | 5 |
| Manoeuvre duration [s] | 2.4211 | 2.4214 | 2.4220 |
| Optimality gap Δ_{opt} [%] | 0 | 0.012 | 0.038 |

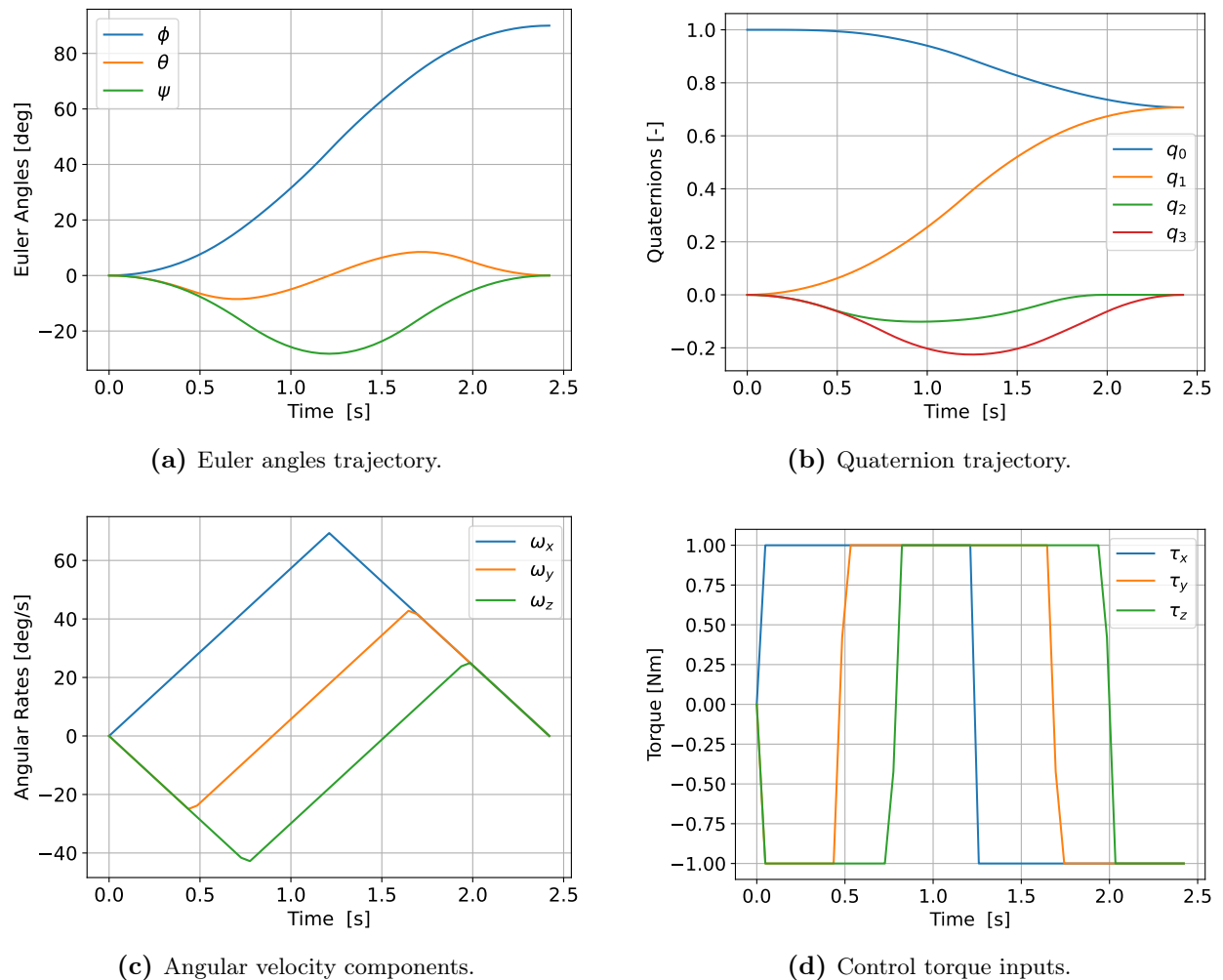


Figure 4.2 Time-optimal trajectory using Hermite-Simpson collocation transcription for a 90° manoeuvre.

4 Results

45° Manoeuvre

The optimal trajectories for the 45° manoeuvre are illustrated in figure 4.3. Unlike the 90° case, both transcription methods converged to the same optimal solution from the same initial guess. This may indicate that the 45° problem exhibits a more favourable optimisation landscape with stronger convergence properties toward the global optimum. However, no certain claims can be made without further analysis.

The control structure for this manoeuvre exhibits 6 switches, as shown in figure 4.3d. The successful identification of the 6-switch solution by both methods, rather than a suboptimal 7-switch structure, demonstrates the reliability of the implemented transcription approaches.

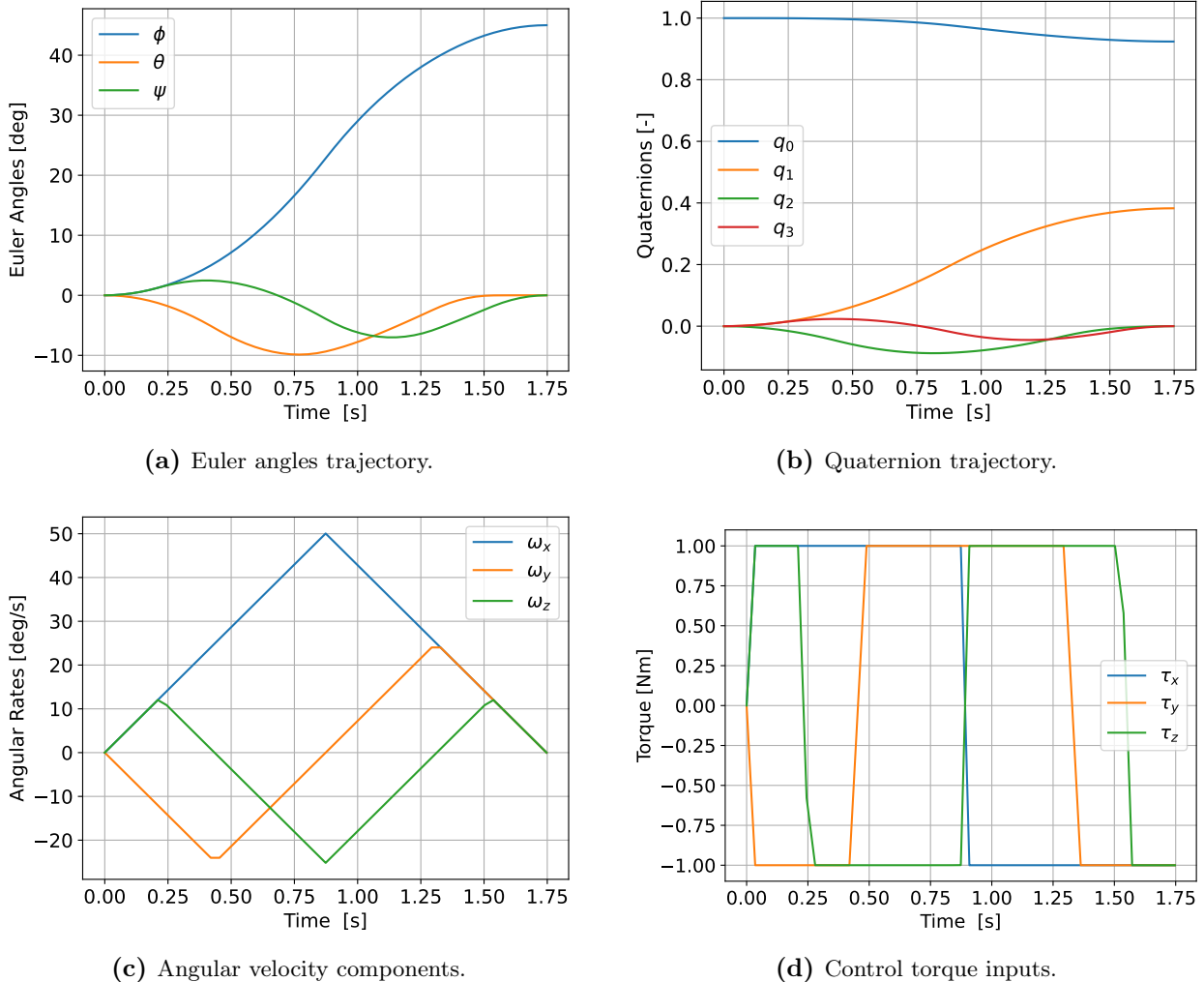


Figure 4.3 Time-optimal trajectory for a 45° manoeuvre.

Performance metrics in table 4.2 reveal that multiple shooting achieved 0.005% error with 1.265 s computation time, while Hermite-Simpson collocation yielded 0.031% error requiring 7.977 s: a 6× speedup and accuracy increase for multiple shooting.

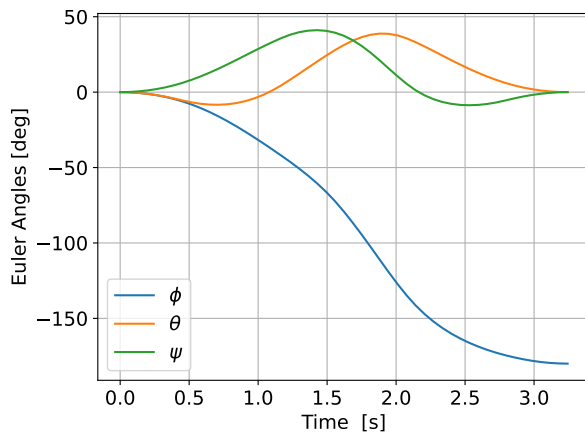
180° Manoeuvre

The 180° rest-to-rest manoeuvre represents the maximum rotation angle on SO(3) and poses particular challenges due to the quaternion sign ambiguity discussed in section 2.5.2. The optimal trajectories are presented in figure 4.4. Both transcription methods converged to identical optimal solutions exhibiting 5 control switches, as shown in figure 4.4d.

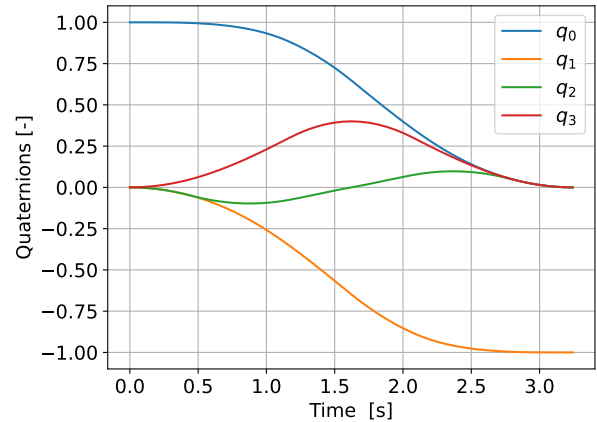
Table 4.2 Performance comparison of transcription methods for a 45° manoeuvre.

| Metric | Optimal | Multiple Shooting | HS Collocation |
|--|---------|-------------------|----------------|
| Computation time [s] | — | 1.265 | 7.977 |
| Control switches [-] | 6 | 6 | 6 |
| Manoeuvre duration [s] | 1.7471 | 1.7472 | 1.7476 |
| Optimality gap Δ_{opt} [%] | 0 | 0.005 | 0.031 |

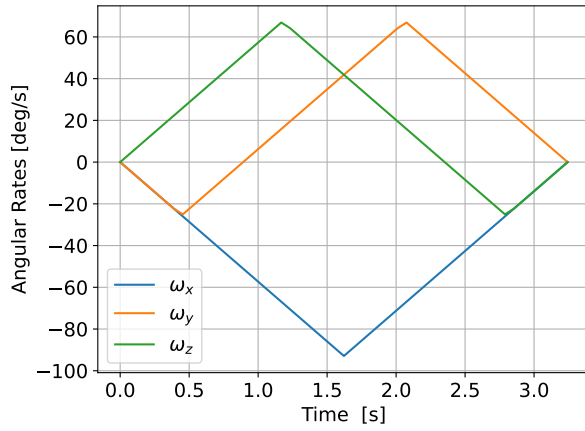
The quaternion trajectory in figure 4.4b demonstrates that the sign convention enforcement procedure (equation (2.50)) successfully prevented quaternion unwinding, ensuring convergence to the minimum-time solution corresponding to rotation through 180° rather than 540°. The angular velocity profile in figure 4.4c exhibits higher peak magnitudes compared to smaller-angle manoeuvres, reflecting the increased rotational momentum required for the longer slew.



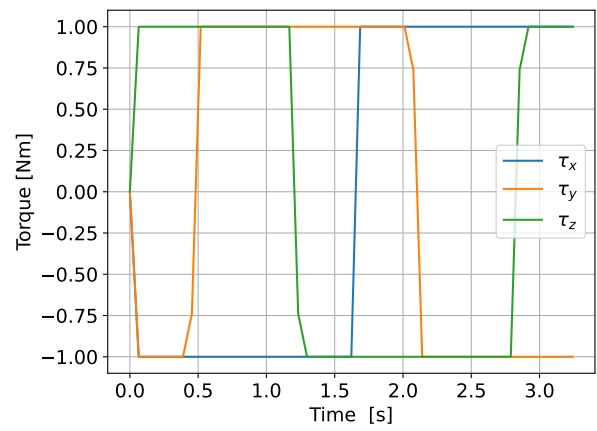
(a) Euler angles trajectory.



(b) Quaternion trajectory.



(c) Angular velocity components.



(d) Control torque inputs.

Figure 4.4 Time-optimal trajectory for a 180° manoeuvre.

Computational performance data in table 4.3 show that multiple shooting required 2.512 s with 0.009% error, while collocation required 4.512 s with 0.046% error, corresponding to a 1.8× speedup and a 5× increase in accuracy. The reduced computational advantage of multiple shooting for this case, compared to the 45° and 90° manoeuvres, may be attributed to the increased problem complexity arising from the larger rotation angle and the associated longer trajectory duration.

Table 4.3 Performance comparison of transcription methods for a 180° manoeuvre.

| Metric | Optimal | Multiple Shooting | HS Collocation |
|---|---------|-------------------|----------------|
| Computation time [s] | – | 2.512 | 4.512 |
| Control switches [-] | 5 | 5 | 5 |
| Manoeuvre duration [s] | 3.2431 | 3.2434 | 3.2446 |
| Optimality gap $\Delta_{\text{opt}} [\%]$ | 0 | 0.009 | 0.046 |

Across all three test cases, multiple shooting consistently demonstrated superior computational efficiency while achieving lower solution errors simultaneously. These results validate the selection of multiple shooting as the transcription method for the rest of the algorithm development.

4.1.2 Integration Scheme Comparison

With multiple shooting selected as the transcription method, the integration scheme used to propagate the system's dynamics is evaluated. Three methods are compared: a CPU and a GPU implementation of RK4, and a GPU implementation of CVODES. Since the solver settings are changed for this analysis (as explained in section 3.2.2), the results from the CPU-RK4 implementation in this section are different from the ones presented in the previous section.

Table 4.4 shows the results obtained for the 3 different manoeuvres. Among the three dynamics propagation approaches, the CPU-RK4 was consistently the fastest and also the most accurate. Conversely, the GPU-accelerated CVODES took 53 to 1682× longer while not providing any improvement in accuracy. As for the GPU-RK4 implementation, computation times ranged from only 1.14× to 27× slower than its CPU equivalent.

Table 4.4 Performance comparison of integration methods for different manoeuvre angles.

| Angle | Metric | Optimal | CPU-RK4 | GPU-RK4 | GPU-CVODES |
|-------|---|---------|---------|---------|------------|
| 45° | Computation time [s] | – | 15.890 | 18.129 | 852.945 |
| | Control switches [-] | 6 | 6 | 6 | 6 |
| | Manoeuvre duration [s] | 1.7471 | 1.7472 | 1.7476 | 1.7473 |
| | Optimality gap $\Delta_{\text{opt}} [\%]$ | 0 | 0.005 | 0.027 | 0.014 |
| 90° | Computation time [s] | – | 2.147 | 59.575 | 3612.220 |
| | Control switches [-] | 5 | 5 | 5 | 5 |
| | Manoeuvre duration [s] | 2.4211 | 2.4214 | 2.4214 | 2.4225 |
| | Optimality gap $\Delta_{\text{opt}} [\%]$ | 0 | 0.012 | 0.012 | 0.059 |
| 180° | Computation time [s] | – | 6.957 | 121.336 | 1559.010 |
| | Control switches [-] | 5 | 5 | 5 | 5 |
| | Manoeuvre duration [s] | 3.2431 | 3.2434 | 3.2434 | 3.2434 |
| | Optimality gap $\Delta_{\text{opt}} [\%]$ | 0 | 0.009 | 0.009 | 0.009 |

The GPU-accelerated CVODES implementation is abandoned due to its poor performance, combined with its more complex interface and reduced customisation options. Regarding the GPU-RK4 implementation, its performance is further studied. The findings are presented in table 4.5. CPU-GPU synchronisation overhead constitutes 71.3% of the total computational budget, while GPU kernel execution and memory transfers account for 13.0% of runtime. The ratio of CPU-side CUDA API blocking time (83.760 s) to actual GPU active time (12.902 s) yields a synchronisation efficiency of 15.4%, indicating that the implementation is synchronisation-bound rather than compute-bound. This bottleneck originates from synchronous memory transfer operations that serialise CPU-GPU execution, preventing concurrent operation of host and device. The IPOPT nonlinear programming

solver contributes 6.343 s of computational overhead for constraint Jacobian evaluations and KKT system assembly, representing 6.4% of total runtime.

Table 4.5 Computational performance breakdown of the GPU-accelerated optimisation framework using RK4 for a 180° rotation.

| Operation Category | Time (s) | Percentage (%) |
|----------------------------------|----------|----------------|
| Total Optimisation Runtime | 99.383 | 100.0 |
| GPU Operations | | |
| Kernel Execution | 7.739 | 7.8 |
| Memory Transfers | 5.163 | 5.2 |
| Total GPU Active Time | 12.902 | 13.0 |
| CPU Operations | | |
| IPOPT Solver Overhead | 6.343 | 6.4 |
| Function Evaluation Overhead | 8.588 | 8.6 |
| Total CPU Computation Time | 14.931 | 15.0 |
| CPU-GPU Synchronisation Overhead | 70.858 | 71.3 |

The profiling data also revealed 995,866 kernel invocations distributed across 1,656 gradient evaluations. Considering that the solver is using finite differences to compute the Jacobian, and that there are 11 decision variables (7 states, 3 controls, and the time step size) for every one of the 50 discretisation points, $50 \times 11 = 550$ kernel calls are made for every Jacobian evaluation. This means that $550 \times 1,656 = 910,800$ out of the 995,866 kernel calls stem from Jacobian evaluation. Since every discretisation point is independent from the other points, finite differences analysis can be implemented at every one of the 50 shooting intervals, simultaneously reducing the number of calls per Jacobian evaluation from 550 to 11. Table 4.6 compares the performance of this new approach with the CPU-RK4 implementations using finite differences (FD) and automatic differentiation (AD) for gradient computation. A clear performance improvement is observed, with results comparable to those of the CPU implementation using FD. However, computation times still remain superior to those achieved when using AD. To achieve results comparable to those achieved with AD, exact Jacobian and Hessian formulations would need to be implemented.

Table 4.6 Performance comparison of different RK4 integration implementations.

| Angle | Metric | CPU-RK4 FD | GPU-RK4 | CPU-RK4 AD |
|-------|--|------------|---------|------------|
| 45° | Computation time [s] | 15.890 | 8.5087 | 1.265 |
| | Control switches [-] | 6 | 6 | 6 |
| | Manoeuvre duration [s] | 1.7472 | 1.7472 | 1.7473 |
| | Optimality gap Δ_{opt} [%] | 0.005 | 0.005 | 0.005 |
| 90° | Computation time [s] | 2.147 | 5.8627 | 0.961 |
| | Control switches [-] | 5 | 5 | 5 |
| | Manoeuvre duration [s] | 2.4214 | 2.4214 | 2.4214 |
| | Optimality gap Δ_{opt} [%] | 0.012 | 0.012 | 0.012 |
| 180° | Computation time [s] | 6.957 | 5.753 | 2.512 |
| | Control switches [-] | 5 | 5 | 5 |
| | Manoeuvre duration [s] | 3.2434 | 3.2434 | 3.2434 |
| | Optimality gap Δ_{opt} [%] | 0.009 | 0.009 | 0.009 |

The performance analysis presented in table 4.7 demonstrates that the optimised GPU implementation achieves a $17.3\times$ speedup compared to the previous GPU implementation (5.753 s versus 99.383 s), reducing IPOPT gradient evaluations from 1,656 to 142 gradient evaluations. The GPU active time constitutes 7.1% of total runtime (0.406 s), comprising 0.248 s for kernel execution across 31,895 invocations and 0.158 s for memory transfers. Pure CPU computation accounts for 43.4% of runtime, with the IPOPT solver framework consuming 1.815 s (31.5%) for gradient evaluations and constraint processing. The CPU-GPU synchronisation overhead represents 49.6% of total runtime (2.853 s). Despite achieving a $31.2\times$ reduction in kernel invocations relative to the baseline, the GPU implementation (5.753 s) remains $2.3\times$ slower than the CPU-RK4 version employing automatic differentiation (2.512 s). This performance deficit is attributed to an insufficient problem scale for effective GPU utilisation: with 50 discretisation intervals and 7 states, only $50 \times 7 = 350$ threads are active per invocation, achieving approximately 3.4% of the theoretical thread capacity. The computational overhead associated with kernel launches and memory transfers is not amortised at this problem scale, rendering the GPU approach inefficient for this use case.

Table 4.7 Computational performance breakdown of the GPU-accelerated optimisation framework using RK4 with structure-exploiting gradient computation for a 180° rotation.

| Operation Category | Time (s) | Percentage (%) |
|----------------------------------|----------|----------------|
| Total Optimisation Runtime | 5.753 | 100.0 |
| GPU Operations | | |
| Kernel Execution | 0.248 | 4.3 |
| Memory Transfers | 0.158 | 2.7 |
| Total GPU Active Time | 0.406 | 7.1 |
| CPU Operations | | |
| IPOPT Solver Overhead | 1.815 | 31.5 |
| Function Evaluation Overhead | 0.679 | 11.8 |
| Total CPU Computation Time | 2.494 | 43.4 |
| CPU-GPU Synchronisation Overhead | 2.853 | 49.6 |

4.1.3 NLP Solver Comparison

Using a multiple shooting discretisation scheme with $N = 50$ intervals, employing RK4 integration with automatic differentiation on the CPU for dynamics propagation, two interior-point NLP solvers are evaluated: IPOPT and FATROP, a structured optimal control problem solver exploiting the special block-sparse structure of multiple shooting formulations (section 2.6.1). The comparative performance analysis presented in table 4.8 demonstrates that both solvers converge to equivalent solutions across all tested manoeuvre angles, with identical control switching structures and manoeuvre durations within 0.005–0.012% of the theoretical optimal values. However, FATROP achieves computation times of 0.085–0.191 s, compared to IPOPT’s 0.961–2.512 s, representing a consistent speedup factor of $9.0\text{--}14.9\times$. This performance advantage is attributed to FATROP’s exploitation of the optimal control problem structure through specialised condensing and Riccati recursion algorithms, which reduce computational complexity relative to general-purpose interior-point methods. The sub-200 ms computation times achieved by FATROP satisfy the real-time feasibility requirements set in section 1.2. Consequently, FATROP is selected as the NLP solver for all subsequent computational experiments in this thesis.

Table 4.8 Performance comparison of IPOPT and FATROP NLP solvers for different manoeuvre angles.

| Angle | Metric | Optimal | IPOPT | FATROP |
|-------|--|---------|--------|--------|
| 45° | Computation time [s] | – | 1.265 | 0.085 |
| | Control switches [-] | 6 | 6 | 6 |
| | Manoeuvre duration [s] | 1.7471 | 1.7472 | 1.7472 |
| | Optimality gap Δ_{opt} [%] | 0 | 0.005 | 0.005 |
| 90° | Computation time [s] | – | 0.961 | 0.107 |
| | Control switches [-] | 5 | 5 | 5 |
| | Manoeuvre duration [s] | 2.4211 | 2.4214 | 2.4214 |
| | Optimality gap Δ_{opt} [%] | 0 | 0.012 | 0.012 |
| 180° | Computation time [s] | – | 2.512 | 0.191 |
| | Control switches [-] | 5 | 5 | 5 |
| | Manoeuvre duration [s] | 3.2431 | 3.2434 | 3.2434 |
| | Optimality gap Δ_{opt} [%] | 0 | 0.009 | 0.009 |

4.2 Algorithmic Reliability Analysis

To assess algorithmic reliability and computational performance, three distinct scenarios are evaluated through MC simulation. Scenario A represents a symmetric spacecraft executing rest-to-rest manoeuvres. Scenario B corresponds to a symmetric spacecraft performing track-to-track manoeuvres. Scenario C examines asymmetric spacecraft executing track-to-track manoeuvres, representing the most challenging configuration due to the effects of gyroscopic coupling.

For each scenario, 10,000 boundary condition sets were randomly sampled using LHS to ensure uniform coverage of the parameter space. All trials employed an identical fixed initial guess corresponding to a 90° rest-to-rest minimum-time rotation.

4.2.1 Success Rate

Figure 4.5 presents the convergence success rates for both algorithms across all scenarios. The CGPOPS benchmark algorithm demonstrates sensitivity to initialisation quality, with success rates declining from 82.5% in scenario A to 64.9% in scenario C. This degradation reflects the increasing difficulty of the optimisation landscape as problem complexity increases through the introduction of non-zero boundary velocities and inertial asymmetry.

The optimised algorithm exhibits substantially improved reliability, achieving relative success rates exceeding 100% in all scenarios. This counterintuitive result arises from the employed evaluation methodology: when CGPOPS failed to converge, solutions from the optimised algorithm were classified as successful if they satisfied convergence tolerances for both optimality and constraint violation. The relative success rate is calculated as the ratio of successful trials from the optimised algorithm to those from CGPOPS, expressed as a percentage. Values exceeding 100% indicate that the optimised algorithm converged to feasible, optimal solutions in cases where the benchmark failed. Scenario B exhibits the highest relative improvement (124.1%), corresponding to an absolute convergence rate of 88%, while scenario A experiences the highest absolute convergence rate of 91%. Scenario C, although still outperforming the benchmark algorithm, achieves only a 70% absolute convergence rate.

4.2.2 Computation Time

Figure 4.6 illustrates the computational performance characteristics of both algorithms. The CGPOPS benchmark algorithm exhibits median computation times ranging from approximately 2

4 Results

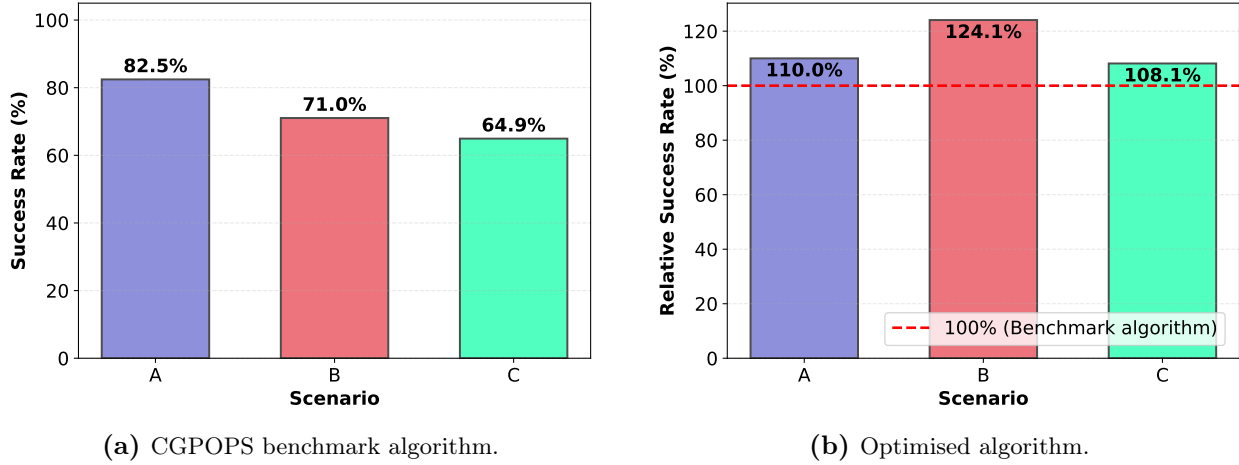


Figure 4.5 Success rate of the developed algorithms over the 3 different scenarios.

seconds in scenario A to 3 seconds in scenario C, with individual trials occasionally exceeding 10 seconds. This computational burden renders the benchmark unsuitable for real-time applications.

The optimised algorithm demonstrates dramatically reduced computation times across all scenarios. For scenarios A and B, the median computation time remains below the 0.2-second real-time threshold indicated by the dashed red line, with median values of approximately 0.125 seconds and 0.100 seconds, respectively. Scenario C exhibits increased computational demand due to its asymmetric inertia characteristics, with a median computation time of 0.295 seconds. However, when considering only successful convergence cases, the median computation time for scenario C remains 0.165 s, still satisfying real-time requirements.

The substantially tighter interquartile ranges observed in the optimised algorithm compared to the benchmark indicate more consistent and predictable computational performance, which is critical for operational deployment where deterministic timing guarantees are essential.

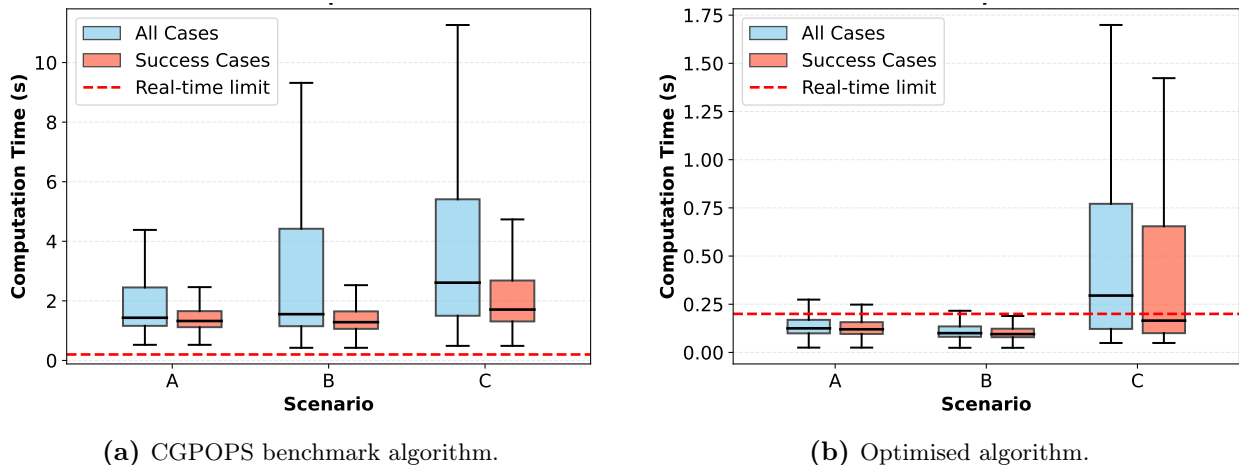


Figure 4.6 Computation time of the developed algorithms over the 3 different scenarios.

4.2.3 Solution Optimality

To quantify solution quality in cases where the optimised algorithm failed to converge but CGPOPS succeeded, the optimality gap is computed as the percentage difference in manoeuvre time relative to the CGPOPS solution. Figure 4.7 presents the distribution of this metric across non-converged trials. The goal of this analysis is to determine whether non-optimal solutions are acceptable, even if they do not correspond to the fastest trajectory.

Scenario A exhibits minimal optimality degradation, with a median deviation of approximately 0.2% and the 75th percentile remaining below 1%. This near-optimal performance suggests that even non-converged solutions from the optimised algorithm provide trajectories of practical utility for symmetric rest-to-rest manoeuvres.

Scenario B demonstrates an increased optimality gap, with a median deviation of 0.5%. The larger gap reflects the additional complexity introduced by non-zero boundary velocities, which expands the feasible solution space and increases the probability of convergence to suboptimal local minima.

Scenario C presents the largest optimality gaps, with a median deviation of approximately 1% and the third quartile percentile reaching 8.8%. The increased gap in asymmetric configurations correlates with the more complex optimisation landscape characterised by multiple local minima separated by regions of infeasibility, which are a consequence of gyroscopic coupling effects.

Notably, even in worst-case scenarios, the optimality gap remains below 9%, indicating that the optimised algorithm consistently identifies solutions in the vicinity of the global optimum. Nevertheless, it is decided to improve these results by introducing PSO initialisation strategies to understand how dependent they are on the initial guess.

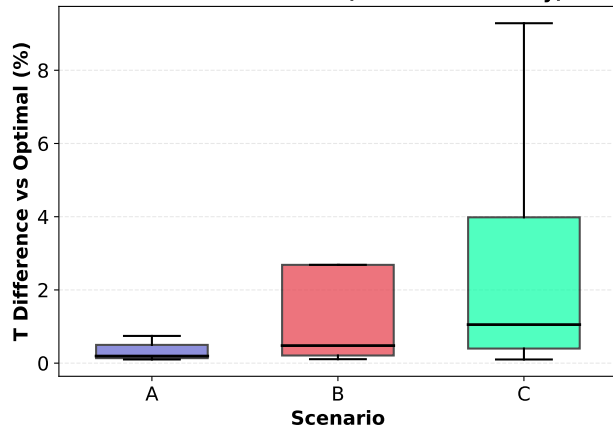


Figure 4.7 Optimality gap for non-converged runs of the optimised algorithm.

4.3 PSO Development

The reliability analysis presented in section 4.2 demonstrated that while the optimised algorithm achieves substantial improvements over the CGPOPS benchmark, convergence success rates decline in complex scenarios, particularly for asymmetric spacecraft configurations. Additionally, the optimality gap analysis revealed that non-converged solutions can deviate from the global optimum by up to 9%. These observations motivate the investigation of metaheuristic initialisation strategies to enhance both reliability and solution quality.

This section presents the results of two PSO-based initialisation approaches: full control trajectory parameterisation and STO parameterisation. The objective is to position the NLP solver within the convergence basin of the global optimum, thereby improving both success rate and solution quality across all scenario classes.

4.3.1 Parameter Tuning Results

Following the LHS-based parameter tuning methodology detailed in section 3.4.2, optimal PSO configurations for both parameterisation approaches were identified through evaluation of 1000 parameter combinations across 1000 independent manoeuvre scenarios each. Table 4.9 presents the

resulting optimal parameter sets, which exhibit substantial differences reflecting the distinct search space characteristics of full control trajectory versus STO parameterisation.

Table 4.9 PSO optimal parameters.

| Category | Parameter | Full Control | STO |
|---------------------|-------------------------------|--------------|------|
| Population | Population size \mathcal{N} | 3200 | 3200 |
| | Iteration count \mathcal{K} | 10 | 100 |
| Inertia Weight | Initial weight w_0 | 3.5 | 5.6 |
| | Minimum weight $w_{0,\min}$ | 0.0 | 3.2 |
| Cognitive Parameter | Initial weight w_1 | 4.8 | 4.8 |
| | Minimum weight $w_{1,\min}$ | 1.5 | 1.7 |
| Social Parameter | Initial weight w_2 | 1.7 | 6.0 |
| | Minimum weight $w_{2,\min}$ | 1.5 | 6.0 |
| Binary PSO | Sigmoid scaling α | — | 7.9 |
| | Sigmoid saturation ϵ | — | 0.57 |

The optimal configurations reveal fundamentally different search strategies driven by the disparity in dimensionality between parameterisation approaches. Full control trajectory parameterisation, with its $O(151)$ -dimensional search space, performs optimally with only 10 iterations, which is compensated for by an aggressive inertia weight decay ($w_{0,\min} = 0.0$, representing a complete transition to exploitation). This rapid convergence strategy reflects the challenge of high-dimensional optimisation where exhaustive exploration is computationally prohibitive.

In contrast, STO parameterisation exploits its substantially reduced $O(10)$ -dimensional search space through sustained exploration over 100 iterations with maintained inertia ($w_{0,\min} = 3.2$). The tenfold increase in iteration count, while remaining within computational budget, enables more thorough coverage of the compact search space. The preserved high social parameter ($w_2 = w_{2,\min} = 6.0$) promotes convergence toward global best positions, appropriate for initialisation strategies, whose focus is purely finding the global minimum basin and not the minimum itself.

Both parameterisations converge on identical population sizes $\mathcal{N} = 3200$, which is five times the available GPU core count, balancing parallel efficiency with population diversity, a crucial factor for effective parameter space exploration. The cognitive parameter initialisation ($w_1 = 4.8$) remains consistent across both approaches, indicating that individual particle memory contributes similarly to search effectiveness regardless of dimensionality.

The binary PSO parameters for STO parameterisation ($\alpha = 7.9$, $\epsilon = 0.57$) indicate preference for sharp sigmoid transitions with moderate stochasticity. The high sigmoid scaling creates decisive initial control sign switching decisions, while the saturation threshold slightly above the minimum ($\epsilon = 0.57 > 0.5$) leads to an almost purely stochastic behaviour, which forces exploration of discrete control directions even with high particle velocities. This is expected for an initialisation strategy whose goal is to properly explore the solution space and find a global optimum basin.

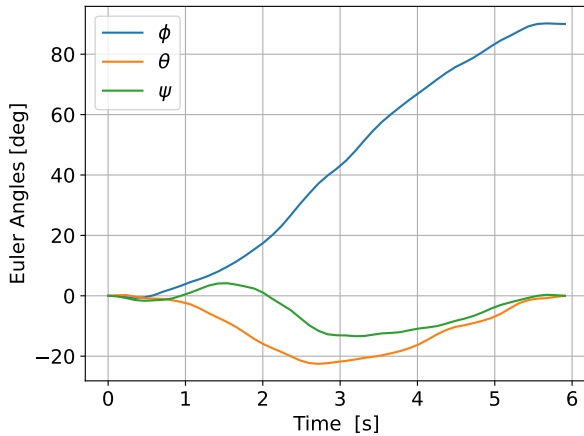
4.3.2 Trajectory Visualisation

To visualise the difference between the trajectories generated by both approaches, they are evaluated on a 90° rest-to-rest reorientation about the roll axis, corresponding to the optimal manoeuvre analysed in figure 4.1 and table 3.2. From analytical solutions, it is known that the control trajectory exhibits five control switches and a manoeuvre duration of 2.4211 s.

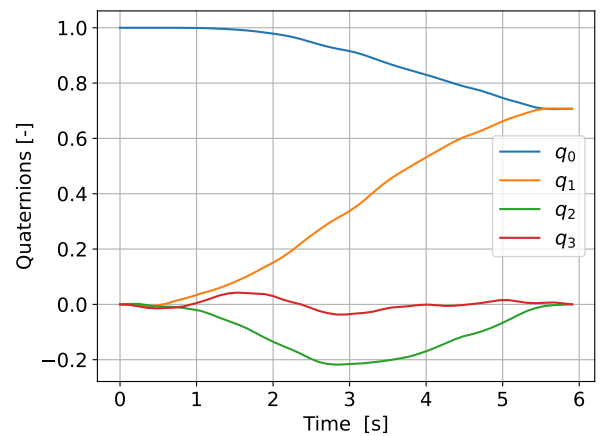
Figure 4.8 presents the trajectory generated by PSO with full control trajectory parameterisation. The Euler angle trajectory (figure 4.8a) demonstrates successful completion of the 90° rotation, though the quaternion evolution (figure 4.8b) exhibits deviations from the smooth hyperspherical

arc characteristic of optimal solutions. The angular velocity profile (figure 4.8c) displays significant oscillations throughout the manoeuvre rather than the symmetric acceleration-deceleration pattern observed in optimal trajectories. Most notably, the control torque history (figure 4.8d) exhibits highly oscillatory behaviour with frequent switching, deviating substantially from the optimal bang-bang structure. Despite satisfying the final state constraints, the manoeuvre duration is 5.9078 s, a 144% increase relative to the optimal value.

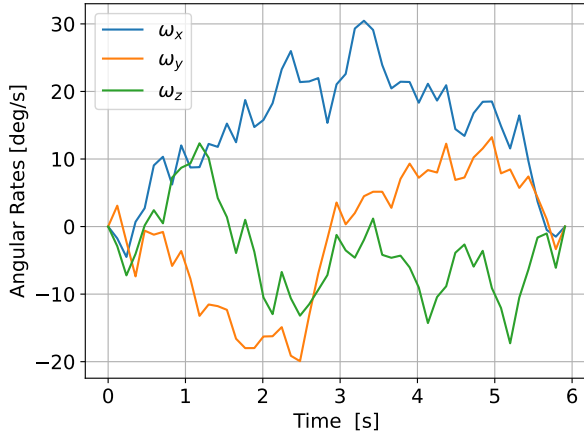
The excessive oscillations in the full control parameterisation trajectory reflect the high-dimensional optimisation landscape ($O(151)$ decision variables) and the limited exploitation phase (10 iterations with aggressive inertia decay to $w_{0,\min} = 0.0$). The PSO algorithm prioritises exploration over refinement, yielding feasible but inefficient trajectories. However, the key advantage of this approach lies in its ability to satisfy terminal constraints while providing the gradient-based solver with a feasible starting point within the global convergence basin.



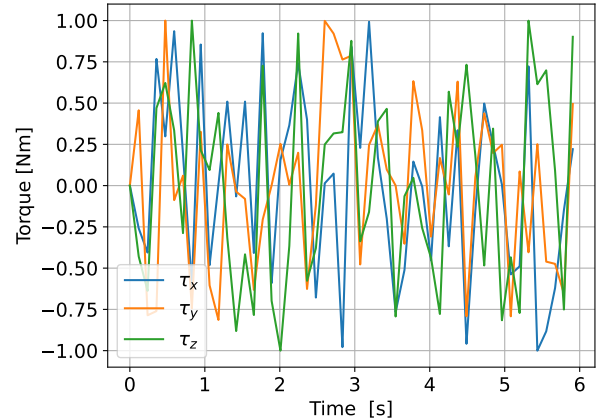
(a) Euler angles trajectory.



(b) Quaternion trajectory.



(c) Angular velocity components.



(d) Control torque inputs.

Figure 4.8 Output trajectory generated by the PSO with full control trajectory parameterisation.

Figure 4.9 presents the trajectory generated by PSO with STO parameterisation. The control torque history (figure 4.9d) exhibits the prescribed bang-bang structure with exactly 5 switches, matching the optimal control topology. The Euler angle trajectory (figure 4.9a) demonstrates smooth monotonic rotation, and the angular velocity profile (figure 4.9c) displays no oscillations, approaching the symmetric profile of the optimal solution. The manoeuvre duration of 2.2880 s represents only a 5.5% deviation from the optimal solution, indicating proximity to the global optimum. However, final state constraints are violated, with the spacecraft failing to achieve the required zero angular velocity and 90° roll attitude at the final time.

The superior trajectory structure and near-optimal manoeuvre duration of the STO parameterisation stem from the substantially reduced search space ($O(10)$ decision variables) and extended exploration phase (100 iterations with maintained inertia $w_{0,\min} = 3.2$). However, the constraint violation indicates that while STO parameterisation excels at identifying the correct control structure, the discrete nature of the switching topology introduces challenges in precisely satisfying boundary conditions.

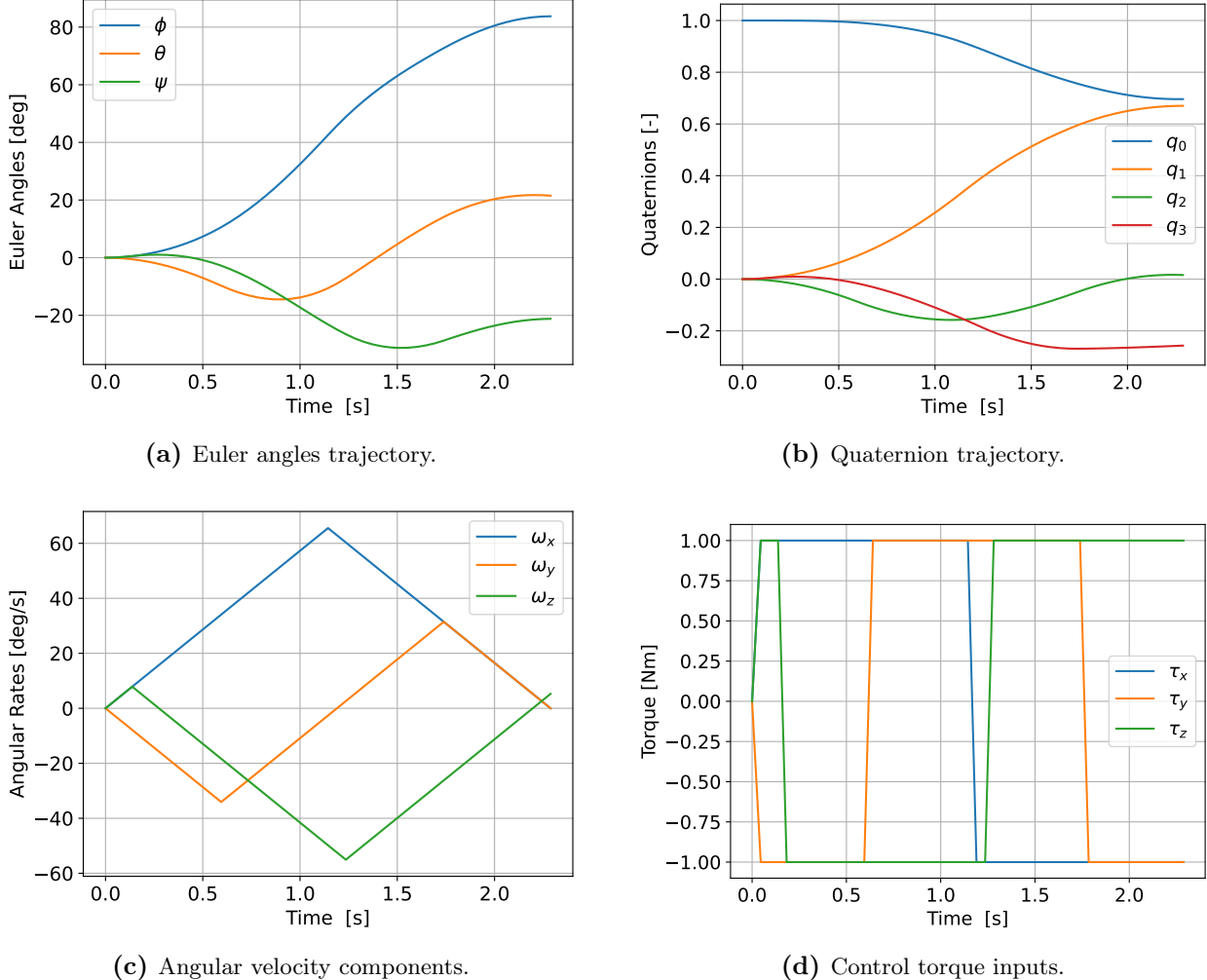


Figure 4.9 Output trajectory generated by the PSO with STO parameterisation.

These observations suggest that PSO serves most effectively as an initialisation strategy rather than a standalone solver. The metaheuristic phase positions the gradient-based solver within the appropriate convergence basin (either a feasible region (full control) or a structurally correct region (STO)) from which local refinement can converge to the constrained optimum. The subsequent reliability analysis (section 4.4) quantifies the extent to which these initialisation strategies enhance algorithmic performance across diverse scenario classes.

4.4 PSO Reliability Analysis

The reliability analysis presented in section 4.2 is extended to evaluate the performance of PSO-based initialisation strategies. The two developed PSO variants are examined, where: *PSO Full* refers to the optimised algorithm initialised with PSO with full control trajectory parameterisation, *PSO STO* refers to PSO with switch time optimisation parameterisation. The analysis compares

these approaches against both the benchmark CGPOPS algorithm and the optimised algorithm without PSO initialisation, referred to as *No PSO*.

4.4.1 Success Rate

Figure 4.10 presents the success rates achieved by the different initialisation strategies across all three scenarios. The initialisation approach demonstrates varying effects on convergence reliability depending on the scenario complexity and spacecraft configuration.

For scenarios A and B, *PSO Full* achieves slightly better success rates than *No PSO*. Contrarily, *PSO STO* exhibits a more pronounced reduction in success rates when compared to *No PSO*. However, it still outperforms the benchmark algorithm.

The most significant deviation occurs in scenario C, where PSO-based initialisation demonstrates unexpected behaviour. *No PSO* achieves a higher success rate than both PSO-initialed approaches. Most notably, *PSO STO* shows the lowest success rate among all methods for this scenario, even falling below the benchmark baseline by 2%.

The reduced success rates observed with *PSO STO*, particularly for asymmetric spacecraft configurations, can be attributed to the constrained solution space imposed by the fixed bang-bang control structure. The STO parameterisation inherently restricts the control trajectory to a pre-defined structure, creating steeper convergence basins in the solution landscape. When the PSO converges to a suboptimal basin, the subsequent gradient-based refinement encounters difficulty escaping due to the high quality of the non-optimal minimum, resulting in convergence to a local minimum rather than the global optimum. This effect is amplified in scenario C, where the asymmetric inertia distribution increases the complexity of the optimal control structure.

The counterintuitive result that the PSO initialisation, implemented specifically to enhance reliability for asymmetric spacecraft, performs worst in scenario C suggests that the current PSO implementations may require additional tuning of exploration-exploitation trade-offs. The PSO tuning has been carried out with rest-to-rest manoeuvres performed with a symmetric spacecraft. The results indicate that the tuning parameters may be dependent on the spacecraft configuration and require personalised tuning.

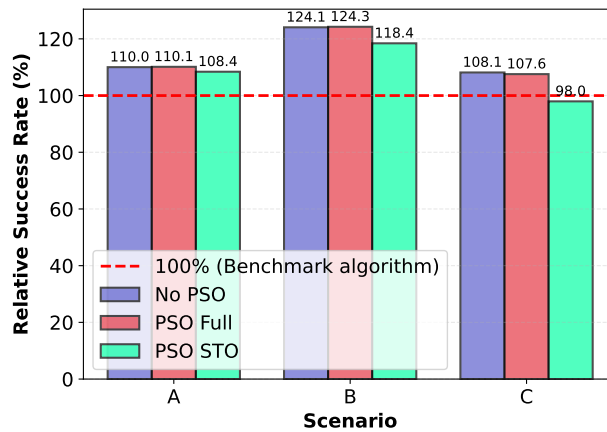


Figure 4.10 Success rate of the developed algorithm with different initialisation strategies.

4.4.2 Computation Time

Figures 4.11 and 4.12 present the computation time distributions for all cases, for successfully converged cases only, and also a breakdown of time spent in PSO versus gradient-based solver phases. The results reveal distinct performance characteristics across scenarios and parameterisation approaches.

4 Results

For scenarios A, both PSO variants achieve faster overall computation times compared to *No PSO*. As shown in figures 4.11a and 4.11b, *PSO Full* demonstrates a median computation time 0.007 s slower than *PSO STO* and 0.005 s faster than *No PSO*. For scenario B, both PSO implementations have a median 0.006 s slower than *No PSO*. Both methods maintain computation times substantially below the 0.2 s real-time threshold.

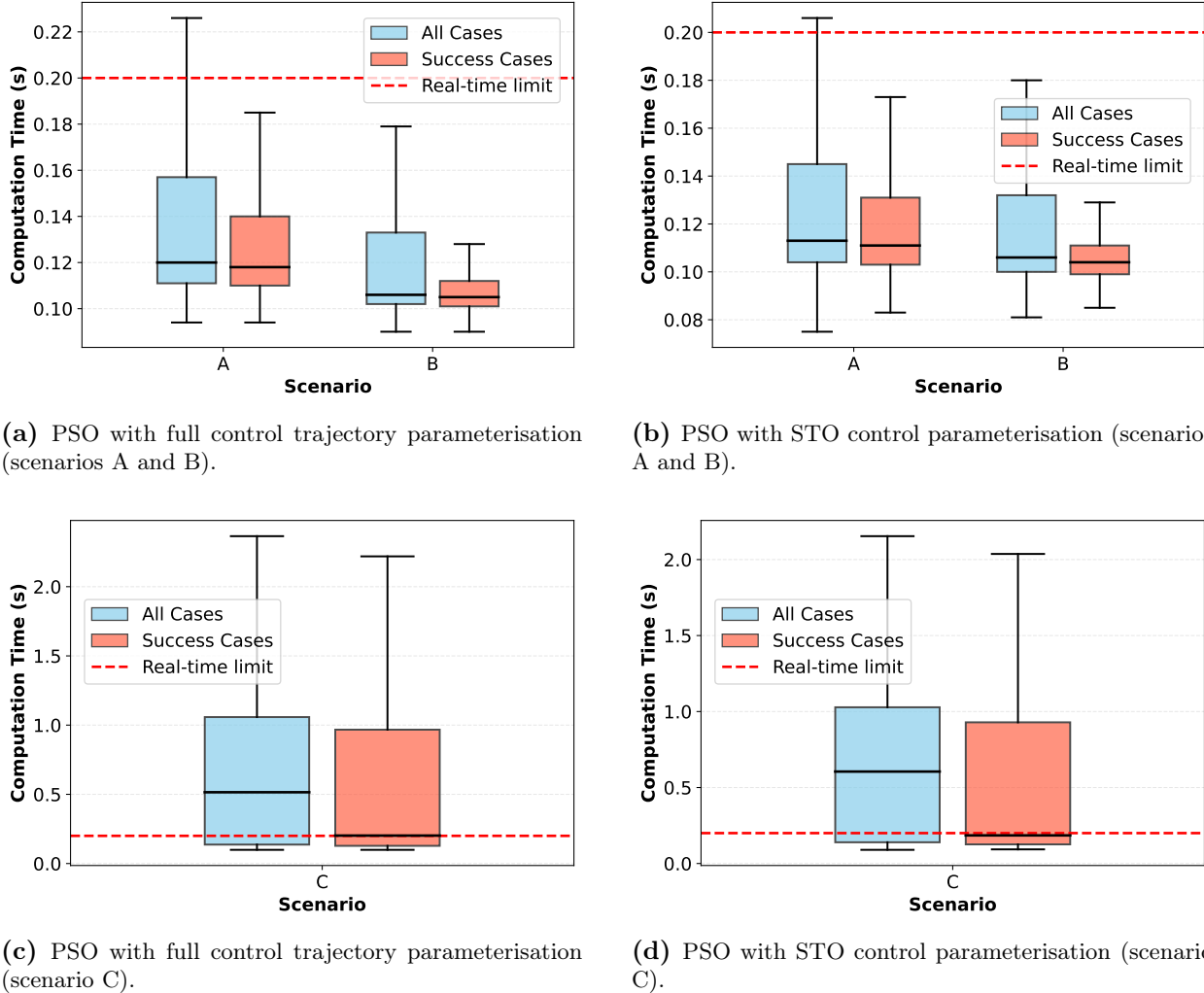


Figure 4.11 Computation time of the optimised algorithm with PSO initialisation.

The time breakdown analysis in figure 4.12 reveals that PSO computation time remains approximately constant across scenarios, with *PSO Full* requiring 0.08 s of PSO time, while *PSO STO* requires 0.07 s. The consistency of the PSO phase duration demonstrates the predictable computational cost of the metaheuristic initialisation phase. Notably, the gradient-based solver time following PSO initialisation is significantly reduced compared to the approximately 0.12 s of solver time in the *No PSO* for scenarios A and B, with *PSO Full* achieving a median solver time of 0.03 s, and *PSO STO* 0.04 s, indicating that improved initialisation quality reduces the refinement burden on the NLP solver.

Scenario C presents a contrasting behaviour, as shown in figures 4.11c, 4.11d, 4.12c and 4.12d. Despite PSO maintaining consistent computation times, the gradient-based solver requires substantially longer refinement periods, with median solver times of approximately 0.4 s for *PSO Full* and 0.5 s for *PSO STO*. This increased solver time results in overall median computation times of 0.515 s and 0.605 s, respectively, exceeding the 0.2 s real-time threshold in 62.01% (*PSO Full*) and 62.96% (*PSO STO*) of cases. The extended solver times in scenario C, combined with the previously discussed reductions in success rate, indicate that PSO initialisation provides less effective

starting points for asymmetric configurations, requiring more extensive gradient-based refinement and potentially converging to suboptimal local minima.

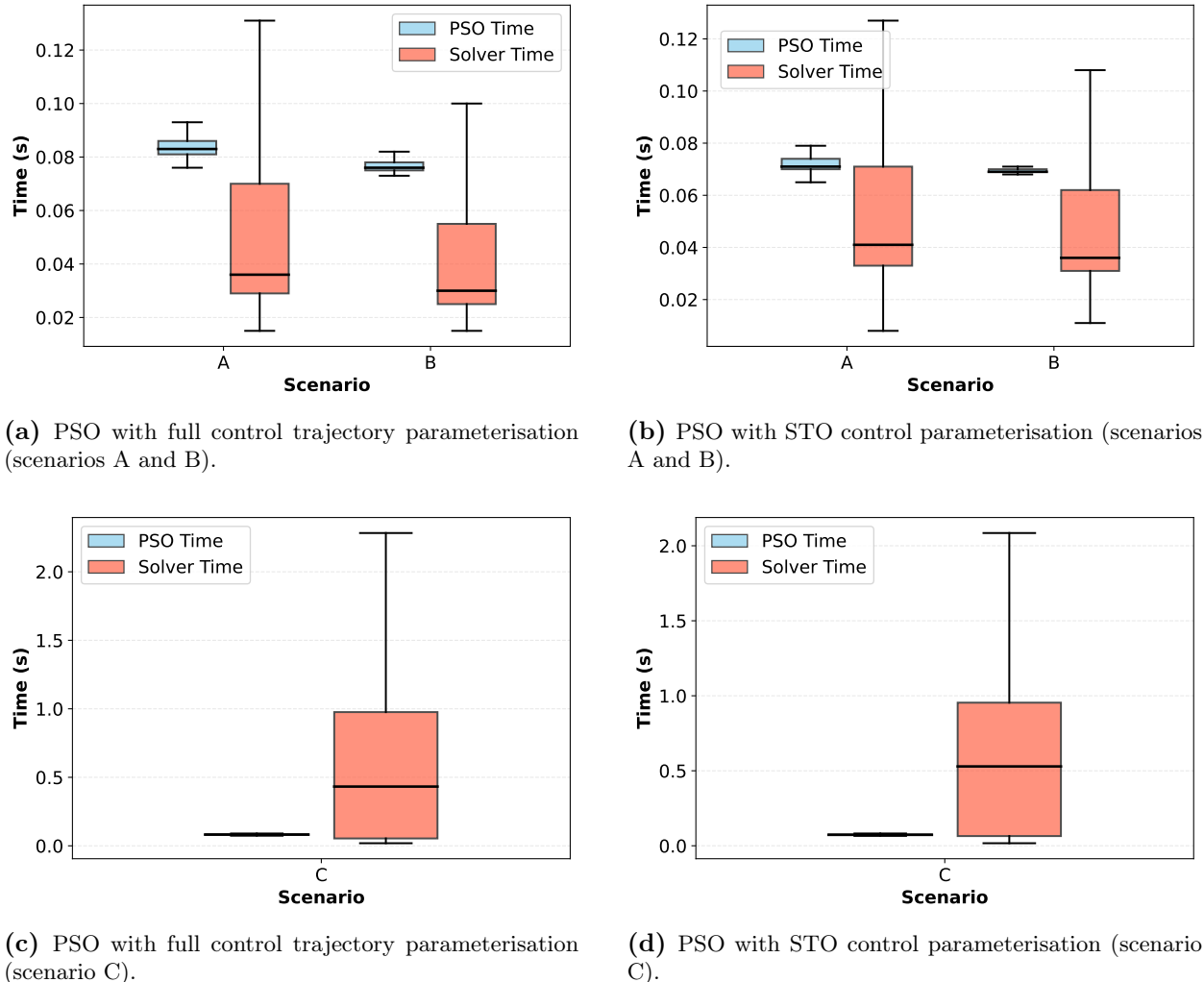


Figure 4.12 Discriminated computation time between time spent on PSO and on the gradient-based solver.

4.4.3 Solution Optimality

Figure 4.13 presents the optimality gap analysis for non-converged runs, quantified as the difference in manoeuvre time relative to converged CGPOPS solutions. The results demonstrate that the parameterisation approach has a significant influence on solution quality in cases of failed convergence.

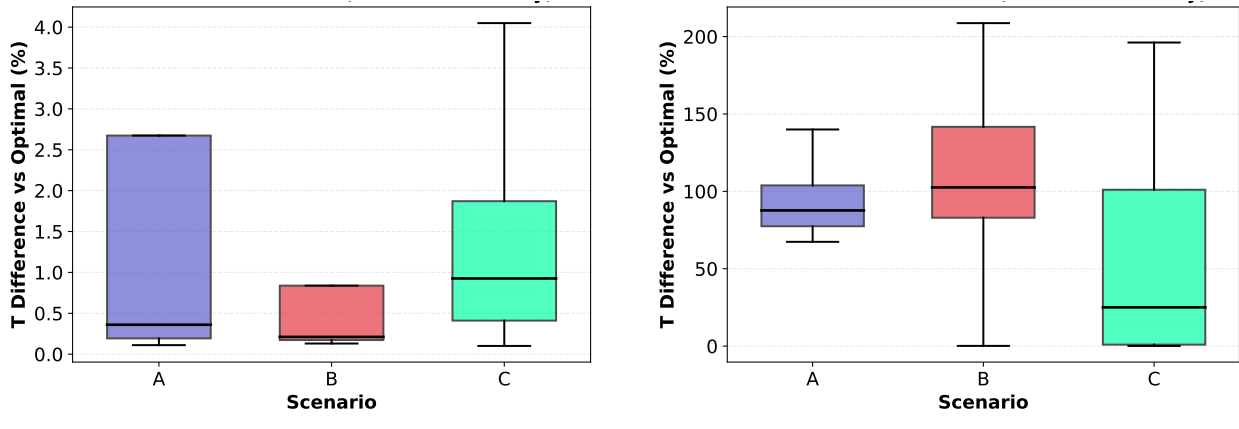
PSO Full exhibits relatively modest optimality gaps across all scenarios, as shown in figure 4.13a. Even scenario C, despite having the lowest success rate, maintains a median optimality gap of nearly 1.0%, although with increased variability, which extends to approximately 4.0% in extreme cases. These results indicate that when *PSO Full* fails to converge, the resulting suboptimal solutions remain relatively close to the optimal manoeuvre time.

In contrast, *PSO STO* demonstrates substantially larger optimality gaps, as illustrated in figure 4.13b. All scenarios exhibit a dramatic increase, with medians near 100% and errors extending to 200% in scenarios B and C. These pronounced optimality gaps directly correlate with the structural constraints imposed by STO parameterisation. The fixed bang-bang control structure creates distinct convergence basins in the solution space, each corresponding to a particular switching sequence. When the PSO converges to an incorrect switching sequence, the gradient-based solver

4 Results

encounters steep basin walls, resulting in convergence to a locally optimal solution within the incorrect basin.

This behaviour suggests that *PSO STO* would benefit from parameter tuning that emphasises solution refinement over exploration, potentially allowing the swarm to escape suboptimal basins before transitioning to gradient-based refinement. Additionally, implementing diversity-preserving mechanisms or multi-start strategies within the PSO phase could improve the probability of identifying the correct convergence basin, particularly for asymmetric configurations where the optimal switching structure is less intuitive.



(a) PSO with full control trajectory parameterisation.

(b) PSO with STO control parameterisation.

Figure 4.13 Optimality gap for non-converged runs of the optimised algorithm with PSO initialisation.

5 Conclusion

This thesis addresses the challenge of computing time-optimal spacecraft attitude slew manoeuvres with computation times compatible with real-time onboard implementation. The research question is answered through investigation of algorithmic optimisation strategies across transcription methods, integration schemes, NLP solvers, and initialisation approaches.

The optimisation framework employs multiple shooting transcription with RK4 integration, automatic differentiation, and the FATROP structured NLP solver. This configuration achieves median computation times of 0.100–0.115 s for symmetric spacecraft executing rest-to-rest and track-to-track manoeuvres, satisfying the 200 ms real-time threshold established in section 1.2. For asymmetric spacecraft configurations, the median computation time is 0.165 s for successfully converged cases that marginally satisfy real-time requirements, although the overall median, including failed convergences, is 0.295 s.

Convergence success rates of 91% for symmetric rest-to-rest manoeuvres, 88% for symmetric track-to-track manoeuvres, and 70% for asymmetric track-to-track manoeuvres are achieved with the optimised algorithm. These results represent substantial improvements over the CGPOPS benchmark algorithm, which exhibits success rates of 82.5%, 71.0%, and 64.9% for the corresponding scenarios while requiring computation times of 2–3 s. The optimised algorithm thus achieves approximately 10–15 \times computational speedup with 8–26% relative improvement in convergence reliability.

Non-optimal solution quality verification confirmed that even non-converged solutions provide trajectories of practical utility, with 75% of optimality gaps remaining below 9% and median deviations of 0.2–1.0% depending on the scenario.

The investigation of PSO-based metaheuristic initialisation strategies revealed configuration-dependent performance characteristics. For symmetric spacecraft, PSO with full control trajectory parameterisation achieved negligible improvements in success rate (0.1–0.2%) while requiring similar computation time, despite reducing gradient-based solver time by approximately 75%. However, for asymmetric configurations, PSO initialisation degraded both success rates and computation times relative to gradient-based optimisation from fixed initial guesses. This suggests that the PSO parameter tuning, conducted exclusively on symmetric rest-to-rest manoeuvres, does not generalise effectively to asymmetric spacecraft dynamics. The optimal configuration for general applications, therefore, omits PSO initialisation in favour of gradient-based optimisation from standardised initial guesses, and does not utilise the GPU.

The research demonstrates that real-time time-optimal spacecraft attitude control is achievable with the developed optimised algorithm. The sub-200 ms computation times achieved for symmetric spacecraft configurations enable closed-loop trajectory replanning at star tracker update rates, facilitating autonomous responses to mission requirements and environmental disturbances.

5.1 Limitations

Although the optimised algorithm was developed with the objective of being as inclusive as possible of every operational scenario, several limitations inherent to the current implementation warrant acknowledgement.

5.1.1 Modelling Assumptions and Scope

The spacecraft dynamics formulation assumes rigid body motion, neglecting flexibility effects that may be significant for spacecraft with large appendages or low structural frequencies. The applicability of the developed algorithm is therefore restricted to spacecraft configurations where rigid body assumptions provide adequate fidelity. Additionally, the optimal control problem formulation does not incorporate control rate constraints, despite actuator slew rate limitations being present in physical reaction wheel and control moment gyroscope systems. The omission of control rate constraints may result in trajectories that, while theoretically time-optimal, are infeasible for implementation on systems with finite actuator bandwidth.

The implemented framework requires spacecraft inertia tensor properties to be specified at compile time as constants. This design decision, while enabling certain compiler optimisations, precludes runtime adaptation to time-varying mass properties during mission execution. For spacecraft experiencing significant propellant consumption or configuration changes through deployment mechanisms, this limitation necessitates either accepting a degraded solution accuracy as inertia properties deviate from compiled nominal values or periodically recompiling and redeploying the optimisation algorithm with updated parameters.

5.1.2 Numerical Integration and Asymmetric Spacecraft

While the developed algorithm demonstrates robust performance for symmetric spacecraft configurations across both rest-to-rest and track-to-track manoeuvres, the reliability degradation observed with an asymmetric spacecraft suggests that additional investigation is needed.

The RK4 integration method, while computationally efficient and accurate for symmetric and mildly asymmetric configurations, has not been verified for spacecraft with highly disparate principal moments of inertia. The cross-coupling terms in Euler's equations would become increasingly dominant, potentially requiring tighter integration tolerances or higher-order schemes to maintain solution accuracy. The impact of extreme inertia asymmetry on integration error accumulation, constraint satisfaction, and convergence basin geometry requires further investigation.

5.1.3 PSO Parameter Tuning Scope

The PSO parameter optimisation was conducted using only 1000 parameter combinations, each evaluated across 1000 manoeuvre scenarios. While this approach identified configurations that yield good performance for scenarios A and B, the results suggest that optimal PSO parameters exhibit sensitivity to the spacecraft configuration. The parameter tuning was performed exclusively for symmetric spacecraft executing rest-to-rest manoeuvres, and the resulting configurations demonstrated suboptimal performance when applied to asymmetric configurations. The scope of the conducted tuning study was constrained by the availability of computational resources and the project timeline.

5.1.4 Computational Hardware

The computational performance results presented throughout this thesis were obtained using a consumer-grade laptop platform from 2018. The reported computation times, therefore, represent performance on hardware substantially less capable than modern computers or contemporary CPU and GPU architectures in terms of core count, memory bandwidth, and floating-point throughput.

5.2 Future Work

Several avenues for extending and enhancing the developed optimisation framework have been identified through the research conducted in this thesis.

5.2.1 Extended Dynamical Models

The rigid body assumption employed in the current formulation could be relaxed to incorporate flexible body dynamics for spacecraft with significant structural flexibility. This extension would require coupling of attitude dynamics with structural deformation modes, increasing problem dimensionality but enabling application to a broader class of spacecraft configurations. Additionally, the inclusion of control rate constraints in the optimal control problem formulation would produce trajectories that account for finite actuator bandwidth limitations, improving implementability on physical spacecraft systems.

5.2.2 Runtime Inertia Adaptation

The compile-time specification of inertia tensor properties could be replaced with a runtime parameterisation approach that accepts time-varying mass properties as inputs to the optimisation algorithm. This modification would require careful consideration of potential performance implications from reduced compiler optimisation opportunities.

5.2.3 Adaptive PSO Parameterisation

A more comprehensive PSO parameter tuning methodology could be developed involving configuration-specific optimisation with adaptive parameter scheduling based on inertia properties. The implementation of adaptive metaheuristic strategies or the development of inertia-ratio-dependent parameter selection heuristics may yield improved convergence reliability for asymmetric spacecraft configurations. Expansion of the parameter search space beyond the 1000 combinations evaluated in this thesis, combined with evaluation across asymmetric spacecraft scenarios, would provide more robust parameter sets.

5.2.4 Path Constraint Integration

Extending the optimal control problem formulation to incorporate state-dependent inequality constraints along the trajectory, such as keep-out cones, would enable the modelling of operational constraints. This enhancement would require an evaluation of the computational cost and convergence reliability implications of increasing problem dimensionality by adding path constraints.

5.2.5 Hardware-in-the-Loop Validation

Integration of the developed optimisation framework with representative spacecraft attitude determination and control system components would provide a higher-fidelity assessment of real-time feasibility and help identify potential implementation challenges not evident in purely numerical simulation environments. Hardware-in-the-loop validation should include actual sensor suites, real actuator dynamics models, and flight software architectures with realistic timing constraints and computational resource limitations.

5.3 Closing Remark

The framework developed in this thesis establishes a foundation for autonomous spacecraft that can compute and execute time-optimal manoeuvres within sensor update cycles, closing the control loop around optimal trajectory generation. This represents a significant step toward spacecraft systems capable of autonomous, optimally responsive operations in dynamic mission environments. The open-source implementation and comprehensive verification methodology provide a platform for continued advancement in real-time aerospace trajectory optimisation, with potential extensions to path-constrained problems and coupled translational-rotational dynamics.

Bibliography

- [1] M. Wilde, J. Harder, and E. Stoll, “Editorial: On-orbit servicing and active debris removal: Enabling a paradigm shift in spaceflight,” *Frontiers in Robotics and AI*, vol. 6, p. 136, 2019.
- [2] C. D. Petersen, “Advances in underactuated spacecraft control,” Ph.D. dissertation, University of Michigan, 2016.
- [3] K. D. Bilimoria and B. Wie, “Time-optimal three-axis reorientation of a rigid spacecraft,” *Journal of Guidance, Control, and Dynamics*, vol. 16, no. 3, pp. 446–452, May/Jun. 1993.
- [4] X. Bai and J. L. Junkins, “New results for time-optimal three-axis reorientation of a rigid spacecraft,” *Journal of Guidance, Control, and Dynamics*, vol. 32, no. 4, pp. 1071–1076, Jul./Aug. 2009.
- [5] S. L. Scrivener and R. C. Thompson, “Survey of time-optimal attitude maneuvers,” *Journal of Guidance, Control, and Dynamics*, vol. 17, no. 2, pp. 225–233, mar 1994.
- [6] B. Pain, B. Hancock, C. Liebe, and J. Mellstrom, “Stellar gyroscope for determining attitude of a spacecraft,” Jet Propulsion Laboratory, California Institute of Technology, Pasadena, CA, United States, NASA Tech Brief NPO-30481, Oct. 2005, document ID: 2011016302. [Online]. Available: <http://www.techbriefs.com/component/content/518?task=view>
- [7] Y. M. Agamawi and A. V. Rao, “Cgpops: A c++ software for solving multiple-phase optimal control problems using adaptive gaussian quadrature collocation and sparse nonlinear programming,” 2019. [Online]. Available: <https://arxiv.org/abs/1905.11898>
- [8] M. D. Shuster, “A survey of attitude representations,” *Journal of the Astronautical Sciences*, vol. 41, no. 4, pp. 439–517, 1993.
- [9] R. M. Byers, “Time optimal attitude control of asymmetric rigid spacecraft,” *Journal of Vibration and Control*, vol. 2, no. 1, pp. 17–32, 1996, received 12 June 1995; Accepted 5 September 1995.
- [10] A. Fleming, P. Sekhavat, and I. M. Ross, “Minimum-time reorientation of a rigid body,” *Journal of Guidance, Control, and Dynamics*, vol. 33, no. 1, pp. 160–170, January–February 2010.
- [11] T. Lee, M. Leok, and N. H. McClamroch, “Optimal attitude control of a rigid body using geometrically exact computations on $\text{SO}(3)$,” *Journal of Optimization Theory and Applications*, 2006, arXiv:math/0601424.
- [12] S. Kulamani and T. Lee, “Constrained geometric attitude control on $\text{SO}(3)$,” *International Journal of Control, Automation, and Systems*, vol. 15, no. 6, pp. 2674–2685, December 2017, arXiv:1711.10992.
- [13] S. T. McDonald, T. L. Griszel, and Z. Wang, “A real-time approach to minimum-energy reorientation of an asymmetric rigid body spacecraft,” in *AIAA Scitech 2020 Forum*. Orlando, FL: American Institute of Aeronautics and Astronautics, January 2020, p. 1261.
- [14] L. S. Pontryagin, V. G. Boltyanskii, R. V. Gamkrelidze, and E. F. Mishchenko, *The Mathematical Theory of Optimal Processes*. New York: Wiley-Interscience, 1962.

Bibliography

- [15] J. T. Betts, *Practical Methods for Optimal Control Using Nonlinear Programming*, 3rd ed., ser. Advances in Design and Control. Philadelphia, PA: Society for Industrial and Applied Mathematics, 2020, vol. 36.
- [16] R. Kress, “Initial value problems,” in *Numerical Analysis*, ser. Graduate Texts in Mathematics. New York, NY: Springer, 1998, vol. 181, ch. 10, pp. 225–257.
- [17] D. J. Gardner, D. R. Reynolds, C. S. Woodward, and C. J. Balos, “Enabling new flexibility in the SUNDIALS suite of nonlinear and differential/algebraic equation solvers,” *ACM Transactions on Mathematical Software (TOMS)*, 2022.
- [18] A. C. Hindmarsh, P. N. Brown, K. E. Grant, S. L. Lee, R. Serban, D. E. Shumaker, and C. S. Woodward, “SUNDIALS: Suite of nonlinear and differential/algebraic equation solvers,” *ACM Transactions on Mathematical Software (TOMS)*, vol. 31, no. 3, pp. 363–396, 2005.
- [19] R. Serban and A. C. Hindmarsh, “CVODES: The sensitivity-enabled ODE solver in SUNDIALS,” in *Proceedings of the ASME 2005 International Design Engineering Technical Conferences and Computers and Information in Engineering Conference*, vol. 6. Long Beach, California, USA: ASME, September 2005, pp. 257–269.
- [20] C. J. Balos, D. J. Gardner, C. S. Woodward, and D. R. Reynolds, “Enabling gpu accelerated computing in the sundials time integration library,” *Parallel Computing*, vol. 108, p. 102836, 2021.
- [21] M. A. Patterson and A. V. Rao, “GPOPS-II: A MATLAB software for solving multiple-phase optimal control problems using hp-adaptive gaussian quadrature collocation methods and sparse nonlinear programming,” *ACM Transactions on Mathematical Software*, vol. 41, no. 1, pp. 1:1–1:37, 2014.
- [22] A. Wächter and L. T. Biegler, “On the implementation of a primal-dual interior point filter line search algorithm for large-scale nonlinear programming,” *Mathematical Programming*, vol. 106, no. 1, pp. 25–57, 2006.
- [23] P. E. Gill, W. Murray, and M. A. Saunders, “SNOPT: An SQP algorithm for large-scale constrained optimization,” *SIAM Review*, vol. 47, no. 1, pp. 99–131, 2005.
- [24] D. Spiller, L. Ansalone, and F. Curti, “Particle swarm optimization for time-optimal spacecraft reorientation with keep-out cones,” *Journal of Guidance, Control, and Dynamics*, vol. 39, no. 2, pp. 312–325, February 2016.
- [25] H. Seywald, “Trajectory optimization based on differential inclusion,” *Journal of Guidance, Control, and Dynamics*, vol. 17, no. 3, pp. 480–487, 1994.
- [26] G. A. Boyarko, M. Romano, and O. A. Yakimenko, “Time-optimal reorientation of a spacecraft using an inverse dynamics optimization method,” *Journal of Guidance, Control, and Dynamics*, vol. 34, no. 4, pp. 1197–1208, July-August 2011. [Online]. Available: <https://arc.aiaa.org/doi/10.2514/1.49449>
- [27] L. Vanroye, A. Sathya, J. De Schutter, and W. Decré, “Fatrop: A fast constrained optimal control problem solver for robot trajectory optimization and control,” in *2023 IEEE/RSJ International Conference on Intelligent Robots and Systems (IROS)*. IEEE, 2023, pp. 10 036–10 043.
- [28] J. Nocedal and S. J. Wright, *Numerical Optimization*, 2nd ed., ser. Springer Series in Operations Research and Financial Engineering. New York, NY: Springer, 2006.

- [29] R. Verschueren, G. Frison, D. Kouzoupis, J. Frey, N. van Duijkeren, A. Zanelli, B. Novoselnik, T. Albin, R. Quirynen, and M. Diehl, “acados – a modular open-source framework for fast embedded optimal control,” *Mathematical Programming Computation*, 2021.
- [30] G. Frison and M. Diehl, “Hpipm: a high-performance quadratic programming framework for model predictive control**this research was supported by the german federal ministry for economic affairs and energy (bmwi) via eco4wind (0324125b) and dyconpv (0324166b), and by dfg via research unit for 2401.” *IFAC-PapersOnLine*, vol. 53, no. 2, pp. 6563–6569, 2020, 21st IFAC World Congress. [Online]. Available: <https://www.sciencedirect.com/science/article/pii/S2405896320303293>
- [31] J. A. E. Andersson, J. Gillis, G. Horn, J. B. Rawlings, and M. Diehl, “CasADi: A software framework for nonlinear optimization and optimal control,” *Mathematical Programming Computation*, vol. 11, no. 1, pp. 1–36, 2019.
- [32] D. Malyuta, Y. Yu, P. Elango, and B. Açıkmeşe, “Advances in trajectory optimization for space vehicle control,” *Annual Reviews in Control*, vol. 52, pp. 282–315, 2021. [Online]. Available: <https://doi.org/10.1016/j.arcontrol.2021.04.013>
- [33] J. A. E. Andersson, “A general-purpose toolbox for nonlinear optimization,” CasADi Documentation, 2018, available: <https://web.casadi.org>.
- [34] G. R. Hecht and E. M. Botta, “Particle swarm optimization-based co-state initialization for low-thrust minimum-fuel trajectory optimization,” *Acta Astronautica*, vol. 211, pp. 416–430, 2023.
- [35] R. G. Melton, “Hybrid methods for determining time-optimal, constrained spacecraft reorientation maneuvers,” *Acta Astronautica*, vol. 94, pp. 294–301, 2014.
- [36] J. Kennedy and R. C. Eberhart, “A discrete binary version of the particle swarm algorithm,” in *Proceedings of the 1997 IEEE International Conference on Systems, Man, and Cybernetics. Computational Cybernetics and Simulation*, vol. 5. Orlando, FL, USA: IEEE, October 1997, pp. 4104–4108.
- [37] C.-C. Wang, C.-Y. Ho, C.-H. Tu, and S.-H. Hung, “cuPSO: GPU parallelization for particle swarm optimization algorithms,” 2023, arXiv preprint arXiv:2205.01313v2.
- [38] Y. Zhuo, T. Zhang, F. Du, and R. Liu, “A parallel particle swarm optimization algorithm based on GPU/CUDA,” *Applied Soft Computing*, vol. 144, p. 110499, 2023.
- [39] J. Nickolls, I. Buck, M. Garland, and K. Skadron, “Scalable parallel programming with CUDA,” *ACM Queue*, vol. 6, no. 2, pp. 40–53, Mar./Apr. 2008.
- [40] NVIDIA Corporation, *CUDA C++ Programming Guide*, NVIDIA Corporation, 2024, version 12.x. [Online]. Available: <https://docs.nvidia.com/cuda/cuda-c-programming-guide/>
- [41] S. H. Jeon, S. Hong, H. J. Lee, C. Khazoom, and S. Kim, “CusADi: A GPU parallelization framework for symbolic expressions and optimal control,” *arXiv preprint arXiv:2408.09662*, 2024. [Online]. Available: <https://arxiv.org/abs/2408.09662>
- [42] N. F. Gade-Nielsen, “Interior point methods on GPU with application to model predictive control,” PhD thesis, Technical University of Denmark, Department of Applied Mathematics and Computer Science, Kongens Lyngby, Denmark, Apr. 2014. [Online]. Available: <https://orbit.dtu.dk>
- [43] J. L. Loepky, J. Sacks, and W. J. Welch, “Choosing the sample size of a computer experiment: A practical guide,” *Technometrics*, vol. 51, no. 4, pp. 366–376, 2009.

Bibliography

- [44] M. D. McKay, R. J. Beckman, and W. J. Conover, “A comparison of three methods for selecting values of input variables in the analysis of output from a computer code,” *Technometrics*, vol. 21, no. 2, pp. 239–245, 1979.
- [45] M. Stein, “Large sample properties of simulations using Latin hypercube sampling,” *Technometrics*, vol. 29, no. 2, pp. 143–151, 1987.
- [46] W. Zhang, W. Quan, and L. Guo, “Blurred star image processing for star sensors under dynamic conditions,” *Sensors*, vol. 12, no. 5, pp. 6712–6726, 2012. [Online]. Available: <https://doi.org/10.3390/s120506712>